DROP-DROP AND DROP-SURFACE DYNAMICS DURING IMPACT AND ELECTROHYDRODYNAMIC INTERACTIONS

A thesis submitted
in partial fulfillment of the requirements
for the degree of

Doctor of Philosophy

by

Santanu Kumar Das

Department of Mechanical Engineering
Indian Institute of Technology Guwahati

October 2023

Dedicated to

all who

made me what I am today

CERTIFICATE

It is certified that the work contained in the thesis entitled "**Drop-drop and drop-surface dynamics during impact and electrohydrodynamic interactions**", by **Santanu Kumar Das** (Reg no. 186103031) has been carried out under my supervision and that this work has not been submitted elsewhere for a degree.

(Amaresh Dalal)
Professor
Department of Mechanical Engineering
Indian Institute of Technology Guwahati

June 2023

Acknowledgements

The present work is the achievement of my research as a student at the Indian Institute of Technology Guwahati, Assam. This thesis was completed due to the support and help of many people whom I want to acknowledge.

Firstly, I want to thank my supervisor, Prof. Amaresh Dalal, for his advice and support during the work. His dedication and generosity with time, which helped me in my career, is much appreciated. He allowed me to pursue my ideas and work independently and was always available to discuss various problems. His attitude towards students and the countless hours of discussions on different issues have changed me in many ways. I enjoyed spending my research career with him, both at work and otherwise. I would also like to thank my doctoral committee members - Prof. Anoop Kumar Dass, Prof. Vinayak Kulkarni, and Prof. Dipankar Bandyopadhyay, for their insight and suggestions during my progress seminars.

I am grateful to my supervisor for introducing me to two of the most notable researchers in my field - Prof. Gautam Biswas and Prof. Gaurav Tomar. My sincere acknowledgment is to Prof. Gautam Biswas (IIT Kanpur), who provided guidance and exposed me to the area of computational multiphase flows. The rich discussions and experience obtained while collaborating with him helped shape my research interest. I take this opportunity to thank Prof. Gaurav Tomar (IISc Bangalore) for being a mentor during my whole research journey. He has been encouraging, enthusiastic and supportive throughout my graduate life. He brought unique perspectives to the problems I have worked on. I would also like to thank him for hosting me for a month at IISc Bangalore. Working with him in close contact has led to fruitful research training for me. I acknowledge him for introducing me to one of his students, Sarika. She has been immensely helpful in making my stay at IISc fruitful. I learned a lot from her, especially the theoretical aspects of electrohydrodynamic flows.

I would also like to thank the Computer and Communication Center of IIT Guwahati for providing access to the Param-Ishan supercomputing facility, which was invaluable for the simulations carried out in my work.

My friends have been a very crucial part of my journey as well. Members of my research group have contributed tremendously to my research activities. I want to thank Dr. Mansh Pratim Borthakur for helping me get started on my project and guide me through the computational tools. I also want to thank Dr. Bhaskarjyoti Sarma for his never-ending guidance and constant motivation and for providing a warm environment when I joined the lab. Thanks to all the Anupravaha lab members for making it a delightful workplace. They have asked me great questions during group meetings, making me think deeper about my work. Niraj, Dheeraj, and Rupresha, thank you for being genuine and supportive. I have also been blessed with good friends who always stood beside me. I have to give a special shoutout to Chandan, Tanuj, and Rohit for being very sensitive at a particularly difficult point in my Ph.D. I want to thank Bikram, Brijesh, Pranab, Dr. Nitesh, Rishabh, Ashok, Abhijit, Biswajyoti, and Pijush for making the campus an enjoyable place to work. I would also like to thank all my friends in the Mechanical Engineering department, and outside the department for being there for me and providing a great work-life balance.

Finally, I would like to thank my parents for their unconditional love and support and for the sacrifices they made for me. I would also like to thank my brother and sister-in-law for supporting me. Your love, support, and dedication make me strive to grow personally and professionally.

Santanu Kumar Das
June 2023

Abstract

The interaction between drop-drop and drop-surface is an essential aspect of fundamental studies in fluid dynamics. Studies of such dynamics have been of great interest to researchers and are important because of their applications in various industrial processes. Due to the recent advancements in microfluidic devices and biological processes, electrohydrodynamic flows became a critical part of these investigations. Robust computational tools have been utilized to understand the fundamental aspects of drop-drop and drop-surface interactions. The solvers are well-validated with past experimental and numerical results. All the numerical simulations have been performed by solving the Navier-Stokes equations, with other forcing terms, wherever required. The electrohydrodynamic flows required the solution of additional electric field equations. The two-phase problems involve tracking the interface, which is captured using either a volume of fluid (VOF) method or a coupled level set and volume of fluid (CLSVOF) method.

The impact of a liquid drop on a liquid pool has been widely investigated. The transition regimes between coalescence and splashing of drops include jet formation with single or multiple secondary drops. One of the main features of this regime is the formation of a central liquid jet followed by the breakup of the jet in the form of drops. Earlier studies have shown that the diameter of the secondary drop lies between 0.58 and 0.94 times the diameter of the impacting drop. We perform numerical investigations to elucidate the earlier observations. The investigations notify the creation of various secondary drops depending on the impact conditions. As a novelty, the present study reveals that secondary drops larger than the primary impacting drop can be obtained at higher impact velocities. We identify the importance of the shape of the cavity on the formation of the jet and the pertaining parameters that are responsible for drop ejection.

The dispersion of drops in an emulsion is commonly seen in several chemical, pharmaceutical, and petroleum industries. An electric field has been shown to affect the stability of these dispersions. We numerically study the dynamics of a pair of

leaky-dielectric droplets in a leaky-dielectric liquid in an externally applied electric field. A pair of drops may coalesce or repel each other in the presence of the electric field. Interactions between a pair of drops are governed by the ratio R/Q, where R and Q are the ratios of drop to ambient fluid electric conductivities and permittivities, respectively. When inertia is neglected, the drops approach each other if $R < Q$, whereas drops repel when $R > Q$. However, the inclusion of inertia permits interesting transient behavior, where the drops may attract due to the electrostatic dipole-dipole attraction even for $R > Q$. The approach velocity then can be governed by the electrostatic forces and varies as $1/h^4$, where h is the separation distance between the drops, in contrast to being hydrodynamically driven as predicted in the Stokes' flow. For compound drops, interactions are essentially governed by the electrical properties of the outer drop and the ambient fluid. However, transient dynamics may also result in the breakup of a compound drop and lead to the formation of single drops.

Studies with creeping flow approximations have shown that depending on the electrical properties, the drops can repel and move apart or get attracted toward each other. This leads to the formation of a stable or unstable emulsion. Incorporating inertia leads to another interaction paradigm where the drops can come closer and form a thin film without coalescing. The formation of the stable thin film was theoretically explained using the electrostatic to hydrodynamic forces ratio. We defined a phase map representing regions for various drop interaction dynamics. Although this phase map is valid for a specific electric field strength, it gives a general idea about the interaction dynamics for a pair of leaky-dielectric drops under the influence of an external electric field.

Understanding polymer blends is essential in foods, paints, cosmetics, and processing industries. The properties of these emulsions are directly related to the microstructure of the polymers resulting from drop deformation, coalescence, and breakup. We study the effect of an electric field on the deformation of the drop suspended in a medium. The drop/medium is considered to be viscoelastic. Accordingly, we have two configurations: a viscoelastic drop suspended in a Newtonian fluid (VN) and a Newtonian fluid suspended in a viscoelastic medium (NV). The viscoelasticity is modeled using the Oldroyd-B constitutive equation. For the VN configuration, drop deformation decreased with an increase in Deborah number. In contrast, the NV configuration showed a non-monotonic nature in the steady-state deformation. These dynamics are explained by examining the viscous and elastic stresses at the drop interface.

Contents

List of Figures **xv**

Nomenclature **xxiii**

1 Introduction **1**

1.1 Literature review . . . 2

1.1.1 Drop impact dynamics . . . 2

1.1.2 Electrohydrodynamics . . . 6

1.1.3 Viscoelastic flows . . . 14

1.2 Motivation . . . 18

1.3 Objectives . . . 19

1.4 Outline of thesis . . . 19

2 Formulation and numerical modeling **21**

2.1 CLSVOF method . . . 22

2.1.1 Governing equations . . . 23

2.1.2 Interface construction . . . 23

2.1.3 Interface advection . . . 24

2.1.4 Numerical scheme . . . 28

2.2 BASILISK solver . . . 29

2.2.1 Governing equations . . . 30

2.2.2 Numerical scheme . . . 33

2.2.3 Spatial dicretization . . . 37

2.3 Summary . . . 38

3 Evolution of jets during drop impact on a deep liquid pool **39**

3.1 Introduction . . . 39

3.2 Formulation . . . 40

3.2.1 Computational domain 40
3.2.2 Solution methodology 41
3.2.3 Dimensionless parameters 42
3.3 Validation 43
3.3.1 Comparison with literature 43
3.3.2 Grid independence studies 43
3.4 Results and discussion 45
3.4.1 Long thick central jet with smaller secondary drop 45
3.4.2 Slender jet with multiple secondary drops 47
3.4.3 Long thick central jet with larger secondary drop 49
3.4.4 Central jet characterization 51
3.5 Summary 53

4 Electrohydrodynamic induced interactions between drops 55
4.1 Introduction 55
4.2 Formulation 57
4.2.1 Computational domain 57
4.2.2 Solution methodology 58
4.2.3 Dimensionless parameters 59
4.3 Validation 60
4.3.1 Comparison with literature 60
4.3.2 Grid independence studies 61
4.4 Results and discussion 62
4.4.1 Interaction dynamics of single emulsion 63
4.4.2 Interaction dynamics of double emulsion 70
4.5 Summary 78

5 Noncoalescence in leaky-dielectric emulsions 79
5.1 Introduction 79
5.2 Formulation 81
5.2.1 Computational domain 81
5.2.2 Solution methodology 82
5.2.3 Dimensionless parameters 83
5.3 Validation 83
5.3.1 Comparison with literature 83
5.3.2 Grid independence studies 85

5.4 Results and discussion 86
5.4.1 Interaction between leaky-dielectric drops 87
5.4.2 Regime map for interacting drop pair 93
5.5 Summary 94

6 Viscoelastic effects on drop deformation 97
6.1 Introduction 97
6.2 Formulation 99
6.2.1 Computational domain 99
6.2.2 Solution methodology 100
6.2.3 Dimensionless parameters 101
6.3 Validation 102
6.3.1 Comparison with literature 102
6.3.2 Grid independence studies 103
6.4 Results and discussion 104
6.4.1 Transient drop deformation 105
6.4.2 Steady state drop deformation 106
6.5 Summary 110

7 Conclusions and scope for future work 111
7.1 Conclusions 111
7.2 Scope of future work 115

References 117

Appendix A Log conformation representation 131

Appendix B Dimensionless equations 133

Appendix C Grid representation 139

List of publications 141

List of Figures

1.1 Snapshots of splash of a drop of water 0.2 gm, 7.36 mm in diameter, falling from a height of 40 cm into water. Figures reproduced from Worthington (1908). 3
1.2 Transition from coalescence to splashing. Reproduced from Rein (1996). 4
1.3 Schematic representation of the deformation of a drop with radius a suspended in another fluid in the presence of an electric field $\mathbf{E}$. The initial undeformed state of the drop is shown using a solid line. The possible steady-state deformed shapes, prolate and oblate, are also illustrated. The relevant properties of the drop (1) and suspending medium (2) are the viscosity μ, dielectric permittivity ε, and electrical conductivity σ. The semi-major and semi-minor axis of the deformed drop are denoted by L and B, respectively. 7
1.4 Shape evolution of castor oil drop in silicone oil. The drop begins with as spherical shape to transient stretching and consequent breakup from the ends. The critical electric capillary number for the breakup is $Ca_E \sim 0.26$. Figures reproduced from Abbasi et al. (2019a). 10
1.5 Breakups of the A/B/C type emulsion drop under an electric field. The surface tension between the shell and ambient, the permittivity of the ambient fluid, and the core and shell diameter are kept constant. The electric field and the surface tension between the core and shell are changed to study the breakup modes. Figures reproduced from Abbasi et al. (2019b). 12

1.6 Coalescence of castor oil drops in silicone oil. Stable and unstable coalescence were observed due to the applied electric field strength. At stronger electric fields, the coalesced droplet became unstable, continuously stretched after the merger, and began to eject droplets at the side ends. Figures reproduced from Abbasi et al. (2022). 13
1.7 Viscoelastic flow behavior due to the normal stress difference. (a) Fixed cylinder with rotating rod. The Newtonian liquid (glycerin) shows a vortex. The polymer solution (polyacrylamide in glycerin) climbs the rod. (b) Flow from orifices. The Newtonian fluid, (silicone oil) shows no diameter increase upon emergence from capillary tube. The polymer solution (polymethylmethacrylate in dimethylphthalate) shows an increase by a factor of 3 in diameter as it flows out of the tube. Figures have been reproduced from Bird et al. (1987a). 16

2.1 A representative diagram showing (a) volume fraction advection into the neighboring cell on the right, and (b) distribution of level-set function around the interface. 26

3.1 Schematic diagram (not to scale) showing the initial configuration and boundary conditions in an axisymmetric cylindrical coordinate system (r, z). The drop is placed near the free surface of the liquid pool. Gravity ($\mathbf{g}$) acts along negative z axis. The size of the domain is $8D_o \times 16D_o$ with the initial height of the liquid pool as $6D_o$. 41
3.2 Qualitative comparison between the (a) experimental and (b) numerical results of Morton et al. (2000) with the (c) present results for a 2.9 mm equivalent diameter drop impacting from a height of 170 mm ($Fr = 85, We = 96, Re = 4480$). (d) Quantitative comparison of temporal evolution of the cavity depth. 44
3.3 Qualitative comparison between the (a) experimental and (b) numerical results of Morton et al. (2000) with the (c) present results for a 2.9 mm equivalent diameter drop impacting from a height of 400 mm ($Fr = 220, We = 248, Re = 7250$). (d) Quantitative comparison of temporal evolution of the cavity depth. 44

3.4 Evolution of the fall of a liquid drop showing the phenomena of formation of long thick jet with a smaller secondary drop ($D_s/D_o < 1$) at different time instants. The corresponding dimensionless parameters are $Fr = 188, We = 310$ and $Re = 8870$. 46
3.5 Expansion and retraction stages during the phenomena of formation of long thick jet with a smaller secondary drop ($D_s/D_o < 1$). The arrows denote the typical flow directions. 46
3.6 Different quantities vs. the Froude number: (a) secondary to primary diameter ratio (blue circle), and (b) pinch-off time (green diamond). The dashed line represents the linear fit for the corresponding plots, with the fitting value shown in the inset. 47
3.7 Evolution of the fall of a liquid drop showing the phenomena of formation of long thin jet with multiple secondary drops at different time instants. The corresponding dimensionless parameters are $Fr = 238, We = 393$ and $Re = 9987$. 48
3.8 Expansion and retraction stages during the phenomena of formation of long thin jet with multiple secondary drops. The arrows denote the typical flow directions. 48
3.9 Evolution of the fall of a liquid drop showing the phenomena of formation of long thick jet with a larger secondary drop ($D_s/D_o > 1$) at different time instants. The corresponding dimensionless parameters are $Fr = 407, We = 671$ and $Re = 13,060$. 49
3.10 Expansion and retraction stages during the phenomena of formation of long thick jet with a larger secondary drop ($D_s/D_o > 1$). The arrows denote the typical flow directions. 50
3.11 Different quantities vs. the Froude number: (a) secondary to primary diameter ratio (blue circle), and (b) pinch-off time (green diamond). The dashed line represents the linear fit for the corresponding plots, with the fitting value shown in the inset. For this range, we obtain a larger secondary drop diameter compared to the initial drop. 51
3.12 Secondary to primary diameter ratio vs. the Froude number. The dashed line represents the linear fit. 52

3.13 Different quantities vs. the Froude number: (a) central jet height (blue circle), and (b) jet velocity (green diamond). The dashed line represents the linear fit for the corresponding plots, with the fitting value shown in the inset. 53

4.1 Schematic diagram (not to scale) showing a pair of compound drops interacting in the presence of an externally applied electric field in an axisymmetric cylindrical coordinate system (r, z). The radius of the outer drop (shell) and the inner drop (core) are a and $a/3$, respectively. Electric field ($\mathbf{E}$) is applied along negative z axis. The size of the domain is $16a \times 16a$. 57

4.2 Comparison of deformation (D) of a single drop with theoretical and computational studies. Other dimensionless parameters for the computations are $Q = 10$, $Ca_E = 0.18$, $Re = 0.10$, $Re_E = 0.01$, $\rho_r = 1$, and $\mu_r = 1$. 61

4.3 Temporal variation of deformation D of the drop under a steady electric field, using six different grid refinements. The inset shows the zoomed view for better convergence analysis. The parameters considered for the simulations are $R = 0.1$, $Q = 2$, $Ca_E = 0.2$, $Re = 5$, and $Re_E = 0.01$. . 62

4.4 Streamlines and variation in the drop shape for different conductivity ratios. The other computation parameters are $Q = 10$, $Ca_E = 0.18$, and $Re = 0.10$. 63

4.5 Drop interaction along with the streamline patterns observed for $R = 6$ and $Q = 8$ at $Ca_E = 1.5$ and $Re = 0.10$. 64

4.6 Drop interaction along with the streamline patterns observed for $R = 1.04$ and $Q = 0.2$ at $Ca_E = 1.5$ and $Re = 0.10$. 65

4.7 Temporal variation in surface charge density (q_s) along the interface and the charge distribution around the interface for (a) $R = 6$ and $Q = 8$ and (b) $R = 1.04$ and $Q = 0.2$ at $Ca_E = 1.5$ and $Re = 0.10$. 66

4.8 Velocity variation with respect to center-to-center distance between the drops for (a) $R = 6$ and $Q = 8$ and (b) $R = 1.04$ and $Q = 0.2$ at $Ca_E = 1.5$ and $Re = 0.10$. 68

4.9 Temporal evolution of a pair of non-coalescing drops for $R = 25$ and $Q = 2$ at $Ca_E = 0.2$ and $Re = 1$. Also shown are the zoomed-in views (representing the same area) and streamlines at $t = 70$. 69

4.10 Comparison of deformation of the core and the shell of a compound drop at $Ca_E = 0.2$ and $Re = 0.10$ for (a) $Q = 2$ and (b) $R = 2.5$. 71
4.11 Streamlines and variation in the shape of the core and shell for different conductivity and permittivity ratios. The other computation parameters are $Ca_E = 0.2$, and $Re = 0.10$. 72
4.12 Drop deformation and translation at different time instances for $R = 10$ and $Q = 25$ using the flow parameters $Ca_E = 0.12$ and $Re = 1$. We also plot the flow patterns in and around the core and shell at $t = 29$ and $t = 40$. 73
4.13 Drop deformation and translation at different time instances for $R = 3$ and $Q = 0.15$ using the flow parameters $Ca_E = 0.12$ and $Re = 1$. We also plot the flow patterns in and around the core and shell at $t = 30$ and $t = 200$. 73
4.14 Velocity variation with respect to center-to-center distance between the drops for (a) $R = 10$ and $Q = 25$ and (b) $R = 3$ and $Q = 0.15$ at $Ca_E = 0.12$ and $Re = 1$. The motion of the inner core drop is also depicted. 74
4.15 Drop deformation and translation at different time instances for $R = 1.5$ and $Q = 10$ using the flow parameters $Ca_E = 0.12$ and $Re = 1$. We also plot the flow patterns in and around the core and shell at $t = 14$ and $t = 20$. 75
4.16 Drop deformation and translation at different time instances for $R = 10$ and $Q = 30$ using the flow parameters $Ca_E = 0.12$ and $Re = 1$. We also plot the flow patterns in and around the core and shell at $t = 34$ and $t = 50$. 75
4.17 Drop deformation and translation at different time instances for $R = 20$ and $Q = 1$ using the flow parameters $Ca_E = 0.12$ and $Re = 1$. We also plot the flow patterns in and around the core and shell at $t = 30$ and $t = 50$. 76
4.18 Drop deformation and translation at different time instances for $R = 30$ and $Q = 10$ using the flow parameters $Ca_E = 0.12$ and $Re = 1$. We also plot the flow patterns in and around the core and shell at $t = 24$ and $t = 60$. 77

4.19 Drop deformation and translation at different time instances for $R = 7$ and $Q = 10$ using the flow parameters $Ca_E = 0.12$ and $Re = 1$. We also plot the flow patterns in and around the core and shell at $t = 50$ and $t = 100$. 77

5.1 Schematic diagram (not to scale) showing a pair of drops interacting in the presence of an externally applied electric field in an axisymmetric cylindrical coordinate system (r, z). The radius of the drops are a and are placed at a separation of $h = 4a$. Electric field ($\mathbf{E}$) is applied along negative z axis. The size of the domain is $16a \times 16a$. 81

5.2 Comparison of the interaction of a silicone oil drop pair in castor oil under uniform DC electric field of $E_\infty = 2.22$ kV/cm. The radius of the drop is $a = 270\mu m$. The experimental result is obtained from Figure 14 of Mhatre et al. (2015a). The red dotted lines are the results from the present solver. 84

5.3 Comparison of the interaction of a silicone oil drop pair in castor oil under uniform DC electric field of $E_\infty = 2.22$ kV/cm. The radius of the drop is $a = 270\mu m$. The experimental result is obtained from Figure 14 of Mhatre et al. (2015a). 84

5.4 Plot of relative velocity and the separation between the drops at six different grid refinements. The parameters considered for the computations are $R = 10$, $Q = 20$, $Re = 1$, $Ca_E = 0.12$, $h/a = 4$, $\mu_r = 1$ and $\rho_r = 1$. 85

5.5 Phase diagram of the expected shape response and the circulation patterns as a function of the conductivity (R) and permittivity (Q) ratios. The zero deformation curve and the $R = Q$ line delineate three combinations of deformation and circulation. The marked points are the (R, Q) parameters presented in this study. 86

5.6 Drop deformation and translation at different time instances for $R = 2.5$ and $Q = 0.4$ using the flow parameters $Ca_E = 0.12$ and $Re = 1$. We also plot the flow patterns at $t = 100$. 88

5.7 Drop deformation and translation at different time instances for $R = 16$ and $Q = 1$ using the flow parameters $Ca_E = 0.12$ and $Re = 1$. We also plot the flow patterns at $t = 50$. 88

5.8 Drop deformation and translation at different time instances for $R = 64$ and $Q = 6.4$ using the flow parameters $Ca_E = 0.12$ and $Re = 1$. We also plot the flow patterns at $t = 21$. 89
5.9 Drop deformation and translation at different time instances for $R = 0.1$ and $Q = 1$ using the flow parameters $Ca_E = 0.12$ and $Re = 1$. We also plot the flow patterns at $t = 70$. 90
5.10 Drop deformation and translation at different time instances for $R = 0.025$ and $Q = 0.16$ using the flow parameters $Ca_E = 0.12$ and $Re = 1$. We also plot the flow patterns at $t = 140$. 91
5.11 Drop deformation and translation at different time instances for $R = 1.5$ and $Q = 10$ using the flow parameters $Ca_E = 0.12$ and $Re = 1$. We also plot the flow patterns at $t = 19$. 92
5.12 Drop deformation and translation at different time instances for $R = 25$ and $Q = 40$ using the flow parameters $Ca_E = 0.12$ and $Re = 1$. We also plot the flow patterns at $t = 24$. 92
5.13 A regime plot showing the various interaction dynamics between a pair of drops when subjected to an uniform electric field. The properties considered in the numerical study are $Ca_E = 0.12$, $Re = 1$, $\mu_r = 1$, and $\rho_r = 1$. An open circle (○) denotes drop coalescence, a cross mark (×) denotes thin film formation, and a square (■) denotes drop separation. . 93

6.1 Schematic diagram (not to scale) showing the initial configuration and boundary conditions in an axisymmetric cylindrical coordinate system (r, z). The radius of the drop is a. Electric field ($\mathbf{E}$) is applied along negative z axis. The size of the domain is $16a \times 16a$. Viscoelasticity of a phase will have both solvent (μ_s) and polymer (μ_p) viscosity. 100
6.2 Temporal evolution of the deformation parameter (D) for two different configurations. Other dimensionless parameters for the computations are $Ca = 0.6$, $Re = 0.3$, $De = 0.4$, and $\beta = 0.5$. 103
6.3 Temporal evolution of drop deformation (D) for different levels of grid refinement. The inset shows the zoomed view for better convergence analysis. The dimensionless parameters for the computations are $R = 0.5$, $Q = 2$, $Re = 1$, $Ca_E = 0.2$, $De = 1$, $Re_E = 0.01$, $\beta = 0.1$, $\mu_r = 1$ and $\rho_r = 1$. 104

6.4 Effect of De on deformation of drop for $Ca_E = 0.2$, $R = 10$ and $Q = 0.1$. The inset for NV configuration shows that at steady-state the deformation increases with an increase in De. 105
6.5 Steady-state deformation variation D/D_N (normalized with D at $De = 0$) with De for two different $Ca_E = 0.1, 0.2$. The electrical parameters are $R = 10$ and $Q = 0.1$. The effect of viscoelasticity is more prominent in the study of VN system. 106
6.6 Plot of electric stresses (a) normal τ_{en} and (b) tangential τ_{et} along the inside edge of the interface at $Ca_E = 0.2$, $R = 10$ and $Q = 0.1$. These stresses do not change with the flow field and only depend on the electric field strength. 107
6.7 Stresses along the inner edge of the interface for VN configuration at $Ca_E = 0.2$. (a) The viscous normal stress τ_{sn} and (b) the viscous tangential stress τ_{st}, due to the solvent in the Oldroyd-B fluid. (c) The polymer normal stress τ_{pn} and (b) the polymer tangential stress τ_{pt}, being the inward normal to the interface. The electrical parameters are $R = 10$ and $Q = 0.1$. 108
6.8 Stresses along the outer egde of the interface for NV configuration at $Ca_E = 0.2$. (a) The viscous normal stress τ_{sn} and (b) the viscous tangential stress τ_{st}, due to the solvent in the Oldroyd-B fluid. (c) The polymer normal stress τ_{pn} and (d) the polymer tangential stress τ_{pt}, being the outward normal to the interface. The electrical parameters are $R = 10$ and $Q = 0.1$. 110

C.1 A representation of the grid used to study drop impact dynamics. An axisymmetric system is used for the study. The grid has been mirrored for better visualization. We also show the initial configuration of the system. 139
C.2 Different zoom levels showing grid refinement for a single emulsion drop. The minimum grid level is $l = 6$ while the maximum grid level is $l = 12$. 140
C.3 Different zoom levels showing grid refinement for a double emulsion drop. The minimum grid level is $l = 6$ while the maximum grid level is $l = 12$. 140

Nomenclature

Roman Symbols

a	Undeformed drop radius
$\mathbf{A}$	Conformation tensor
B	Length of semi-minor axis
Bo	Bond number
C	Volume fraction
Ca_E	Electric capillary number
D	Deformation parameter
De	Deborah number
d	Distance from interface
D_o	Primary drop diameter
D_s	Secondary drop diameter
$\mathbb{D}$	Deformation tensor
$\mathbf{E}$	Electric field
$\mathbf{F}_e$	Electric force
F_h	Hydrodynamic force
Fr	Froude number
$\mathbf{F}_s$	Surface tension force

$\mathbf{g}$	Acceleration due to gravity
H	Heaviside function
$\mathbf{J}$	Current density
l	Grid refinement level
L	Length of semi-major axis
$\mathbf{n}$	Interface normal vector
Oh	Ohnesorge number
p	Pressure
Q	Permittivity ratio
q_s	Surface charge density
q_v	Volumetric charge density
$\mathbf{r}$	Position vector
R	Conductivity ratio
Re	Reynolds number
Re_E	Electric Reynolds number
$\mathbb{T}$	Stress tensor
$\mathbb{T}_e$	Maxwell stress tensor
$\mathbb{T}_p$	Polymer stress tensor
$\mathbb{T}_s$	Viscous stress tensor
$\mathbf{u}$	Velocity field
U	Impact velocity
U_e	Electrohydrodynamic velocity
We	Weber number

Greek Symbols

α	Cone vertex angle
β	Solvent viscosity ratio
δ_s	Dirac delta function
ϵ	Interface thickness
ε_0	Permittivity of free space
ε	Electrical permittivity
γ	Surface tension coefficient
κ	Curvature
λ	Relaxation parameter
μ	Viscosity
ϕ	Level set function
φ	Electric potential
ρ	Density
σ	Electrical conductivity
Ψ	Log of conformation tensor
Θ	Property
ζ	Ratio of electrostatic to hydrodynamic forces

Subscripts

1	Drop/Pool phase
2	Ambient phase
n	Normal component
p	Viscoelastic phase

s Newtonian phase

t Tangential component

Acronyms / Abbreviations

AMR Adaptive Mesh Refinement

BCG Bell-Colella-Glaz

CFL Courant-Friedrichs-Lewy

CLSVOF Coupled Level Set and Volume of Fluid

CSF Continuum Surface Force

EHD Electrohydrodynamics

ENO Essentially Non-Oscillatory

LS Level Set

MAC Marker and Cell

VOF Volume of Fluid

Chapter 1

Introduction

Drop interactions are significant in the microphysics of clouds and precipitation, which influence global climate and environmental change (Pumphrey and Elmore, 1990). Electric field enhances drop coalescence rates and is useful in many industrial applications ranging from liquid-liquid separation processes to microfluidic mixers (Kavehpour, 2015). Moreover, the polymer processing industries blend and mix different polymers to enhance their properties (Tucker and Moldenaers, 2002). The processes involving drop interactions and different rheological effects in the presence of an electric field show diverse phenomena.

An important application of drop-drop and drop-interface coalescence study is the separation of the water and oil phases in an emulsion (Eow and Ghadiri, 2003). Effective oil and water separation is crucial in a maritime oil spill cleaning operation. Dewatering of crude oil by petroleum industries is another area where oil-water separation finds its importance. The effectiveness of this separator is directly affected by oil viscosity and density. It is critical to deeply understand the tiniest components that directly impact these phenomena to create a highly efficient and resilient process. The backbone of such systems is drop-drop and drop-interface interactions. We also require a better understanding of the coalescence process, which directly affects various applications, including emulsification and de-emulsification processes. This thesis elucidates the understanding of these phenomena by studying the various attributes.

This chapter first introduces drop impact dynamics on a liquid pool (§ 1.1.1). We then describe the electrohydrodynamics of drops and emulsions (§ 1.1.2). Viscoelastic flow and its characteristic flow behavior are then outlined (§ 1.1.3). The literature gaps are then highlighted, and the thesis objectives are summarized (§ 1.3). The chapter concludes with an outline of the remainder of the dissertation (§ 1.4).

1.1 Literature review

1.1.1 Drop impact dynamics

The impact of a drop on the surface of deep liquid pool results in either coalescence with the receiving liquid or splashing. In addition, impinging drops may also bounce off or float on the liquid surface. Different flow characteristics are observed near the transition from coalescence to splashing (Yarin, 2006). The study of drop impacts on solid and liquid surfaces is significant due to its various technical and natural applications (Castillo-Orozco et al., 2015; Yarin, 2006). Some technical applications include ink-jet printing, oil spills, spray painting and coating, fuel injection, pyrometallurgical operations, plasma spraying, fire suppression by sprinklers, and soil erosion. Many large-scale and widespread natural phenomena, such as the aeration of the surface layers of lakes, seas, and oceans, depend on air bubble entrainment due to raindrop impacts. Such drop impacts lead to jets and secondary droplets forming, which evaporate and form salt crystals. Accordingly, drop impact analyses find their relevance in meteorological studies too. In the microfabrication industry, producing different components using precision solder-drop dispense, liquid atomization, and cleaning also involve drop impacts. Deicing aircraft and power lines using mechanical methods requires understanding the physical phenomena involving drop impacts.

Worthington (1908) was one of the first to systematically investigate the impact of a drop on a pool of liquid. His famous book A Study of Splashes documented the photographs of drop and solid-ball impacts on deep liquid pools. Figure 1.1 shows one such experiment where a drop of water impacts a pool of water, and we observe various phenomena, including the formation of a crater, central jet, and secondary drop. Despite the phenomena being ubiquitous, with over a decade of research, it still needs to be fully understood and continues to attract researchers.

Drop impact phenomena are remarkably diverse, depending on many factors. A drop may be spherical or elliptical (prolate or oblate) at impact. Studies are conducted for both normal and oblique impact on the free surface of a liquid in a deep pool, on a thin liquid film on a wall, or a dry solid surface. The liquid may be Newtonian or non-Newtonian (such as viscoelastic). The drop and pool liquid may be miscible or immiscible and can be at different temperatures. The outcome of the impact depends mainly on the impact velocity, size of the drop, the properties of the liquid (density, viscosity), the interfacial tension, and air entrapment. Accordingly, we can have coalescence or splashing. When a drop impacts a liquid pool, a crater may form

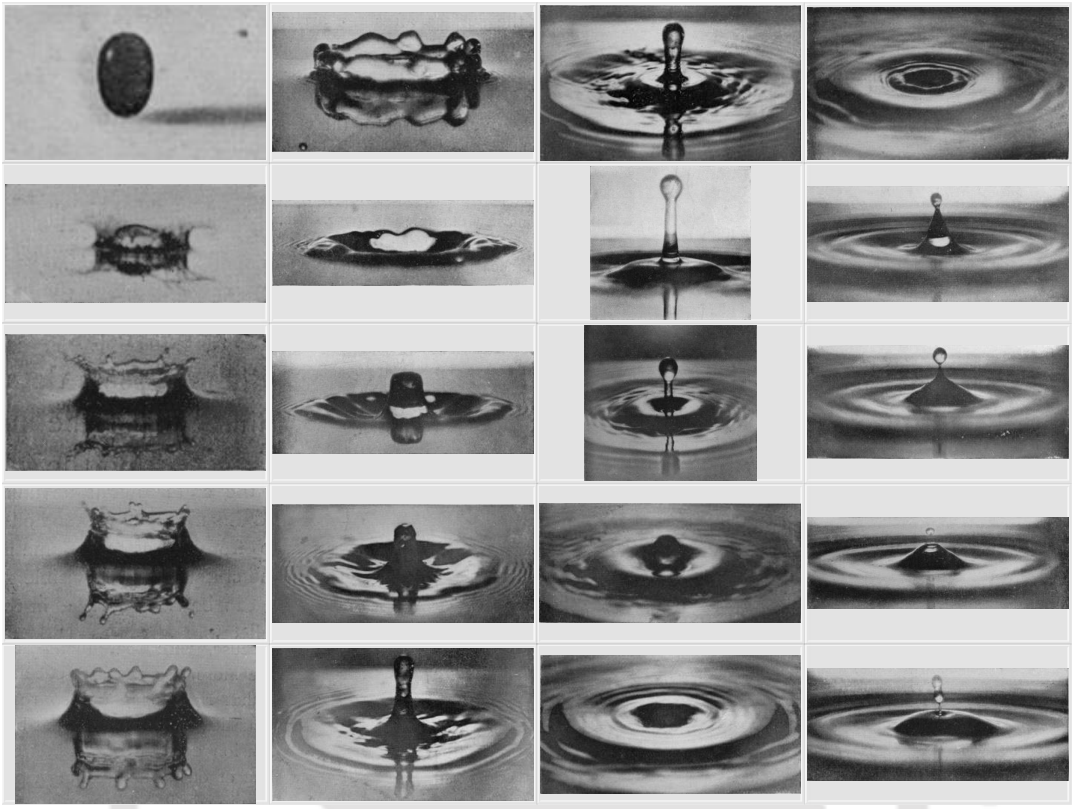

Fig. 1.1 Snapshots of splash of a drop of water 0.2 gm, 7.36 mm in diameter, falling from a height of 40 cm into water. Figures reproduced from Worthington (1908).

in the bulk of the liquid pool. This crater can collapse and form a jet that rises from its center, known as the Worthington jet. This central jet may be subjected to capillary breakup leading to the formation of secondary droplets. The objectives of studying such flows are to determine the dynamics responsible for the phenomena, understand the interaction of different forces, and determine the transition from one regime (coalescence) to another (splashing).

Researchers studied the transition regimes between coalescing and splashing drops using high-speed photography techniques. The mechanism of different flows was studied by the normal impact of water drops on the plane water surface. Although Pumphrey and Elmore (1990) determined the boundaries of regular bubble entrainment, the jet formation boundaries were only determined once Rein (1996) showed the various transition regimes experimentally. Figure 1.2 shows the transition from coalescence to splashing based on increasing Weber number (We). Rein (1996) distinguished coalescence from splashing by the presence of a vortex ring in the case of coalescence and a secondary droplet in the case of splashing and the bubble entrapment zone was

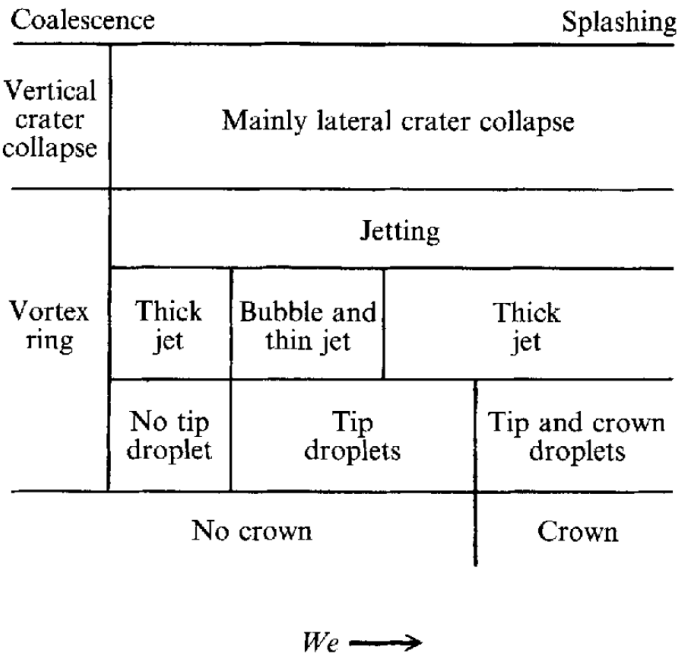

Fig. 1.2 Transition from coalescence to splashing. Reproduced from Rein (1996).

considered a particular case of splashing. The vortex ring formation and propagation owing to impacting water drops have been demonstrated experimentally by Durst (1996). The investigation enhanced the insight into the penetration of drops and the development of vortex rings generated by the impacting water drops. As the impact velocity of the drop is increased, the splashing regimes start. The main features of splashing are the formation of a crown and the rise of a liquid column in the middle of the crater (Engel, 1967; Leng, 2001). When the impact velocity is very high, the crown sometimes closes on itself and entraps a large bubble (Medwin et al., 1990). Furthermore, the cavity produced in the pool is deep, and its retraction leads to a central jet. The high-speed jet can disintegrate, yielding one or more drops upward (Berny et al., 2020; Castillo-Orozco et al., 2015).

Charles and Mason (1960) investigated the partial coalescence for liquid drop at a liquid-liquid interface and suggested a cascade phenomenon controlled by the Rayleigh capillary instability. A review of different stages of coalescence of liquid on a planar interface, with the significance of different types of stresses, was presented by Kavehpour (2015). Pinch-off was considered the only mechanism for the early dynamics of coalescence. Thoroddsen and Takehara (2000) suggested that the surface tension time scale should be accounted for partial coalescence while studying the coalescence dynamics at a liquid-air interface for water, ethanol, and mercury drops. Utilizing

ultra-high-speed video, Blanchette and Bigioni (2006) presented a phase diagram as a function of the Ohnesorge and Bond numbers for the coalescence of ethanol-water and ethanol-glycerin drop at the liquid-air interface. Aryafar and Kavehpour (2006) used water, methanol, and silicon oil and presented the coalescence condition. Honey and Kavehpour (2006) developed a theory for the maximum height of the bouncing drop, which matched well with the experimental results. Additional studies on jet breakup have been conducted to understand the effects of drop size, interfacial tension, and viscosity (Chen et al., 2006; Manzello and Yang, 2002). Chen et al. (2006) reported three sub-regimes within the partial coalescence regime for the coalescence of water and water-glycerol drops at the liquid-liquid interface and presented a scaling relationship for the drop size ratio and the coalescence time. Gilet et al. (2007) reported cascading outcomes for mercury and less viscous drops in their experiments. A transition regime from partial to complete coalescence was observed when the neck radius oscillated twice (Ray et al., 2010). Regime maps have been developed for vortex ring formation, bubble entrapment, and jet formation based on the Weber, Froude, and capillary numbers (Agbaglah et al., 2015; Ray et al., 2015). However, all regimes were not captured due to the limited range of these parameters. In an attempt to explain the impact dynamics, Ray et al. (2015) performed extensive numerical calculations to simulate the transition from coalescence to splashing. Their study concluded that after the crater reaches its maximum depth, the crater base retracts differently for different parametric ranges, which leads to different phenomena. They identified two new zones: the small thick jet regime with and without a secondary drop and the small bubble entrapment with a long thick jet. They also investigated the vortex ring generated during the impact and observed that it moved with the capillary waves.

Rocco et al. (2010) simulated drop impact on a thin layer of the same liquid in quiescent air. They developed a volume of fluid based simulation tool to depict deposition, spreading, and splashing for a range of Weber and Reynolds numbers. Coppola et al. (2011) extended the analysis for the splashing regime. They identified the appearance of an initial horizontal ejecta sheet, followed by an almost vertical lamella sheet formation. Furthermore, they developed insights into the relevant scaling laws. For a higher Froude number and thus a higher Weber number, the long thick jet phenomena begins. This can be explained by the high inertia force, which produces high amplitude capillary waves traveling towards the crater base. During this stage, the crater base retracts differently for different parametric ranges leading to different phenomena as shown by, for example, Leng (2001) experimentally and Ray et al. (2015)

numerically. Michon et al. (2017) conducted experiments investigating drop impact dynamics in a deep liquid pool. By varying different parameters, they could define two regimes: the singular jet and the cavity jet, depending on the mechanism of cavity retraction and subsequent jet dynamics. An extensive study of the singular jet regime was conducted by Thoroddsen et al. (2018). In their experimental study, they observed fast, thin jets due to the formation of a sub-crater at the base of the collapsing cavity, which they termed dimple. By performing experiments on a water drop impacting a horizontal free water surface, Ma et al. (2019) showed that the size of the daughter drop could be even bigger than the primary drop. Kim et al. (2021) investigated the impingement dynamics for a two-layer liquid and suggested using an effective Weber number to characterize the crater and jet dynamics.

1.1.2 Electrohydrodynamics

The interaction of fluids and electric fields occurs in natural phenomena such as the disintegration of raindrops in thunderstorms and has many practical applications such as electrosprays, microfluidic devices, crude oil demulsification, electrocoalescence, electrorheology, electrospray, electrospinning, and inkjet printing. These systems typically consist of two immiscible fluids, and thus an interface exists between them. Depending on the particular application, the interface may deform or rupture under the applied electric field. Hence it becomes crucial to understand the interfacial effects to accurately predict the response to an electric field. Interesting applications utilizing the convection currents generated in droplets due to electric fields are emerging. For example, Penkova et al. (2006) showed that the electric field driven flow in a droplet affects the nucleation of protein clusters. Chung and Oliver (1990) showed that the electric field induced circulation results in enhanced heat transfer in a spherical droplet translating in a dielectric medium. Electric field also affects the wetting characteristics, which can be harnessed for various applications in microfluidics (Romero Herreros, 2014). An electric field can also be employed to control the size of droplets and bubbles from a nozzle, as shown in Notz and Basaran (1999) and Sunder and Tomar (2013). Application of an electric field across an emulsion has been shown to affect the stability of emulsions (Barnes, 1994; Kilpatrick, 2012). Effect of electric field on a liquid drop has been studied extensively since the time of Rayleigh (1882). Garton and Krasucki (1964) observed in their experiments that bubbles in insulating liquids deform in prolate shapes and showed that with an increase in electric field beyond a critical value, the bubbles can become unstable.

We consider an uncharged, neutrally buoyant spherical drop of radius a suspended in another immiscible fluid, as shown in Figure 1.3. The viscosity, permittivity, and electrical conductivity of the fluids are denoted by μ, ε, and σ, respectively, with subscript 1 denoting the drop phase and 2 denoting the medium phase. When a uniform electric field of strength E_∞ is applied, the interface of the drop acquires charge, and the drop gets polarized. This is due to the difference in permittivity or conductivity between the drop and the suspending fluid. Consequently, electric stresses are generated at the interface, which tends to deform the interface. These electric stresses are nonuniform along the interface, with the maximum occurring at the poles ($\theta = 0, \pi$) of the drop, and vanishes at the equator ($\theta = \pi/2, 3\pi/2$).

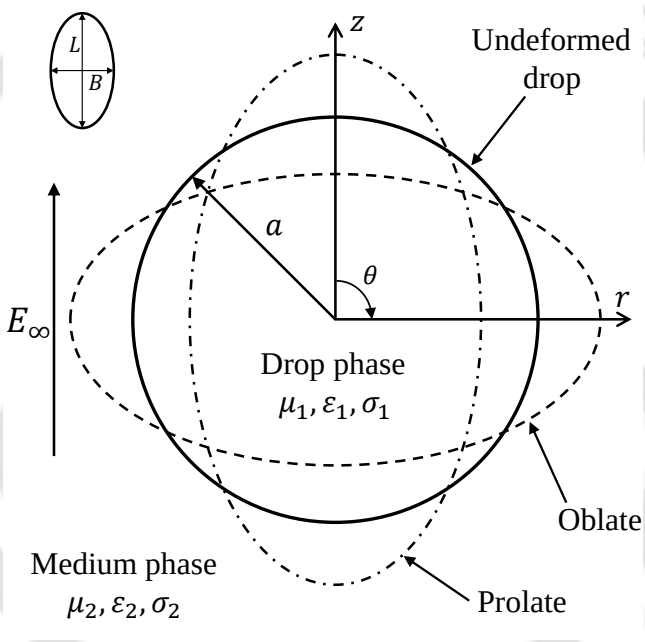

Fig. 1.3 Schematic representation of the deformation of a drop with radius a suspended in another fluid in the presence of an electric field **E**. The initial undeformed state of the drop is shown using a solid line. The possible steady-state deformed shapes, prolate and oblate, are also illustrated. The relevant properties of the drop (1) and suspending medium (2) are the viscosity μ, dielectric permittivity ε, and electrical conductivity σ. The semi-major and semi-minor axis of the deformed drop are denoted by L and B, respectively.

If the drop and medium phases are perfectly dielectric, the interface does not acquire a charge, and the surface charge density is zero. When a perfectly conducting drop is placed in a perfectly dielectric medium, the tangential component of electric stress does not exist. Therefore, the tangential component of the electric traction vanishes

for a perfectly conducting or perfectly dielectric drop in a perfectly dielectric medium. The surface tension then balances the normal component of the electric stress. The drop deforms along the direction of the electric field into a prolate shape, and the fluids are quiescent. This phenomenon is termed electrohydrostatics (Allan and Mason, 1962; O'Konski and Thacher, 1953; Saville, 1997; Taylor, 1964). An example of a conducting drop in a dielectric would be water drops suspended in oil, which is prevalent in oil refining processes (Eow et al., 2001; Mhatre et al., 2015b). Dielectric-dielectric systems are encountered in the electrospinning of polymer melts (Reznik and Zussman, 2010). Allan and Mason (1962) calculated the steady-state deformation attained by the drop under a weak electric field. For a perfectly conducting drop suspended in a perfectly dielectric medium

$$D = \frac{L - B}{L + B} = \frac{9}{16} Ca_E \ , \tag{1.1}$$

and when both the phases are perfectly dielectric

$$D = \frac{9}{16} \frac{(Q-1)^2}{(Q+2)^2} Ca_E \ . \tag{1.2}$$

Here Q is the ratio of the electrical permittivity of the drop phase to the medium phase, and Ca_E is the electric capillary number defined as the ratio of electric stresses to capillary stress. This theory was derived in the limit $Ca_E \ll 1$, and the deformation scales linearly with the electric capillary number $D \sim Ca_E$. Allan and Mason (1962) confirmed their theoretical predictions against experimental measurements and verified the prolate deformation of a conducting drop. However, for dielectric drops, they discovered that in addition to prolate deformation, there were some cases where oblate deformation of drops was sustained. They were unable to explain their observations using the existing theories (Allan and Mason, 1962; O'Konski and Thacher, 1953).

Investigations were carried out further, concluding that perfect dielectric systems were difficult to encounter in practice. Even the most insulating system had a small but measurable value of electrical conductivity due to the presence of impurities. For instance, the electrical conductivity of silicone oil and castor oil $\sim \mathcal{O}\left(10^{-12} - 10^{-11}\right)$ S/m (Allan and Mason, 1962). Such systems showed oblate deformations when subjected to an electric field. Taylor (1966) explained this observation using a leaky dielectric model. He postulated that although the bulk of the fluids remained electroneutral, the weak conductivities of the fluids allowed the interface to acquire charge under an electric field. These finite charges at the interface create a jump in the tangential electric stresses, which are balanced by the viscous shear stresses. Thus a fluid flow is generated in both

phases even after the drop reaches a steady deformed state, and this phenomenon is known as electrohydrodynamics. Taylor (1966) derived the deformation of the drop by balancing the electric, viscous, and capillary forces acting at the interface as

$$D = \frac{9}{16}\frac{Ca_E}{(2+R)^2}\left[R^2 + 1 - 2Q + \frac{3}{5}(R-Q)\frac{2+3\mu_r}{1+\mu_r}\right], \tag{1.3}$$

where R is the ratio of the electrical conductivity of the drop phase to the medium phase, and μ_r is the ratio of viscosity of the drop phase to the medium phase. This theory was again valid for weak electric fields only $Ca_E \ll 1$. Subsequent to the deformation predictions by Taylor (1966), several improvements on the solution have been proposed. Second order corrections to drop deformation were given by Ajayi (1978), followed by the effect of charge convection on drop deformation as discussed in (Feng and Scott, 1996; Lanauze et al., 2015; Xu and Homsy, 2006). The leaky dielectric theory is presented in detail in Melcher and Taylor (1969) and has been extensively used since then to explain the behaviour of an isolated drop in an emulsion.

As discussed above, drops can undergo prolate or oblate deformations when subjected to an electric field. The theoretical model of Taylor predicts drop deformation very well for low electric field strength. If the electric field strength is increased, the model no longer remains valid, and the drop is susceptible to instabilities and breakup. The steady and transient deformation of drops at weak electric fields is vastly studied and well understood (Saville, 1997). The transient deformation of a drop depends on the Reynolds number (Re). If $Re \ll 1$, the drop monotonically reaches a steady state during its transient evolution. In contrast, if $Re > 1$, the drop has oscillating characteristics before it reaches a steady state (Jiang et al., 2020). Feng and Scott (1996) showed that inertial effects might change a drop shape from oblate to prolate. Lanauze et al. (2013) and Das and Saintillan (2017a) showed that surface charge convection causes the formation of charge shocks near the equator of an oblate drop. It was observed that the inclusion of charge convection effects resulted in a reduction in interfacial velocities. The importance of the ratio of charge relaxation time scale with the time scale of other processes such as charge convection due to fluid flow or drop deformation due to local shear have been discussed by Collins et al. (2013). When the strength of the electric field is high, the drops become unstable and break into daughter drops. Many studies were conducted to distinguish the critical parameter for the break up of a prolate drop (Collins et al., 2013; Das and Saintillan, 2017a; Lac and Homsy, 2007; Lanauze et al., 2015). Two broad modes of breakup were reported.

In one case, the drop elongates to a cylindrical shape, develops a neck, and breaks, producing daughter drops. This is known as end pinching. The other mode, called tip streaming, is characterized by the formation of pointed conical ends at the poles of the drop from which smaller drops are ejected. The transition between these modes is complex and depends on various parameters. A high-conductivity drop ejects thinner jets, and smaller daughter drops via tip streaming.

For a low-conducting drop, the jet vanishes, and the breakup is via end-pinching due to the rapid domination of capillary stresses. Sherwood (1988) studies drop deformation under strong electric fields using a boundary integral method. Lac and Homsy (2007) used an axisymmetric boundary integral method to study the stability of drops. Bentenitis and Krause (2005) theoretically studied drop deformation by extending the conventional leaky dielectric model in a framework of spheroidal deformation. Abbasi

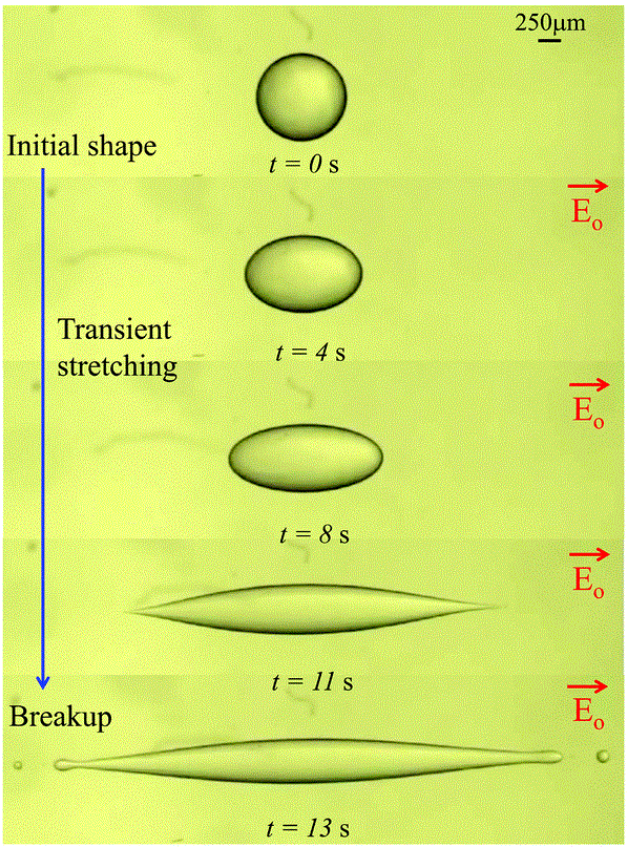

Fig. 1.4 Shape evolution of castor oil drop in silicone oil. The drop begins with as spherical shape to transient stretching and consequent breakup from the ends. The critical electric capillary number for the breakup is $Ca_E \sim 0.26$. Figures reproduced from Abbasi et al. (2019a).

et al. (2019a) performed experiments and found the critical electric capillary number for the breakup of prolate drops. Figure 1.4 shows one such study where the instability for a castor oil drop in silicone oil occurred at $Ca_E \sim 0.26$. For oblate-shaped drops, when the electric field strength is increased, the drops undergo electro-rotation due to surface charge convection effects. This is known as Quincke rotation, where the induced dipole tries to align itself with the applied electric field (Das and Saintillan, 2017a,b; Ha and Yang, 2000b; Salipante and Vlahovska, 2010). The electro-rotation stabilizes the drop against breakup by suppressing drop deformation. Brosseau and Vlahovska (2017) conducted experiments and found that drops can undergo dimpling and equatorial streaming. The drop forms a torus shape in the former mode and eventually breaks. In the latter mode, the drop flattens and forms thin edges, breaking into tiny droplets.

Recent studies investigated the effects of an electric field on double emulsion (compound) drops due to their vast applications (Enayati et al., 2010, 2011). An A/B/A type of compound drop has the same fluid in the core and ambient, while the A/B/C type has three distinct fluid components. For an A/B/A type, only two modes of core-shell deformation are possible: prolate-oblate and oblate-prolate. In A/B/C types of double emulsions, four possible core/shell-shell/ambient deformations are: prolate-prolate, prolate-oblate, oblate-prolate, and oblate-oblate. These deformation types depend entirely on the ratio R/Q. The effect of the electric field on compound drops has been studied theoretically and experimentally (Behjatian and Esmaeeli, 2013, 2015; Reznik et al., 2006; Soni et al., 2013). Most of these studies on compound drops have focused on the relative deformation of the inner and the outer drops and the possibilities of breakup and release of the inner drop into the ambient fluid. Gouz and Sadhal (1989) used a bipolar coordinate system to examine various configurations of compound drops under which a compound drop is stable in a translational flow for a given set of suitable electrical conductivities and permittivities of the constituting fluids. Ha and Yang (1999b) used the domain perturbation method, similar to Taylor (1966), to predict the equilibrium shapes of the inner and the outer drop and also computed the rheological response of a dilute double emulsion of compound drops. Tsukada et al. (1993) using theoretical analysis, showed that the deformation is related to the core-shell drop volume ratio. Studies on A/B/C type emulsions were conducted by Behjatian and Esmaeeli (2013). They used a domain perturbation method to study the charge distributions around the interfaces. They also found the deformation types to depend on the R/S ratio. Abbasi et al. (2017) showed that if the shell fluid was highly

conducting, it behaved like a shield, and the core had negligible deformation. Only a few studies are present in the literature regarding the breakup of double emulsions. Ha and Yang (1999a) performed experiments using castor oil and water emulsions and observed pinch-off and tip-streaming modes of breakup. Abbasi et al. (2017), using a level set method, studied the various modes under which a double emulsion may break up. They showed that the inner drop might undergo large oblate deformation. In contrast, the outer drop undergoes prolate deformation and thus can lead to the bursting of the compound drop, ejecting the inner drop fluid into the ambient. They also showed that if the inner drop is not concentrically placed, it may migrate to the outer surface of the compound drop and be ejected out for particular conductivity and permittivity ratios. Abbasi et al. (2019b) also conducted experiments on A/B/C type double emulsions and reported unidirectional and bidirectional breakups, as shown in Figure 1.5. Due to the charge convection effects, the breakup of the core changed from

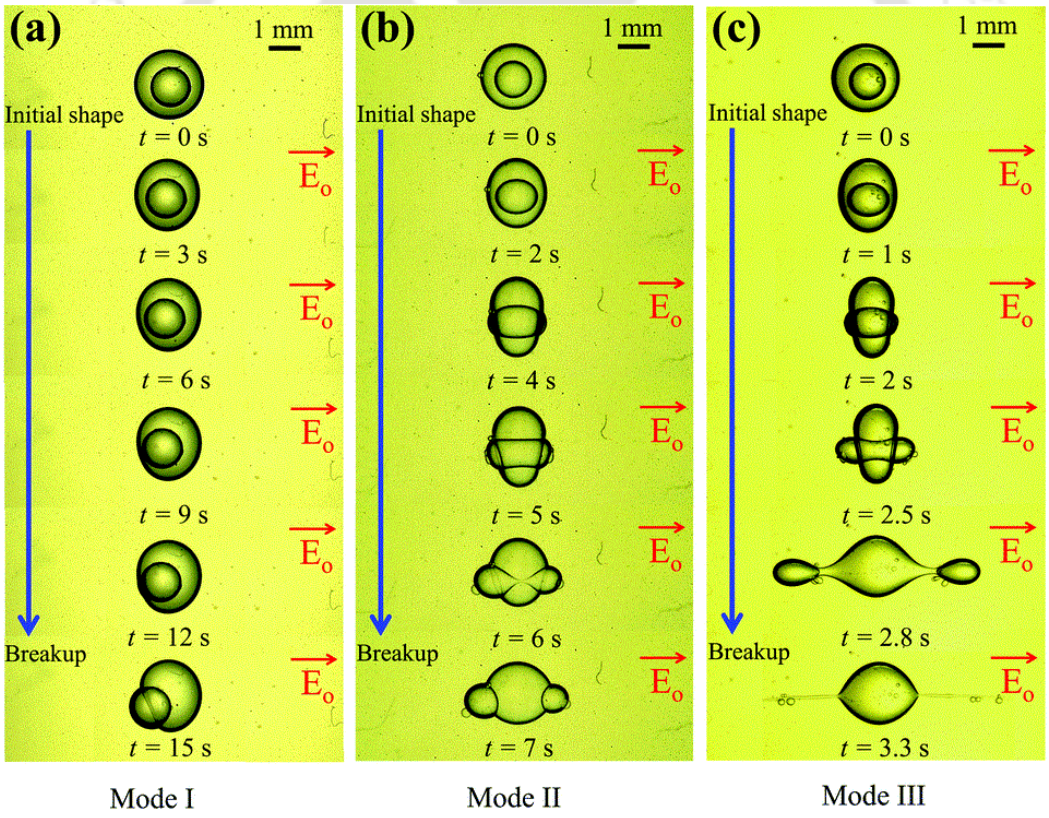

Fig. 1.5 Breakups of the A/B/C type emulsion drop under an electric field. The surface tension between the shell and ambient, the permittivity of the ambient fluid, and the core and shell diameter are kept constant. The electric field and the surface tension between the core and shell are changed to study the breakup modes. Figures reproduced from Abbasi et al. (2019b).

bulbous lobes to conical ends.

An emulsion is rendered unstable when the drops attract, whereas the emulsion is stable when the drops repel. Drops attract each other if the flow due to the electric stresses at the drop surface is from the poles towards the equator, thus resulting in a velocity field that pulls the drops together along the axis, with the externally applied electric field direction aligned with the axis. On the other hand, drops repel each other when the flow is from the equator to the poles. The flow direction can be predicted by comparing the drop to ambient electric conductivity and permittivity ratios, R and Q, respectively. If $R < Q$ flows from poles to the equator, and thus drops attract, whereas when $R > Q$ flow is from the equator to poles. Where considerable effort has been invested in understanding the behavior of isolated drops and emulsions in an electric field, the effect of interactions between the drops on the rheology and stability of the emulsion must be understood better for dense emulsions. There are considerable studies on the interaction between drops and particles suspended in a perfect insulator in the presence of an externally applied electric field (Arp et al., 1980; Latham and Roxburgh, 1966). Due to the relevance to the oil industry and atmospheric science, interactions between conducting drops suspended in an insulating fluid (such as in water-in-oil systems and water droplets in clouds) in the presence of an electric field have been studied extensively (Atten, 1993; Brazier-Smith, 1971;

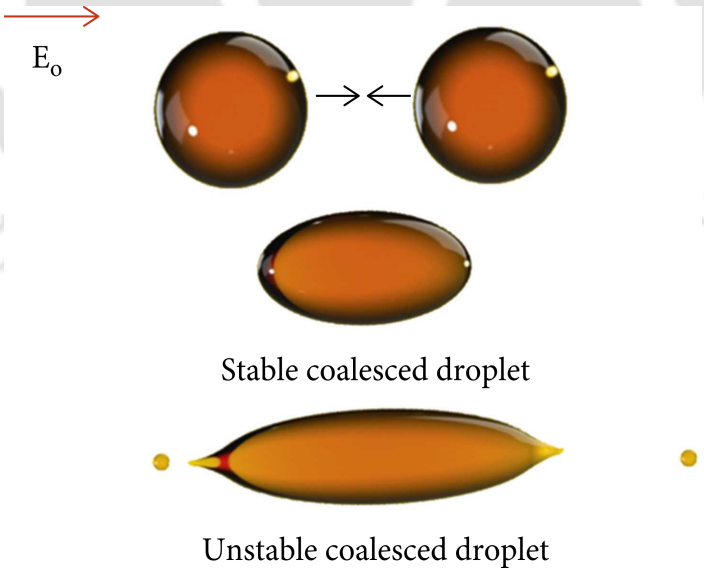

Fig. 1.6 Coalescence of castor oil drops in silicone oil. Stable and unstable coalescence were observed due to the applied electric field strength. At stronger electric fields, the coalesced droplet became unstable, continuously stretched after the merger, and began to eject droplets at the side ends. Figures reproduced from Abbasi et al. (2022).

Pearce, 1954). A curious phenomenon of electrocoalescence, or rather the phenomenon of non-coalescence, of charged drops in an electric field has also revived some interest lately in the study of interactions between a pair of drops in the presence of an electric field (Anand et al., 2019; Aryafar and Kavehpour, 2007; Ristenpart et al., 2009). For uncharged drops in perfectly dielectric fluids, the drops always attract each other due to dipole-dipole electrostatic interactions. Thus, the approach velocity in viscous fluids is proportional to h^{-4}, where h is the separation distance between the drops. Interaction between a pair of leaky dielectric drops suspended in a leaky dielectric fluid was first studied theoretically by Sozou (1975). He used bispherical harmonics, considering the two drops to be the same size, to solve for the electric and velocity fields due to the tangential electric stresses at the drop interface. The key conclusions were the increase in the non-uniformity in the electric field in the region between the drops when their approach distances were shorter than twice the diameters. Zhang et al. (1995) used a population dynamics approach to study the interaction between drop pairs, but their study was conducted using perfectly conducting drops dispersed in a perfect dielectric liquid. Using a boundary integral method, Baygents et al. (1998) performed axisymmetric simulations of interactions between two leaky-dielectric drops in leaky-dielectric ambient fluid with the axis of symmetry aligned with the electric field. They showed that the hydrodynamic forces dominate the electrostatic forces in the limit of a small Reynolds number and dictate the stability of emulsions. They also showed that the relative velocity between the drops of perfectly dielectric systems is governed by h^{-4}. They showed that, in contrast, for leaky dielectric fluids, drops attract or repel at a rate proportional to h^{-2} due to the hydrodynamic forces. Tomar et al. (2007) proposed a CLSVOF based method to simulate two-phase electrohydrodynamics and showed good agreement with the results of Baygents et al. (1998). Lin et al. (2012) used a phase-field method to simulate the interaction between a pair of drops in the presence of an electric field. The effect of the viscosity ratio on the time scale of coalescence was discussed, but the scaling for the relative velocity between the drops was not examined.

1.1.3 Viscoelastic flows

Polymeric fluids, also called viscoelastic fluids, exhibit viscous and elastic properties. These viscoelastic fluids contain long chains of high molecular weight polymer molecules and can adopt various configurations and orientations. The interaction of these polymer chains with each other and the surrounding fluid particles creates a complex internal

microstructure in the polymeric liquid, giving rise to its characteristic flow behavior. Silly putty is a classic example of a viscoelastic fluid with such complex behavior. When this putty is left to relax on a wire mesh screen for an extended period, it flows through the screen like a viscous fluid but when dropped onto the floor it bounces like an elastic solid. When evaluated over an extended length of time, a viscoelastic substance exhibits viscous behavior, but when viewed over a short period, it exhibits elastic behavior (Bird et al., 1987a; Morrison, 2001). These viscoelastic fluids are used in a wide range of manufacturing and processing industries due to their mechanical properties, including the production of synthetic fibers, paints, shampoos, blend compatibilizers, adhesives, emulsion stabilizers, packaging, coating, biocompatible materials, polymer processing, and plastic manufacturing.

The viscosity of Newtonian fluids is independent of shear rate, whereas viscoelastic fluids have shear rate dependent viscosity. The polymeric fluids whose viscosity decreases with shear rate are termed shear thinning or pseudoplastic fluids. In contrast, those whose viscosity increases with shear rate are termed shear thickening or dilatant fluids. Newtonian fluids flow as long as stresses are applied and come to rest when they are removed. The internal strains in viscoelastic fluids do not disappear instantly and continue distorting the fluid even without external loads. The time during which the internal molecular configuration can withstand these internal stresses is called the relaxation time. These relaxation time constants give rise to fading memory effects in viscoelastic fluids. When externally applied stresses are removed, a viscoelastic fluid shows reverse deformation or a recoil similar to the retraction of a rubber band. Accordingly, analysis of this fading memory effect is essential in study of viscoelastic fluids.

In viscoelastic fluids, an additional tension force is developed along with the viscous stresses along the flow direction. This force, known as normal stress, is caused by the alignment and stretching of polymer molecules in the flow direction. Several deviations from the Newtonian flow behavior observed during the viscoelastic fluid flow arise due to this normal stress difference. The normal stress difference is observed even in shear flows. Several viscoelastic phenomena, such as rod climbing, die swell, and extruded swell effects are due to the normal stress difference (see Figure 1.7). When subjected to elongational flows, polymer molecules experience extensive stretching resulting in strong elastic force and large elongational viscosity. The tubeless siphon effect and polymeric jets both exhibit this behavior. Additional features exhibited by viscoelastic fluids include drag reduction in turbulent pipe flow, enhancement of the corner vortices

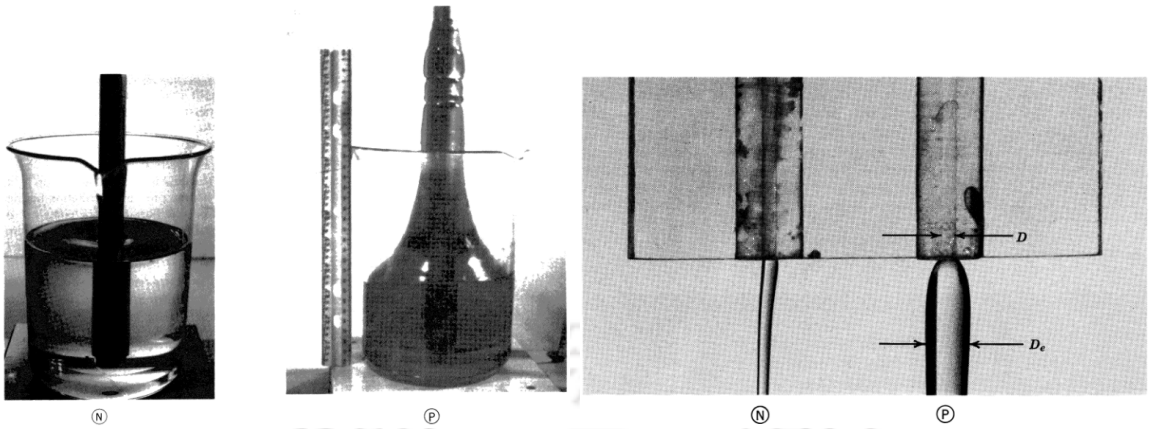

(a) Rod Climb (b) Die Swell

Fig. 1.7 Viscoelastic flow behavior due to the normal stress difference. (a) Fixed cylinder with rotating rod. The Newtonian liquid (glycerin) shows a vortex. The polymer solution (polyacrylamide in glycerin) climbs the rod. (b) Flow from orifices. The Newtonian fluid, (silicone oil) shows no diameter increase upon emergence from capillary tube. The polymer solution (polymethylmethacrylate in dimethylphthalate) shows an increase by a factor of 3 in diameter as it flows out of the tube. Figures have been reproduced from Bird et al. (1987a).

through the contraction, and sharkskin instability arising during the extrusion of the polymer melts (Bird et al., 1987a; Renardy, 1989).

The governing equations for Newtonian flows are inadequate in describing the viscoelastic behavior, as stress is not a linear function of the velocity gradient. Strains, strain rates, and strain history define the stress in viscoelastic fluids. A constitutive relationship that takes into account the influence of the stress tensor, flow kinematics, and material parameters is preferable for predicting viscoelastic flow events. This constitutive equation should handle flows with high strain and strain rate and display strain rate and time-dependent viscosity. It should also account for the presence of first and second normal stress difference, stress growth at the onset of deformation and stress relaxation after flow cessation, elastic recoil, sensitivity to deformation type, stress overshoot, and nonlinear relaxation. Brownian forces, hydrodynamic interaction, excluded volume, internal viscosity, self-entanglement, finite extensibility, and solvent-polymer interaction should also take into consideration (Larson, 1988; Oldroyd, 1950).

Developing a constitutive equation that encompasses all of the above-mentioned viscoelastic fluid processes is mathematically demanding. Even if such models are developed, they will be difficult to evaluate analytically, even for simple flows, and

a numerical solution would require substantial computational resources. Researchers have developed closed-form constitutive relations by relaxing some of the rheological properties. Constitutive equations are modeled following either continuum or microstructural approach. In the continuum approach, constitutive equations are developed at the macroscopic level, following certain principles and simplifications using mathematical approximations (Larson, 1988; Owens and Phillips, 2002). The continuum based constitutive equations are of either differential type (comprising of time derivatives of strain rate tensor) or integral type (comprising integrals of strain history). In the macroscopic approach, constitutive equations are developed by exploiting the kinetic theory of polymeric liquids. The microstructure of a polymeric material is represented by considering many micromechanical elements (beads and springs in a dumbbell model). Based on physical principles, a stochastic differential equation characterizes these micromechanical components and the motion of polymer molecules. These equations relate the microscopic forces with the macroscopic stress and strain (Bird et al., 1987a,b).

A suitable constitutive equation must be selected for investigation based on the polymeric material and flow conditions. The validity of the constitutive equation is typically tested with the rheological behavior exhibited by the viscoelastic fluids in a simple flow such as pure shear or elongational flows. However, most industrial processes involve complex flows, a combination of shear and elongational flows. The suitability of a constitutive equation in describing the behavior of viscoelastic fluids in complex flows can be evaluated by comparing experimental rheological data with numerical analysis. In this thesis, we will consider the constant shear viscosity behavior of Boger fluids modeled using the Oldroyd-B constitutive equation.

Most of the studies in the literature have focused on the interfacial phenomena of Newtonian fluids, but as summarized earlier, numerous applications involve processing polymer emulsions. Thus it is crucial to understand the behavior of polymer fluids to develop emulsions with improved properties. The rheological response of the polymer blends and emulsions can be investigated by studying simple flows, such as a drop subjected to either shear or extensional flow. Hence the preliminary experimental (Mighri et al., 1997; Tretheway and Leal, 2001) and numerical (Hooper et al., 2001; Ramaswamy and Leal, 1999a,b) studies investigated the influence of a uniaxial extensional flow field on the drop dynamics. These studies considered either the drop or ambient phase to be viscoelastic. They concluded that the presence of a viscoelastic drop in a Newtonian matrix suppresses its deformation, while the viscoelastic matrix is found to enhance the

drop deformation. These studies were extended to analyze drop dynamics subjected to a shear flow field (Elmendorp, 1986; Mighri et al., 1998). Similar to earlier results, drop viscoelasticity was found to restrict the drop deformation in these studies. In contrast, for the matrix viscoelasticity, some studies displayed enhanced drop deformation while others showed suppression of deformation (Guido et al., 2003; Sibillo et al., 2004). This contradictory behavior was examined by Yue et al. (2005), who reported that the deformation of a Newtonian drop in a viscoelastic matrix is nonmonotonic. Theoretical investigations by Maffettone and Greco (2004) and Minale (2004), who derived the phenomenological model to predict the transient drop shapes and deformation, agree well with previous studies (Aggarwal and Sarkar, 2007, 2008). Numerical experiments were also conducted to understand the viscoelastic flow dynamics (Boyko and Stone, 2022; Lee et al., 2021; Wang et al., 2023). Studies were also conducted to analyze the motion of a bubble through the viscoelastic medium (Funfschilling and Li, 2001; Herrera-Velarde et al., 2003). Different flow features such as teardrop shaped bubble, formation of negative wake, and rise velocity jump discontinuity were reported (Lind and Phillips, 2010; Pillapakkam et al., 2007). Effects of viscoelasticity on the drop dynamics through the complex microchannel were also explored (Chung et al., 2009; Harvie et al., 2008). Only a handful of studies in the literature explore the effects of viscoelasticity in electrohydrodynamic flows. Ha and Yang (2000a) experimentally observed the effects of viscoelasticity on the deformation and breakup of a drop in a uniform electric field. They concluded that the critical electric field strength of viscoelastic drops was increased. Lima and D'Ávila (2014) performed numerical simulations and found that the drop deformation decreased with increased relaxation time. Electric field magnitude primarily influenced the deformation, but other parameters also played a role.

1.2 Motivation

The motivation for studying various drop dynamics is to understand better the rich underlying physics involved with such flows. We investigate different Newtonian and viscoelastic fluid processes in the presence and absence of an electric field. The thesis presents a numerical investigation of such systems. The dynamics related to the formation of a secondary drop, especially to determine the conditions under which a larger secondary drop forms, must be explored in detail. Experiments have shown that a water drop impacting a pool can form a secondary drop larger than the primary

drop. The scaling for the relative velocity between the interacting drops is studied, which can vary depending upon the Reynolds number of the flow generated by the tangential electric stresses. The drops can attract for particular electrical properties. However, the coalescence phenomenon is delayed due to the slow drainage of the film between the drops, and a drop-pair doublet is formed. These nonlinear effects due to the finite Reynolds number have not been explored earlier. Drop dynamics due to an electric field in the presence of a viscoelastic medium have not been investigated. The mechanism of deformation and stability of drops are yet to be understood.

1.3 Objectives

Many studies have investigated the dynamics of drop-drop and drop-surface interactions. Although many mechanisms are well understood from past research works, there are still some unanswered questions due to the inherent complexity of the problem. We require a detailed understanding of the underlying physics to get the broader picture, which motivates these studies. The above summary, drawn from the literature gaps, forms the objectives for the present thesis.

1. To understand the secondary drop formation mechanism and determine the conditions under which a larger secondary drop forms.
2. To investigate the drop-drop interactions in single and double emulsions in the presence of an external electric field.
3. To investigate the effect of inertia in drop interaction in the presence of an external electric field.
4. To understand the various rheological effects under the influence of an electric field.

1.4 Outline of thesis

The present chapter describes the various drop dynamics and provides a detailed literature review. The literature gaps are highlighted, and the objectives are discussed. This thesis solely deals with numerical investigations to understand the various drop dynamics. Chapter 2 describes the in-house and open-source solvers utilized for the studies. Chapter 3 explores the phenomena of impact of a water drop on a deep

pool of water. Three scenarios emerge with the formation of a central jet and the pinch-off of one or more secondary drops. We also identified the regime for the formation of a secondary drop larger than the primary drop. Chapter 4 investigates the interaction dynamics of a pair of leaky dielectric drops suspended in leaky dielectric fluid. Both single and double emulsions are examined, and a new scaling for flow velocity is proposed. The interaction dynamics are suggested to be driven by the relative strength of the electrostatic and hydrodynamic forces. Chapter 5 furthers the previous investigation for pair of single emulsions. We consider the effects of a finite Reynolds number and study the drop dynamics. A regime map is drawn to demarcate the different interacting phenomena. Chapter 6 examines the effect of viscoelasticity on drop deformation in electrohydrodynamic flows. The transient and steady-state deformation are studied for two configurations: a viscoelastic drop suspended in a Newtonian matrix, and a Newtonian drop suspended in a viscoelastic medium. Finally, Chapter 7 concludes the thesis with a summary of the main contributions and highlights the scope of future research.

Chapter 2

Formulation and numerical modeling

In the previous chapter, we discussed the various physical phenomena that included complex flow mechanisms. Such complex flow dynamics results from the interplay between different forces. Generally, these dynamics are studied in three ways: (1) Experimental investigations, wherein the phenomena are studied using a scaled model in a laboratory environment; (2) Analytical techniques are used to solve the governing equations by applying first principle methods (in the case of multiphysics problems, these solutions become challenging); and (3) Computational studies, where the mathematical equations are solved by utilizing numerical techniques to find approximate solutions, and the accuracy depends on various parameters. Although experimental studies will remain the intrinsic source of information, numerical techniques become advantageous in investigating large parametric data sets. Nevertheless, experiments will be employed subsequently to validate the numerical results.

Studies involving two fluid phases are referred to as two-phase flows, whereas multiphase flows consist of a broader category of problems, including particle-laden flows. This thesis deals with two-phase flows with a sharp interface separating the phases. Typically for two-phase flows, the governing equations are defined separately for each phase, and a jump condition is used to couple the solution at the fluid interface. However, it is possible to adapt one set of governing equations for the whole flow domain occupied by the various phases without resorting to jump conditions. In this scenario, the various phases are modeled as one fluid with variable material properties that change abruptly at the phase boundary. Adding singular terms (δ-function) to the equation is critical to account for these abrupt changes. This form of the equation

is often called the one-fluid approach and is the basis for describing the governing equations in this thesis.

This chapter describes the governing equations and the various numerical methods applied to solve those equations. In this thesis, we use two different solvers to study the problems. The numerical scheme for both solvers has been explained in detail. First, the in-house developed coupled level-set and volume-of-fluid method (CLSVOF) based solver is explained (§ 2.1). Then we outline details of the open-source solver Basilisk, which is based on a volume-of-fluid method (VOF) (§ 2.2). Finally, a summary is provided (§ 2.3).

2.1 CLSVOF method

The VOF method of Hirt and Nichols (1981) forms the building block of computations involving two fluids separated by a sharp interface. This approach uses a fixed grid wherein the interface is approximated within each two-fluid cell through which it passes. A preliminary approach was to represent the interface by a piecewise constant line (vertical or horizontal) known as Simple Line Interface Calculation. Youngs (1982) improved this interface representation and introduced the Piecewise Linear Interface Calculation. This method was robust and efficient but was only first-order accurate. Subsequently, Puckett et al. (1997) improved the interface representation method by introducing the Least-square Volume Interface Reconstruction Algorithm. The VOF method finds its advantage in satisfying mass conservation extremely well. However, it becomes difficult to accurately capture the geometric properties due to spatial discontinuity near the interface. An efficient interface representation method, known as the level-set (LS) method, was introduced by Sussman et al. (1994). This method was first developed and used in the context of computer graphics and image processing (Osher and Sethian, 1988). The level-set method is capable of accurately computing the geometric properties of complicated boundaries. If not properly implemented, this method may violate mass conservation. In the CLSVOF method of Sussman and Puckett (2000), the LS function is used only to compute the geometric properties of the interface, while the interface itself is advected using the VOF approach. Gerlach et al. (2006) compared different methods and concluded that the CLSVOF method was more efficient for surface tension dominated two-phase flows. The CLSVOF methodology adopted for the present thesis is described in detail in the following sections.

2.1.1 Governing equations

The mass and momentum conservation equations for the incompressible Newtonian two-phase flow system are expressed by the one-fluid formulation as (Prosperetti and Tryggvason, 2007)

$$\boldsymbol{\nabla} \cdot \mathbf{u} = 0 \,, \tag{2.1}$$

$$\rho \left[\frac{\partial \mathbf{u}}{\partial t} + \boldsymbol{\nabla} \cdot (\mathbf{u}\mathbf{u}) \right] = -\boldsymbol{\nabla} p + \boldsymbol{\nabla} \cdot (2\mu \mathbb{D}) + \rho \mathbf{g} + \mathbf{F}_s \,. \tag{2.2}$$

where $\mathbf{u} = (u, v)$ is the velocity field, p is the pressure, $\mathbb{D} = \frac{1}{2}\left[(\boldsymbol{\nabla}\mathbf{u}) + (\boldsymbol{\nabla}\mathbf{u})^T\right]$ is the deformation tensor, $\mathbf{g}$ is the acceleration due to gravity, and ρ and μ are the density and viscosity, respectively.

The surface tension term ($\mathbf{F}_s$) in the momentum conservation equation is defined by the continuum surface force (CSF) model of Brackbill et al. (1992). Using this model, the surface tension force per unit volume can be defined as

$$\mathbf{F}_s = \gamma \kappa \delta_s \hat{\mathbf{n}} \tag{2.3}$$

where γ is the surface tension coefficient, κ is the mean curvature of the interface, and $\hat{\mathbf{n}}$ is the unit normal vector to the interface. δ_s is the Dirac delta function which is zero everywhere except at the interface. The interface normal vector is computed from the Heaviside function (defined later) as $\hat{\mathbf{n}} = \boldsymbol{\nabla}\phi / |\boldsymbol{\nabla}\phi|$ (with ϕ being the level-set function) and the curvature is computed as $\kappa = -\boldsymbol{\nabla} \cdot \hat{\mathbf{n}}$. All the computations are performed under isothermal conditions and the concentration gradient along the interface is neglected.

2.1.2 Interface construction

In the present solver, the interface is constructed using the piecewise method as described by Youngs (1982). This method approximates the interface by a straight line in each cell. The alignment of the interface in each cell is calculated using the interface unit normal $\hat{\mathbf{n}}$. The initial value of $\hat{\mathbf{n}}$ in a two-phase cell (i, j) is calculated based on the volume fraction $C_{i,j}$ in that cell and the volume fraction of its neighbor cells. The initial value of the normal $\mathbf{n} = (n^x, n^y)$ is calculated in a cell as

$$n^x_{i,j} = \frac{1}{8\Delta x} \left(C_{i+1,j+1} + 2C_{i+1,j} + C_{i+1,j-1} - C_{i-1,j+1} - 2C_{i-1,j} - C_{i-1,j-1} \right) \,, \tag{2.4}$$

$$n_{i,j}^{y} = \frac{1}{8\Delta y}\left(C_{i+1,j+1} + 2C_{i,j+1} + C_{i-1,j-1} - C_{i+1,j-1} - 2C_{i,j-1} - C_{i-1,j-1}\right) . \quad (2.5)$$

The unit normal vector $\hat{\mathbf{n}}$ can then be calculated using $\hat{\mathbf{n}} = \mathbf{n}/|\mathbf{n}|$. The position of the interface is then adjusted so that it divides the cell into two areas to match the volume fraction. This is achieved by calculating the distance of the interface from the cell center.

A physical interface with zero thickness and a sharp jump in properties can lead to numerical convergence issues. To avoid this material discontinuity, a finite thickness of the interface is considered while capturing it numerically. The properties are smoothed in a thin region near the interface. In the CLSVOF approach, this smoothening is performed using a smoothed Heaviside function which is defined based on the level-set function as

$$H(\phi) = \begin{cases} 0 & \text{if } \phi < -\epsilon \, , \\ \frac{1}{2} + \frac{\phi}{2\epsilon} + \frac{1}{2\pi}\left[\sin\left(\frac{\pi\phi}{\epsilon}\right)\right] & \text{if } |\phi| \leq \epsilon \, , \\ 1 & \text{if } \phi > +\epsilon \, , \end{cases} \quad (2.6)$$

where ϵ is the numerical thickness of the interface on each side, leading to a total numerical thickness of 2ϵ. The code has been tested rigorously for different conditions to optimize this parameter (Ray et al., 2010; Tomar et al., 2007). In our simulations, we have considered the numerical interface thickness in the range $0.5\Delta x - 1.5\Delta x$, where Δx is the size of each grid cell. The physical properties are interpolated on this thin region as

$$\begin{aligned} \rho(\phi) &= \rho_1 H(\phi) + \rho_2(1 - H(\phi)) \, , \\ \mu(\phi) &= \mu_1 H(\phi) + \mu_2(1 - H(\phi)) \, . \end{aligned} \quad (2.7)$$

2.1.3 Interface advection

Let us define two immiscible fluids, fluid 1 and fluid 2, separated by an interface. Figure 2.1(a) shows an illustrative representation of the volume fraction. An indicator function $C_{i,j}$ is defined to identify the two fluids as

$$C_{i,j} = \frac{\Theta - \Theta_2}{\Theta_1 - \Theta_2} \quad (2.8)$$

where Θ denotes any property in a given cell. In the context of VOF, this indicator function is known as volume fraction which is defined in each cell (i, j) as

$$C_{i,j} = \begin{cases} 1 & \text{if it is a fluid 1 cell ,} \\ 0 & \text{if it is a fluid 2 cell ,} \\ 0 < C < 1 & \text{if it is a two-phase cell .} \end{cases} \tag{2.9}$$

The motion of the interface is captured by solving the advection equation for the volume fraction given as

$$\frac{\partial C}{\partial t} + \mathbf{u} \cdot \boldsymbol{\nabla} C = 0 \tag{2.10}$$

which can be reformulated as $\frac{\partial C}{\partial t} + \boldsymbol{\nabla} \cdot (\mathbf{u}C) = C\boldsymbol{\nabla} \cdot \mathbf{u}$ (by invoking the continuity equation). This equation is split into two equations in the two orthogonal directions as

$$\frac{\partial C}{\partial t} + \frac{\partial (uC)}{\partial x} = C\frac{\partial u}{\partial x} , \tag{2.11}$$

$$\frac{\partial C}{\partial t} + \frac{\partial (vC)}{\partial y} = C\frac{\partial v}{\partial y} . \tag{2.12}$$

This is known as the operator split approach. Puckett et al. (1997) suggested employing an implicit scheme in the first sweeping direction and an explicit scheme in the second direction to maintain the conservation property. Thus the equations are discretized as

$$C^*_{i,j} = C^n_{i,j} + \frac{\Delta t}{\Delta x}\left(\delta G^x_{i-1/2,j} - \delta G^x_{i+1/2,j}\right) + \frac{\Delta t}{\Delta x} C^*_{i,j}\left(u_{i+1/2,j} - u_{i-1/2,j}\right) , \tag{2.13}$$

$$C^{n+1}_{i,j} = C^*_{i,j} + \frac{\Delta t}{\Delta y}\left(\delta G^y_{i,j-1/2} - \delta G^y_{i,j+1/2}\right) + \frac{\Delta t}{\Delta y} C^*_{i,j}\left(v_{i,j+1/2} - v_{i,j-1/2}\right) , \tag{2.14}$$

where $\delta G^x_{i+1/2,j} = (uC)_{i+1/2,j}$ indicates the flux across the right face of (i, j) cell and $\delta G^y_{i,j+1/2} = (vC)_{i,j+1/2}$ indicates the flux across the top edge of the (i, j) cell. The superscripts n and $n + 1$ denote the time instances at the current and next iteration levels, respectively, with Δt denoting the time step. The star term $(C^*_{i,j})$ represents the intermediate values after the sweep in the first direction. The volume flux δG can be obtained using a geometrical interpretation of flux as shown in Figure 2.1(a). Considering the right face of a cell containing the interface, the portion advecting during time Δt can be calculated as $u_{i+1/2,j}\Delta t\Delta y$ (fluxed into the neighboring cell). The fluxed volume from this face to the neighboring cell can be calculated using the

known interface position and the velocity as

$$\delta G^x_{i+1/2,j} = \frac{u_{i+1/2,j} G^x_{i+1/2,j}}{u_{i+1/2,j} \Delta t \Delta y} = \frac{G^x_{i+1/2,j}}{\Delta t \Delta y} \tag{2.15}$$

This value of volume flux is substituted in Equation (2.13) and the intermediate volume fraction $C^*_{i,j}$ is calculated. In a similar manner, the vertical flux $G^y_{i,j+1/2}$ is determined, and subsequently the volume fraction at new time level $C^{n+1}_{i,j}$ is calculated. The methodology is made second-order accurate by alternating the sweep direction at each time step, known as Strang splitting (Strang, 1968).

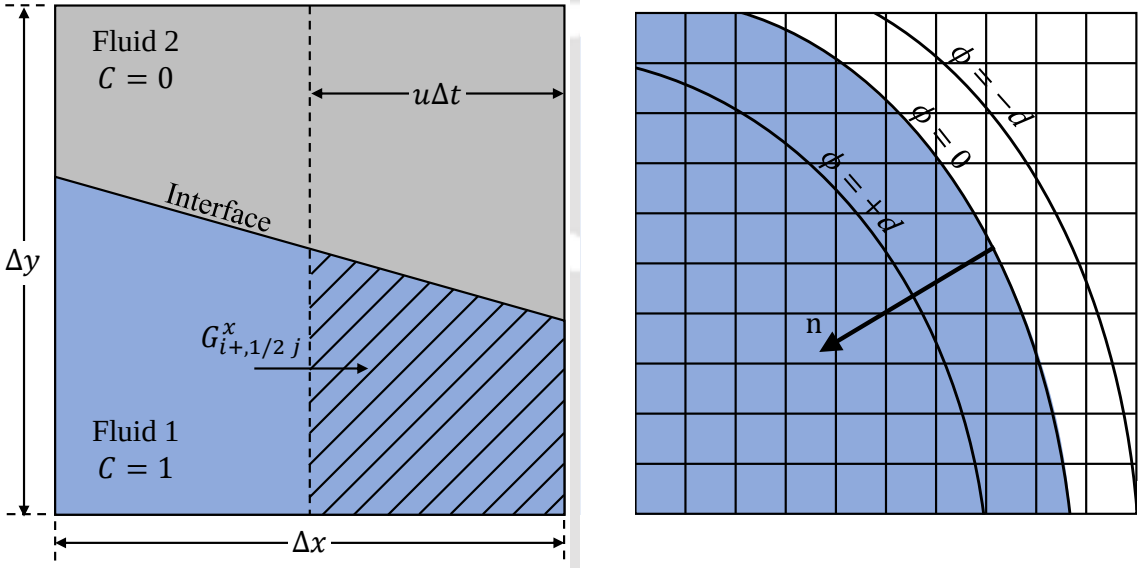

Fig. 2.1 A representative diagram showing (a) volume fraction advection into the neighboring cell on the right, and (b) distribution of level-set function around the interface.

The level-set function is used to calculate the geometric properties only. The interface is represented using a smooth level-set function ϕ which is maintained as a signed distance from the interface given as

$$\phi(\mathbf{r}, t) = \begin{cases} +d & \text{in the fluid 1 region ,} \\ 0 & \text{at the interface ,} \\ -d & \text{in the fluid 2 region ,} \end{cases} \tag{2.16}$$

where $d = d(\mathbf{r})$ is the shortest distance of the interface from the point having position vector $\mathbf{r}$. Figure 2.1(b) shows an illustrative representation of the distribution of ϕ around the interface. Using the initial know position of the interface, the advection equation for the level-set function is solved to capture the interface at next the time step, which is given as

$$\frac{\partial \phi}{\partial t} + \mathbf{u} \cdot \boldsymbol{\nabla} \phi = 0 \tag{2.17}$$

The convective term is discretized using the essentially non-oscillatory (ENO) scheme (Chang et al., 1996). After each time step, the level set function is reinitialized to the exact signed normal distance by coupling it with the volume fraction.

In the above discussion, we defined the two phases using a volume fraction method. After determining the interface, we solved the advection equation to drive the interface. The level-set function was invoked to calculate the geometric properties. The CLSVOF method combines the advantage of both the level-set and volume-of-fluid approaches. Now we present the interface advection algorithm adopted in the present CLSVOF method.

1. Intermediate volume fraction $C^*_{i,j}$ is calculated in one sweep direction by solving Equation (2.13).

2. Level-set function ϕ is advected in the same direction by solving the split form of Equation (2.17).

3. Interface normal and curvature are calculated, and the perpendicular distance between cell center and interface is adjusted to match the given volume fraction with that of the reconstructed interface.

4. Next sweep is performed by solving Equation (2.14) to get the final distribution of the volume fraction $C^{n+1}_{i,j}$.

5. Intemediate level-set function is advected in the above sweep direction by solving the split form of Equation (2.17).

6. Interface is again reconstructed based on updated values of volume fraction and level-set function as described in step 3.

7. The scheme for advancing ϕ using Equation (2.17) (steps 2 and 5) does not conserve its distance function attributes. Hence, the level-set function is reinitialized after each time.

2.1.4 Numerical scheme

The single set of governing equations is solved on a staggered grid arrangement by using the marker-and-cell (MAC) algorithm of Harlow and Welch (1965). A uniform grid arrangement is used where the grid size in both directions is considered the same, i.e., $\Delta x = \Delta y$. All the scalar variables are defined at the cell centers, while the vector quantities are defined at the face centers. The surface tension force is modeled using the CSF model as described in Equation (2.3). The fluid properties are calculated based on a smoothed Heaviside function for the treatment of discontinuity across the interface as formulated in Equation (2.7). The momentum equation is re-written as

$$\rho(\phi)\left[\frac{\partial \mathbf{u}}{\partial t} + \boldsymbol{\nabla}\cdot(\mathbf{u}\mathbf{u})\right] = -\boldsymbol{\nabla}p + \boldsymbol{\nabla}\cdot(2\mu(\phi)\mathbb{D}) + \rho(\phi)\mathbf{g} + \gamma\kappa(\phi)\mathbf{n}(\phi) \tag{2.18}$$

The discretized momentum equation is given as

$$\begin{aligned}\mathbf{u}^{n+1} = \mathbf{u}^{n} &- (\boldsymbol{\nabla}\cdot(\mathbf{u}^{n}\mathbf{u}^{n})\Delta t + \mathbf{g}\Delta t \\ &+ \left(\frac{-\boldsymbol{\nabla}p^{n+1} + \boldsymbol{\nabla}\cdot(2\mu(\phi^{n})\mathbb{D}_{u}^{n}) + \sigma\kappa(\phi^{n})\mathbf{n}(\phi^{n})}{\rho(\phi^{n})}\right)\Delta t\end{aligned} \tag{2.19}$$

The convective terms in the momentum equation are discretised using a second order ENO scheme, and the remaining space derivatives are discretised using a central difference scheme. The discretised momentum equations are solved explicitly for known values of volume fraction and level-set function at time t^n resulting in a provisionally predicted velocity field $\mathbf{u}^*$. This predicted velocity is corrected by invoking the continuity equation (divergence-free velocity field). This leads to the pressure Poisson equation given by

$$\boldsymbol{\nabla}\cdot\mathbf{u}^{n+1} - \boldsymbol{\nabla}\cdot\mathbf{u}^{*} = -\Delta t\boldsymbol{\nabla}\cdot\left(\frac{\boldsymbol{\nabla}p'}{\rho(\phi^{n})}\right) \tag{2.20}$$

where $p' = p^{n+1} - p^{n}$ is the pressure correction term. This equation is solved using an iterative method based on preconditioned biconjugate gradient (BI-CGSTAB) method. Using the pressure correction, the provisional velocities are corrected to obtain the velocity at the new time level t^{n+1} using

$$\mathbf{u}^{n+1} = \mathbf{u}^{*} - \Delta t\left(\frac{\boldsymbol{\nabla}p'}{\rho(\phi^{n})}\right) \tag{2.21}$$

This updated velocity field is utilized to determine the new volume fraction C^{n+1} and level-set function ϕ^{n+1} followed by the interface reconstruction.

The above-detailed discretization leads to a scheme that is second-order accurate in space and first-order accurate in time. The explicit treatment of convective terms leads to time constraints to ensure stability of the solution. In the advection algorithm, the sum of the volume fluxed over the cell faces must be smaller than the total cell volume. This leads to the limiting condition

$$\Delta t_c \leq \left(\frac{\Delta x}{|u|_{max}} + \frac{\Delta y}{|v|_{max}} \right) \tag{2.22}$$

Furthermore, the explicit treatment of surface tension term also results in a capillary time step limit as

$$\Delta t_s < \left[\frac{\gamma \pi}{\Delta x (\rho_1 + \rho_2)} \right]^{1/2} \tag{2.23}$$

Finally, the stability restriction due to gravity can be expressed as

$$\Delta t_g \leq \frac{\Delta x}{v_g} \tag{2.24}$$

where $v_g = \mathbf{g}\Delta t_g$ is the gravity-induced velocity. Among all the time limits $(\Delta t_c, \Delta t_s, \Delta t_g)$, the minimum value is used as the time step for all the computations.

2.2 BASILISK solver

In this section, we describe the open-source solver Basilisk used to study the two-phase electrohydrodynamic (EHD) problems (Popinet, 2003, 2009, 2015). We detail both the Newtonian and viscoelastic formulations employed in the solver. The solver is based on the finite-volume approach and deals with the interface tracking using a VOF methodology in solving incompressible two-phase fluid motions. One advantage of this solver is the utilization of an adaptive quad/octree spatial discretization which significantly reduces the computational cost. The continuum surface force method (CSF) is applied in a balanced way to simulate surface-tension-driven flows accurately. The solver incorporates the electric body forces into the Navier-Stokes equation and considers the charge migration due to both conduction and convection (López-Herrera et al., 2011). The additional stress term arising from viscoelastic studies is also integrated into the Navier-Stokes equation (López-Herrera et al., 2019). The solver

provides two approaches for viscoelastic simulation: the log conformation approach and the square-root conformation approach. We restrict ourselves to the log conformation approach and the Oldroyd-B constitutive model in this thesis. The log conformation approach is combined with the time-split scheme to increase the stability of viscoelastic flow simulations.

The simulation of two-phase flows by incorporating the electrostatic effects is quite challenging. Most studies prefer the Boundary Element Method for simulating such multiphysics problems (Lac and Homsy, 2007; Sherwood, 1988). However, this method is restricted to solving problems in the limit of Stokes flows. Some previous studies have used the Finite Element Method to study the breakup of charged jets and droplet formation in electric fields (Collins et al., 2013; Notz and Basaran, 1999). This solver has been used previously in investigating different EHD flow phenomena (Behera et al., 2019; Borthakur et al., 2021; Ghasemi et al., 2018). Viscoelastic flows have been modeled using the Finite Element Method (Hulsen et al., 2005; Kane et al., 2009; Knechtges et al., 2014). The log conformation approach was implemented in these studies. Other numerical methods, such as the Lattice Boltzmann Method (Ma et al., 2020; Phillips and Roberts, 2011) and Smoothed Particle Hydrodynamics (Xu et al., 2012; Zainali et al., 2013), can also be found in the literature on computational rheology. Various flow dynamics and different rheological effects have been successfully studied in the past using the present solver (Azarmanesh et al., 2015; Li and Cheng, 2023; Romanò et al., 2021). The numerical methodology used in the solver is described in detail in the following sections.

2.2.1 Governing equations

The continuity and momentum equations governing the incompressible Newtonian and viscoelastic two-phase flow system are expressed by the one-fluid formulation as

$$\boldsymbol{\nabla} \cdot \mathbf{u} = 0 \,, \tag{2.25}$$

$$\rho \left[\frac{\partial \mathbf{u}}{\partial t} + \mathbf{u} \cdot \boldsymbol{\nabla} \mathbf{u} \right] = -\boldsymbol{\nabla} p + \boldsymbol{\nabla} \cdot \mathbb{T} + \mathbf{F}_s + \mathbf{F}_e \,, \tag{2.26}$$

where $\mathbf{u} = (u, v)$ is the velocity field, p is the pressure, and ρ and μ are the fluid density and viscosity, respectively. The surface tension term $\mathbf{F}_s$ in the momentum equation is

defined by the CSF model of Brackbill et al. (1992) as

$$\mathbf{F}_s = \gamma\kappa\delta_s\hat{\mathbf{n}} \,, \tag{2.27}$$

where γ is the surface tension coefficient, κ is the interface curvature, and $\hat{\mathbf{n}}$ is the unit normal to the interface. δ_s is the Dirac delta function which is zero everywhere except at the interface.

The stress tensor ($\mathbb{T}$) in the momentum equation is split into the solvent component ($\mathbb{T}_s$) and the polymeric component ($\mathbb{T}_p$) as

$$\boldsymbol{\nabla}\cdot\mathbb{T} = \boldsymbol{\nabla}\cdot\mathbb{T}_s + \boldsymbol{\nabla}\cdot\mathbb{T}_p \tag{2.28}$$

The solvent component (viscous stress tensor) is expressed as the usual Newtonian fluid as $\mathbb{T}_s = 2\mu_s\mathbb{D} = \mu_s\left(\boldsymbol{\nabla}\mathbf{u} + \boldsymbol{\nabla}\mathbf{u}^T\right)$ where μ_s is the solvent viscosity. In the Newtonian studies, there is no contribution from polymeric part ($\mathbb{T}_p = 0$) and the solvent viscosity is considered as the fluid viscosity ($\mu_s = \mu$). The polymeric component of the stress tensor considers the memory effects exhibited by the polymer. There are several constitutive rheological models available in the literature to define the polymeric stresses (Renardy, 1989). These are typically functions of the conformation tensor $\mathbf{A}$

$$\mathbb{T}_p = \frac{\mu_p\mathbf{f_S}(\mathbf{A})}{\lambda} \,, \tag{2.29}$$

where $\mathbf{f_S}(\cdot)$ is the strain function, λ is the relaxation parameter of the fluid, and μ_p is the polymeric viscosity (Grmela and Carreau, 1987). The conformation tensor describes the local average of stretch and orientation of polymer molecules within the polymer solution. This is assumed to be always symmetric and positive definite, obeying $\overset{\triangledown}{\mathbf{A}} = -\mathbf{f_R}(\mathbf{A})/\lambda$ where $\mathbf{f_R}(\cdot)$ is the relaxation function, and $\overset{\triangledown}{\mathbf{A}}$ denotes the operator upper-convected derivative defined as

$$\overset{\triangledown}{\mathbf{A}} = \frac{\partial\mathbf{A}}{\partial t} + \mathbf{u}\cdot\boldsymbol{\nabla}\mathbf{A} - \mathbf{A}\cdot(\boldsymbol{\nabla}\mathbf{u}) - (\boldsymbol{\nabla}\mathbf{u})^T\cdot\mathbf{A} \tag{2.30}$$

We perform the viscoelastic studies for an Oldroyd-B model whose constitutive relation reduces to $\lambda\overset{\triangledown}{\mathbb{T}}_p + \mathbb{T}_p = 2\mu_p\mathbb{D}$ that can be expressed as

$$\lambda\left[\frac{\partial\mathbb{T}_p}{\partial t} + \mathbf{u}\cdot\boldsymbol{\nabla}\mathbb{T}_p - (\boldsymbol{\nabla}\mathbf{u})\cdot\mathbb{T}_p - \mathbb{T}_p\cdot(\boldsymbol{\nabla}\mathbf{u})^T\right] + \mathbb{T}_p = \mu_p\left(\boldsymbol{\nabla}\mathbf{u} + \boldsymbol{\nabla}\mathbf{u}^T\right) \tag{2.31}$$

Maxwell's electromagnetic equations are considered while computing $\mathbf{F}_e$ (Melcher and Taylor, 1969; Saville, 1997). Since the characteristic time scale for the magnetic induction effects is significantly smaller than the characteristic time scale for electric phenomena in this study, we ignore the electromagnetic coupling and assume that the electric field, $\mathbf{E}$, is curl-free ($\boldsymbol{\nabla} \times \mathbf{E} = 0$). Thus, we can write $\mathbf{E} = -\boldsymbol{\nabla}\varphi$ where φ is the electric potential. In this electrostatic limit, we have the following Poisson equation

$$\boldsymbol{\nabla} \cdot (\varepsilon \mathbf{E}) = \boldsymbol{\nabla} \cdot (\varepsilon \boldsymbol{\nabla}\varphi) = -q_v \ , \tag{2.32}$$

where ε is the electric permittivity and q_v is the volumetric charge density. The charge conservation equation is given by

$$\frac{\partial q_v}{\partial t} + \boldsymbol{\nabla} \cdot \mathbf{J} = 0 \tag{2.33}$$

Here, $\mathbf{J} = \sigma \mathbf{E} + q_v \mathbf{u}$ is the current density (ohmic charge conduction + convection of charges) with σ denoting the electric conductivity. Considering homogeneous electrical properties, Equation (2.33) reduces to

$$\frac{\partial q_v}{\partial t} + \boldsymbol{\nabla} \cdot (q_v \mathbf{u}) = \boldsymbol{\nabla} \cdot (\sigma \boldsymbol{\nabla}\varphi) \tag{2.34}$$

The electric field force can be modeled as a volumetric force given by

$$\mathbf{F}_e = q_v \mathbf{E} - \frac{1}{2} E^2 \boldsymbol{\nabla}\varepsilon \tag{2.35}$$

The first term in the above equation is the electrophoretic force arising due to the presence of free charges and the second term is the dielectrophoretic force. The electric force can also be written in terms of the divergence of the Maxwell stress tensor $\mathbb{T}_e$ as $\mathbf{F}_e = \boldsymbol{\nabla} \cdot \mathbb{T}_e$ where

$$\mathbb{T}_e = \varepsilon \left(\mathbf{E}\mathbf{E} - \frac{E^2}{2} \mathbf{I} \right) \tag{2.36}$$

The above one-fluid formulation can be shown to impose the following boundary conditions implicitly. The electric potential is continuous through the interface such that $\|\phi\| = 0$ where $\|\cdot\|$ indicates the jump in the quantity across the interface in the direction of the normal vector $\mathbf{n}$. Since no phase change is involved, we have velocity continuity at the interface as $\|\mathbf{u} \cdot \mathbf{n}\| = 0$. Using Gauss Law at the interface yields the jump condition in the normal ($E_n = \mathbf{E} \cdot \mathbf{n}$) and tangential ($E_t = \mathbf{E} \cdot \mathbf{t}$) component of

the electric field

$$\|\varepsilon E_n\| = q_s \ , \qquad \|E_t\| = 0 \ , \tag{2.37}$$

where q_s is the surface charge density of free charges. Normal stress balance condition at the interface yields

$$\|p\| + \mathbf{n} \cdot \|\mathbb{T}\| \cdot \mathbf{n} + \mathbf{n} \cdot \|\mathbb{T}_e\| \cdot \mathbf{n} = \gamma\kappa \ , \tag{2.38}$$

where $\|p\|$ denotes the jump in pressure, $\mathbf{n} \cdot \|\mathbb{T}\| \cdot \mathbf{n}$ is the jump in the normal component of the viscous stress, and $\mathbf{n} \cdot \|\mathbb{T}_e\| \cdot \mathbf{n}$ is the jump in the normal component of the Maxwell stress tensor across the drop surface. In the absence of any variation in the surface tension coefficient, tangential stress balance is given by

$$\mathbf{t} \cdot \|\mathbb{T}\| \cdot \mathbf{n} + \mathbf{t} \cdot \|\mathbb{T}_e\| \cdot \mathbf{n} = 0 \tag{2.39}$$

Conservation of the surface charge is ensured by accounting for advection of the interface, along with the change in area of the interface due to motion. Thus, surface charge conservation equation is given by

$$\frac{\partial q_s}{\partial t} + \mathbf{u} \cdot \boldsymbol{\nabla}_s q_s - q_s \mathbf{n} \cdot (\mathbf{n} \cdot \boldsymbol{\nabla}) \cdot \mathbf{u} + \|\sigma E_n\| = 0 \ , \tag{2.40}$$

where the term, $q_s \mathbf{n} \cdot (\mathbf{n} \cdot \boldsymbol{\nabla}) \cdot \mathbf{u}$, accounts for the change in charge density due to the change in the interfacial area. Variation in surface charge density due to the difference in the current density across the interface is given by the last term. In the one-fluid formulation, we solve a volumetric charge conservation equation which also accounts for the surface charge conservation in a thin diffused layer (over one to three grid cells) at the interface. The efficacy of the one-fluid formulation has been demonstrated in Tomar et al. (2007) and López-Herrera et al. (2011). The algorithm used in this study is from the latter study which employs a charge conservation approach.

2.2.2 Numerical scheme

The interface is tracked using the VOF method in which the volume fraction C is advected with the fluid using

$$\frac{\partial C}{\partial t} + \boldsymbol{\nabla} \cdot (\mathbf{u} C) = 0 \tag{2.41}$$

The two immiscible fluids, fluid 1 and fluid 2, separated by an interface, are tracked by solving this equation. This advection equation is solved using a one-dimensional scheme wherein the volume fraction C is advected along each spatial direction (x and y). The flux along the sweeping direction is computed from the local interface normal and the face velocities. This flux is further corrected utilizing the divergence-free condition of the velocity field. The sweeps are performed in alternate directions to avoid a preferred direction of advection. The spatial values of the fluid and electric properties are interpolated using the weighted arithmetic mean as

$$\begin{aligned} \rho &= C\rho_1 + (1-C)\rho_2 \,, \qquad \mu = C\mu_1 + (1-C)\mu_2 \,, \\ \varepsilon &= C\varepsilon_1 + (1-C)\varepsilon_2 \,, \qquad \sigma = C\sigma_1 + (1-C)\sigma_2 \,. \end{aligned} \tag{2.42}$$

The surface tension force is included in the momentum equation following the CSF method in a balanced manner which avoids parasitic currents (Francois et al., 2006). The curvature of the interface is computed accurately using a height function approach (Popinet, 2018). The curvature κ is calculated as

$$\kappa = \frac{h_y''}{\sqrt{1+h_y'^2}} \tag{2.43}$$

using the height functions as $x = h_x(y)$ and $y = h_y(x)$. This method results in a second-order accurate estimation of curvature.

The solver uses a staggered-in-time discretization combined with a time-splitting projection method, resulting in a second-order accurate scheme. The polymeric stresses and electric field equations are discretized accordingly (López-Herrera et al., 2019, 2011). The time-stepping scheme of the Navier-Stokes equations is as follows:

Step 1: Volume fraction at the intermediate time step $C_{n+\frac{1}{2}}$ are calculated using a VOF scheme.

$$\frac{C_{n+\frac{1}{2}} - C_{n-\frac{1}{2}}}{\Delta t} + \boldsymbol{\nabla} \cdot (\mathbf{u}_n C_n) = 0 \tag{2.44}$$

Step 2: Properties are updated

$$\Theta_{n+\frac{1}{2}} = \Theta_1 C_{n+\frac{1}{2}} + \Theta_2 (1 - C_{n+\frac{1}{2}}) \tag{2.45}$$

where Θ is any property of the fluid: ρ, $\mu_s(\mu)$, μ_p, σ, ε.

Step 3: Polymeric stresses are computed at the intermediate time step, $(\mathbb{T}_p)_{n+\frac{1}{2}}$. The time-stepping scheme for this will be discussed later.

Step 4: Charge density at the intermediate time step $(q_v)_{n+\frac{1}{2}}$ is calculated. The convective term is approximated using the Bell-Colella-Glaz (BCG) scheme (second-order unsplit upwind scheme) (Bell et al., 1989).

$$\frac{(q_v)_{n+\frac{1}{2}} - (q_v)_{n-\frac{1}{2}}}{\Delta t} + \boldsymbol{\nabla} \cdot \left[(q_v)_n \mathbf{u}_n + \sigma_{n-\frac{1}{2}} \mathbf{E}_{n-\frac{1}{2}}\right] = 0 \tag{2.46}$$

Step 5: Electric potential at the intermediate time step $\phi_{n+\frac{1}{2}}$ is calculated by solving the Poisson equation for electric potential. Electric field is computed as $\mathbf{E}_{n+\frac{1}{2}} = -\boldsymbol{\nabla}\phi_{n+\frac{1}{2}}$.

$$\boldsymbol{\nabla} \cdot \left[\boldsymbol{\nabla}\left(\varepsilon_{n+\frac{1}{2}} \varphi_{n+\frac{1}{2}}\right)\right] = -(q_v)_{n+\frac{1}{2}} \tag{2.47}$$

Step 6: Electric body force $(\mathbf{F}_e)_{n+\frac{1}{2}}$ is computed from $\mathbf{E}_{n+\frac{1}{2}}$ using a conservative approach by utilizing the cell face values (López-Herrera et al., 2011).

$$(\mathbf{F}_e)_{n+\frac{1}{2}} = \boldsymbol{\nabla} \cdot (\mathbb{T}_e)_{n+\frac{1}{2}} = \varepsilon_{n+\frac{1}{2}} \left(\mathbf{E}_{n+\frac{1}{2}} E_{n+\frac{1}{2}} - \frac{(E^2)_{n+\frac{1}{2}}}{2}\mathbf{n}\right) \tag{2.48}$$

Step 7: Provisional velocity field $\mathbf{u}_*$ is calculated, where the advection term is computed using the BCG scheme.

$$\rho_{n+\frac{1}{2}} \left(\frac{\mathbf{u}_* - \mathbf{u}_n}{\Delta t} + \mathbf{u}_{n+\frac{1}{2}} \cdot \boldsymbol{\nabla}\mathbf{u}_{n+\frac{1}{2}}\right) = \boldsymbol{\nabla} \cdot \left(\mu_{n+\frac{1}{2}}(\mathbb{D}_n + \mathbb{D}_*)\right) + \boldsymbol{\nabla} \cdot (\mathbb{T}_p)_{n+\frac{1}{2}} + (\gamma\kappa\delta_s\mathbf{n})_{n+\frac{1}{2}} + (\mathbf{F}_e)_{n+\frac{1}{2}} \tag{2.49}$$

Step 8: Pressure at the intermediate time step is calculated by solving the pressure Poisson equation.

$$\boldsymbol{\nabla} \cdot \left(\frac{\Delta t}{\rho_{n+\frac{1}{2}}} \boldsymbol{\nabla} p_{n+\frac{1}{2}}\right) = \boldsymbol{\nabla} \cdot \mathbf{u}_* \tag{2.50}$$

Step 9: Velocity field $\mathbf{u}_{n+1}$ is calculated, which is used to advect the volume fraction for the next time step.

$$\mathbf{u}_{n+1} = \mathbf{u}_* - \frac{\Delta t}{\rho_{n+\frac{1}{2}}} \boldsymbol{\nabla} p_{n+\frac{1}{2}} \tag{2.51}$$

Next, we describe the time stepping for computing the polymeric stresses using the log conformation approach (Fattal and Kupferman, 2004), as mentioned in Step 3. A time-split procedure is applied to decompose $\boldsymbol{\Psi}$ (Hao and Pan, 2007) (for details of log conformation tensor see Appendix A)

$$\frac{\partial \boldsymbol{\Psi}}{\partial t} + \mathbf{u} \cdot \boldsymbol{\nabla} \boldsymbol{\Psi} - 2\mathbf{B} - (\boldsymbol{\Omega}\boldsymbol{\Psi} - \boldsymbol{\Psi}\boldsymbol{\Omega}) = -\frac{e^{-\boldsymbol{\Psi}}}{\lambda} \mathbf{f}_{\mathbf{R}}(e^{\boldsymbol{\Psi}}) \tag{2.52}$$

where $\Psi = \log(\mathbf{A})$ as

$$\frac{\partial \boldsymbol{\Psi}}{\partial t} + \mathbf{u} \cdot \boldsymbol{\nabla} \boldsymbol{\Psi} = 0 \,, \tag{2.53}$$

$$\frac{\partial \boldsymbol{\Psi}}{\partial t} - 2\mathbf{B} - (\boldsymbol{\Omega}\boldsymbol{\Psi} - \boldsymbol{\Psi}\boldsymbol{\Omega}) = 0 \,, \tag{2.54}$$

$$\frac{\partial \boldsymbol{\Psi}}{\partial t} = -\frac{e^{-\boldsymbol{\Psi}}}{\lambda} \mathbf{f}_{\mathbf{R}}(e^{\boldsymbol{\Psi}}) \,. \tag{2.55}$$

The stress function, $\mathbf{f}_{\mathbf{S}}(\mathbf{A})$, and the relaxation function, $\mathbf{f}_{\mathbf{R}}(\mathbf{A})$, are assumed as linear functions $\mathbf{f}_{\mathbf{S},\mathbf{R}}(\mathbf{A}) = \eta_{S,R}\,(\nu_{S,R}\mathbf{A} - \mathbf{I})$. For Oldroyd-B model $\eta_S = \eta_R = 1$ and $\nu_S = \nu_R = 1$, and therefore $\mathbf{f}_{\mathbf{S},\mathbf{R}}(\mathbf{A}) = (\mathbf{A} - \mathbf{I})$. Using the values of polymeric stress at $\left(n - \frac{1}{2}\right)$ and the velocity field at n, time stepping of Equation (2.52) is as follows:

Step 1: Conformation tensor at $\left(n - \frac{1}{2}\right)$ is calculated.

$$\mathbf{A}_{n-\frac{1}{2}} = \frac{\lambda}{\mu_p} (\mathbb{T}_p)_{n-\frac{1}{2}} + \mathbf{I} \tag{2.56}$$

Step 2: Conformation tensor is diagonalized to obtain its eigenvalues $\Lambda_{n-\frac{1}{2}}$ and eigenvectors matrix $\mathbf{R}_{n-\frac{1}{2}}$.

Step 3: Log of the conformation tensor is calculated.

$$\boldsymbol{\Psi}_{n-\frac{1}{2}} = \mathbf{R}\ \log(\Lambda)\ \mathbf{R}^T \Big|_{n-\frac{1}{2}} \tag{2.57}$$

Step 4: Values of $\mathbf{B}_n$ and $\mathbf{\Omega}_n$ are obtained using the eigenvalues and eigenvectors at $\left(n-\frac{1}{2}\right)$.

Step 5: Log conformation tensor is advected using the BCG scheme.

$$\mathbf{\Psi}_* = \mathbf{\Psi}_{n-\frac{1}{2}} - \Delta t \boldsymbol{\nabla} \cdot (\boldsymbol{u_n} \mathbf{\Psi}_n) \tag{2.58}$$

Step 6: Provisional values $\mathbf{\Psi}_{**}$ are calculated implicity.

$$\mathbf{\Psi}_{**} = \mathbf{\Psi}_* + \Delta t \left(2\mathbf{B}_n + \mathbf{\Omega}_n \mathbf{\Psi}_{n-\frac{1}{2}} - \mathbf{\Psi}_{n-\frac{1}{2}} \mathbf{\Omega}_n\right) \tag{2.59}$$

Step 7: Equation (2.55) is integrated to obtain Λ^{**}, $\mathbf{R}^{**}$ and the conformation tensor $\mathbf{A}^{**} = \mathbf{R}\ \Lambda\ \mathbf{R}^T\Big|_{**}$

Step 8: Conformation tensor at $\left(n+\frac{1}{2}\right)$ is calculated.

$$\mathbf{A}_{n+\frac{1}{2}} = \mathbf{A}_{**} e^{-\Delta t/\lambda} + \left(1 - e^{-\Delta t/\lambda}\right) \mathbf{I} \tag{2.60}$$

Step 9: Polymer stress at $\left(n+\frac{1}{2}\right)$ is calculated.

$$(\mathbb{T}_p)_{n+\frac{1}{2}} = \frac{\mu_p}{\lambda} \left(\mathbf{A}_{n+\frac{1}{2}} - \mathbf{I}\right) \tag{2.61}$$

This completely describes the numerical scheme the solver uses to numerically solve the Navier-Stokes equations, including the electric force and polymeric stress terms. The electric field is computed separately, and the resultant electric force is added to the momentum equation. Similarly, the polymeric stresses are computed separately using the log conformation approach and added to the momentum equation.

2.2.3 Spatial dicretization

Space is discretized using a structured grid of square finite volumes that can be uniform or non-uniform. The discretization is arranged hierarchically in a quadtree structure (Popinet, 2003). The size of a cell h is represented by its level l ($h \propto 2^{-l}$). All the variables are defined at the center of each cell in a collocated manner, with some exceptions where the variables are defined at the cell faces to avoid any spurious current. The variables are computed as the volume-averaged values for the corresponding cell. An approximate projection method is used for the spatial discretization to avoid

decoupling pressure and velocity fields. The quadtree grid structure can be refined and coarsened dynamically at a reasonable computational cost. This adaptation is based on a restriction criteria of desired scalar fields. Interpolation and extrapolation are performed to assign proper values for each variable in the refined and coarsened cells. A detailed description and visualization of the mesh size used in the present solver are shown in Appendix C.

2.3 Summary

In this chapter, the equations governing the Newtonian and viscoelastic flows and their numerical implementations are discussed. We primarily solve the two-phase incompressible fluid flow equations with some modifications due to the presence of polymers or the effect of an external electric field. The two solvers used for the studies in this thesis have been described extensively. The in-house solver based on the CLSVOF method will be utilized to study the dynamics of drop impacting a liquid pool. The EHD studies involving Newtonian and viscoelastic models will be performed using the open-source solver Basilisk.

Chapter 3

Evolution of jets during drop impact on a deep liquid pool

The transition regime between coalescence and splashing of drops due to impact on a liquid pool includes jet formation with single or multiple secondary drops. One of the main features of this regime is the formation of a central liquid jet followed by the breakup of the jet in the form of drops. This chapter investigates the formation of various secondary drops depending on the impact conditions using a coupled level-set and volume-of-fluid (CLSVOF) method. The chapter begins by describing the drop impact mechanism on a liquid pool and the previous studies conducted (§ 3.1). Next, the computational setup used for the study is outlined (§ 3.2). This is followed by validating the present model with previous experimental studies (§ 3.3). Then the validated model is used to study three different regimes (§ 3.4). The first is the formation of a long thick central jet with a smaller secondary drop. The second is the formation of a slender jet with multiple secondary drops. And the third is the formation of a long thick central jet with a larger secondary drop. The chapter then concludes with a summary of the results and establishes that secondary drops larger than the initial drop can be obtained at higher impact velocities (§ 3.5).

3.1 Introduction

Drop splashing on liquid layers is encountered frequently in nature. Splashing finds applications in many areas, such as oil spills, ink-jet printing, and spray cooling. Experimental, numerical, and theoretical studies of the phenomena of drop impact have been reported in Rein (1993). Depending on the impact conditions, water drops

falling on a deep pool can coalesce to form a vortex ring or splash. When a drop impacts a liquid surface with a sufficiently low velocity, it coalesces with the pool forming a vortex ring (Rein, 1993; Thoraval et al., 2016). As the impact velocity of the drop is increased, the splashing regimes start. The main features of splashing are the formation of a crown and the rise of a liquid column in the middle of the crater (Ray et al., 2015). Furthermore, the cavity produced in the pool is deep, and its retraction leads to a central jet. Instabilities usually cause the separation of droplets from the tip of this central jet. The transition between coalescence and splashing proceeds via several intermediate steps. A review of different stages of coalescence of liquid on a planar interface, with the significance of different types of stresses, was presented by Kavehpour (2015). For a higher Froude number and thus a higher Weber number, the long thick jet phenomena begins. This can be explained by the high inertia force, which produces high amplitude capillary waves traveling towards the crater base. During this stage, the crater base retracts differently for different parametric ranges leading to different phenomena as shown by, for example, Leng (2001) experimentally and Ray et al. (2015) numerically. By performing experiments on a water drop impacting a horizontal free water surface, Ma et al. (2019) showed that the size of the secondary drop could be even bigger than the primary drop. In the present investigation, particular emphasis is put on determining the conditions under which a secondary drop forms. For this purpose, the different regimes are investigated by detailed numerical simulations. A newly identified regime characterized by a long thick central jet with a secondary drop larger than the primary falling drop is studied. The present study attempts to enhance the understanding of the dynamics related to the secondary drop, especially for this specific case.

3.2 Formulation

3.2.1 Computational domain

The impact dynamics is investigated using the complete Navier-Stokes equations in an axisymmetric cylindrical coordinate system (r, z) with $z = 0$ representing the bottom of the domain, while $r = 0$ is the axis of symmetry. Gravity ($\mathbf{g}$) acts in the negative z direction. Figure 3.1 shows the schematic diagram for the initial configuration of the system. The drop and the liquid pool are denoted by 1, while the surrounding medium is denoted by 2. The fluids are assumed to be Newtonian and incompressible.

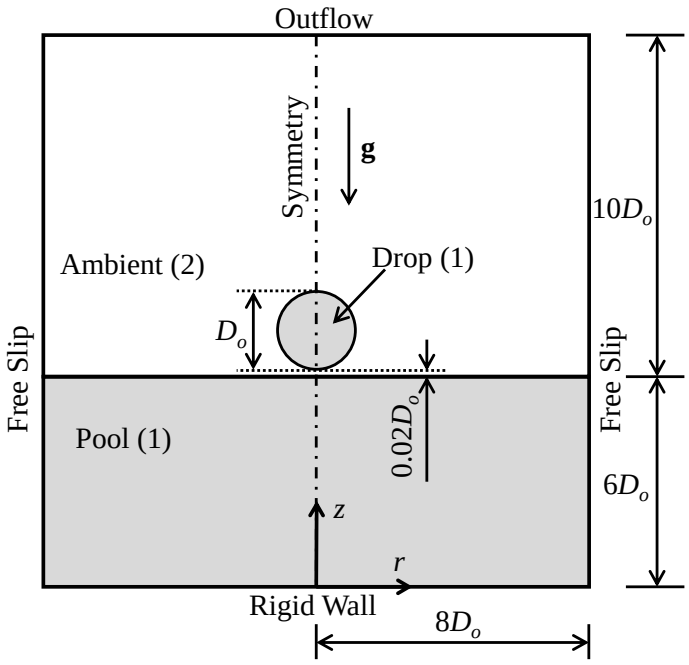

Fig. 3.1 Schematic diagram (not to scale) showing the initial configuration and boundary conditions in an axisymmetric cylindrical coordinate system (r, z). The drop is placed near the free surface of the liquid pool. Gravity $(\mathbf{g})$ acts along negative z axis. The size of the domain is $8D_o \times 16D_o$ with the initial height of the liquid pool as $6D_o$.

The computational domain spans $8D_o \times 16D_o$ with the initial height of the liquid pool as $6D_o$. Here, D_o represents the initial undeformed drop diameter which is placed at $0.02D_o$ from the flat interface. The drop is assumed to be spherical and traveling with an impact velocity U. The computational domain is large enough to neglect the boundary effects on the flow dynamics.

3.2.2 Solution methodology

In the present study, a liquid drop impacts a liquid pool of the same fluid. The one-fluid formulation for the Navier-Stokes equation is used as the governing equation for this study. The modified momentum equation incorporates the surface tension force at the interface.

$$\boldsymbol{\nabla} \cdot \boldsymbol{u} = 0 \ ,$$

$$\rho \left[\frac{\partial \boldsymbol{u}}{\partial t} + \boldsymbol{\nabla} \cdot (\boldsymbol{u}\boldsymbol{u}) \right] = -\boldsymbol{\nabla} p + \boldsymbol{\nabla} \cdot (2\mu \mathbb{D}) + \rho \boldsymbol{g} + \mathbf{F}_s \ .$$

The boundary conditions used are symmetry at the left boundary ($r = 0, z$) and free-slip condition at the right boundary ($r = 8D_o, z$).

$$u = 0 \ , \qquad \frac{\partial v}{\partial r} = 0 \ . \tag{3.1}$$

Outflow boundary conditions are applied on the top surface ($r, z = 16D_o$)

$$\frac{\partial u}{\partial z} = 0 \ , \qquad \frac{\partial v}{\partial z} = 0 \ , \tag{3.2}$$

and no-slip and impervious conditions are used at bottom surface ($r, z = 0$)

$$u = 0 \ , \qquad v = 0 \ . \tag{3.3}$$

The details of the governing equations are defined in Section 2.1.1. The numerical simulations are carried out using the in-house CLSVOF solver described extensively in Section 2.1.4. This solver has been used by many researchers successfully in the past for solving various interfacial flow problems (Deka et al., 2017; Ray et al., 2010; Tomar et al., 2007).

3.2.3 Dimensionless parameters

The governing equations and the boundary conditions are made dimensionless using the drop diameter D_o as the length scale, the impact velocity U as the velocity scale, and $\rho_1 U^2$ as the pressure scale. The pertinent non-dimensional parameters for the present analysis are the Froude number ($Fr \equiv U^2/gD_o$), the Reynolds number ($Re \equiv \rho_1 U D_o/\mu_1$), and the Weber number ($We \equiv \rho_1 U^2 D_o/\gamma$). Here, ρ_1 is the density of the drop, μ_1 is the viscosity of the drop, and γ is the surface tension coefficient between drop and ambient. The Froude number indicates the relative importance of the inertia force over the gravity force, the Reynolds number indicates the importance of inertial forces relative to viscous forces, and the Weber number indicates the relative importance of the inertia force over the surface tension force. In addition, two other relevant dimensionless parameters used for our study are density ratio $\rho_r = \rho_2/\rho_1$ and viscosity ratio $\mu_r = \mu_2/\mu_1$, accounting for the dynamic effect of the surrounding medium.

3.3 Validation

3.3.1 Comparison with literature

In order to check the efficacy of the present solver, we validated the bubble entrainment and thick jet phenomenon with the experimental and numerical data of Morton et al. (2000). Experiments were conducted by impacting a 2.9 mm water drop in a deep-water pool from 170 and 400 mm heights. Figure 3.2 shows the case of impact from 170 mm ($We = 96, Fr = 85, Re = 4480$), and our simulations effectively capture the entrainment of a bubble during the crater collapse. The simulations can predict both the formation and closing of the sub-crater. The only limitation in the numerical method of Morton et al. (2000) was that after the pinch-off, the trapped bubble disappeared since the gas phase dynamics were neglected in their numerical model. However, using the present CLSVOF method, we were able to capture the bubble formation. For the case of drop impact from a height of 400 mm ($We = 248, Fr = 220, Re = 7250$) depicted in Figure 3.3, there was no bubble entrapment; instead, a Rayleigh jet was projected upwards. Due to the instability on the surface of this jet, a secondary drop was formed at the jet tip. Our numerical simulations for this phenomenon predict a diameter of the secondary drop of $0.84D_o$, which agrees well with the diameter measured from the digitized movie images ($\approx 0.80D_o$) and numerical results ($\approx 0.85D_o$) of Morton et al. (2000). Quantitative validation was performed by plotting the cavity depth relative to the initial pool height versus the time for both initial heights of 170 mm and 400 mm. The cavity height (H_{ca}), measured as the depth relative to the initial pool surface level, was made dimensionless using the initial drop diameter (D_o) and (D_o/U) is used as a scale to make the time (t) dimensionless. Figures 3.2 and 3.3 compare the experimental (denoted by blue triangles) and numerical results (green squares) of Morton et al. (2000) with the present numerical studies (red circles), which show a very good agreement.

3.3.2 Grid independence studies

The computational domain is discretized using $280 \times 560 = 1.6 \times 10^5$ grid cells to ensure grid-independent solutions. During the computations, the time steps are chosen to satisfy the Courant-Friedrichs-Lewy (CFL), capillary, and viscous time conditions (Ray et al., 2010). The grid independence tests were performed using three different grids. Simulations were performed for a 3.5 mm drop impact at $U = 2.50$ m/s using the grids

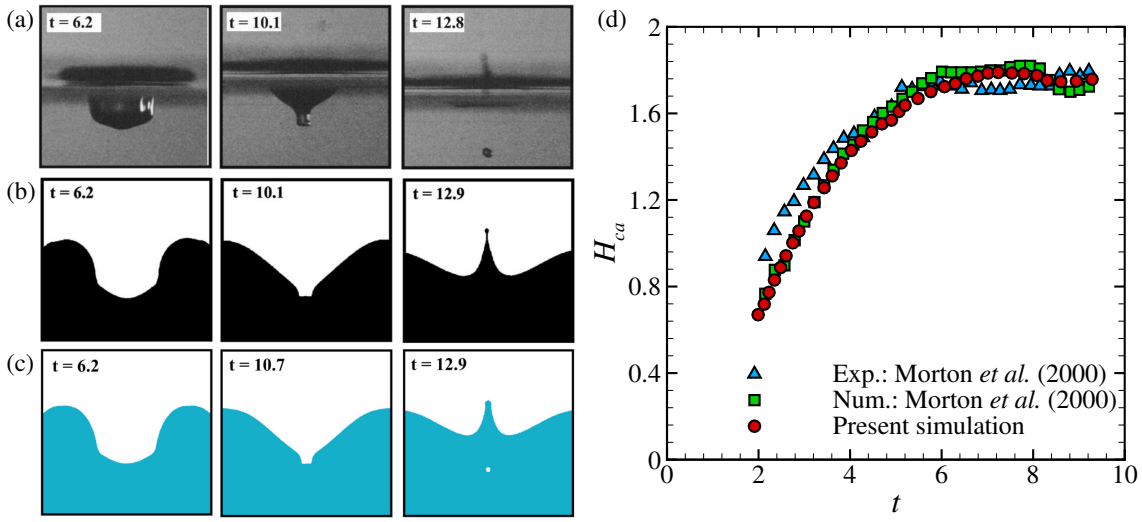

Fig. 3.2 Qualitative comparison between the (a) experimental and (b) numerical results of Morton et al. (2000) with the (c) present results for a 2.9 mm equivalent diameter drop impacting from a height of 170 mm ($Fr = 85, We = 96, Re = 4480$). (d) Quantitative comparison of temporal evolution of the cavity depth.

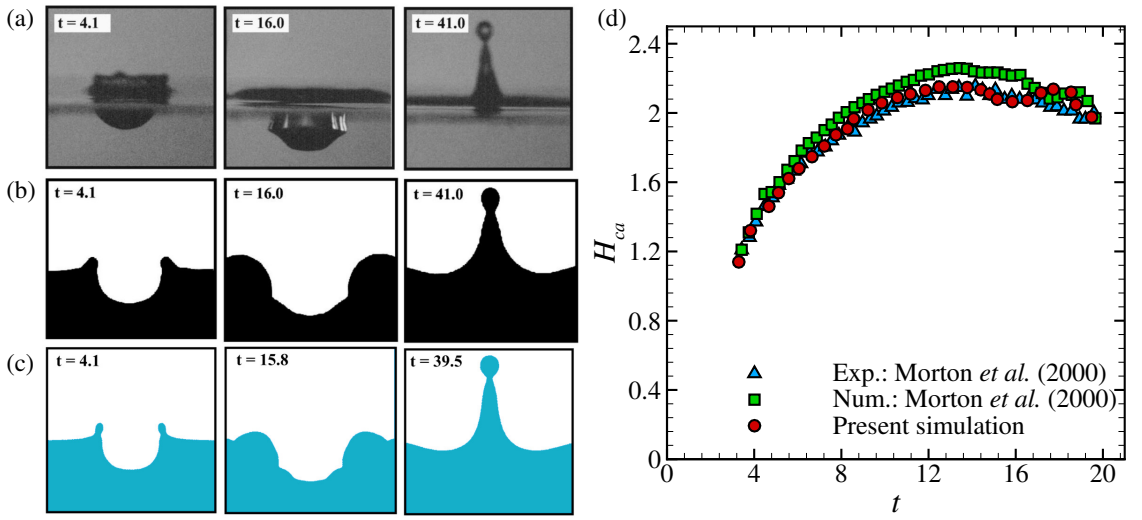

Fig. 3.3 Qualitative comparison between the (a) experimental and (b) numerical results of Morton et al. (2000) with the (c) present results for a 2.9 mm equivalent diameter drop impacting from a height of 400 mm ($Fr = 220, We = 248, Re = 7250$). (d) Quantitative comparison of temporal evolution of the cavity depth.

with 140×280, 280×560, and 560×1120 cells. The corresponding values of D_s/D_o (D_s being the secondary drop diameter) are 0.9138, 0.8935 and 0.8909, respectively. The percentage difference between the values of D_s/D_o for the grids with 280×560 and 560×1120 cells is approximately 0.29%. Thus, a grid with 280×560 cells has been used to generate the rest of the results presented in this study. This grid size ensures optimum computational time without compromising the accuracy of the results.

3.4 Results and discussion

A drop impacting a pool of the same fluid penetrates through the interface and forms a crater. Owing to the high impact velocity, a central jet forms. Under certain conditions, the tip of the jet pinches off due to the Rayleigh-Plateau instability and the secondary drop forms. Many parameters can affect this behavior, of which viscosity, surface tension, and impact velocity are the most important. The present study investigates the effects of high-impact velocity on the formation of secondary drops. To understand the effect, we consider the impact of a 3.5 mm water drop on a deep-water pool at velocities in the range $2.10 \leq U \leq 3.80$ m/s ($128 \leq Fr \leq 421, 212 \leq We \leq 693, 7333 \leq Re \leq 13,270$). Fluid properties of both phases are taken at 20°C. As the drop diameter and fluid properties are held constant, the impact conditions have a constant Bond number of 0.017 ($Bo \equiv \rho_1 g D_o^2/\gamma$). Three different phenomena are observed: (A) long thick central jet with a secondary drop smaller than the primary drop, (B) slender jet with multiple secondary drops, and (C) long thick central jet with a secondary drop larger than the primary drop. For all these phenomena, three basic stages are observed: (i) crater and wave swell (rim of the crater) expansion, (ii) wave swell retraction leading to crater side retraction, and (iii) crater base retraction.

3.4.1 Long thick central jet with smaller secondary drop

The formation of a long thick central jet with a secondary drop that is smaller than the initial drop is observed for low impact velocities, which range from $2.10 \leq U \leq 2.68$ m/s corresponding to $128 \leq Fr \leq 209$. The other dimensionless parameters are $212 \leq We \leq 345$ and $7333 \leq Re \leq 9358$. Due to the inertia force, the crater base is pushed upwards to a W-shaped structure. The crater retraction continues, and a thick jet is finally ejected upwards. The jet grows to a large height, and a large secondary drop is pinched off.

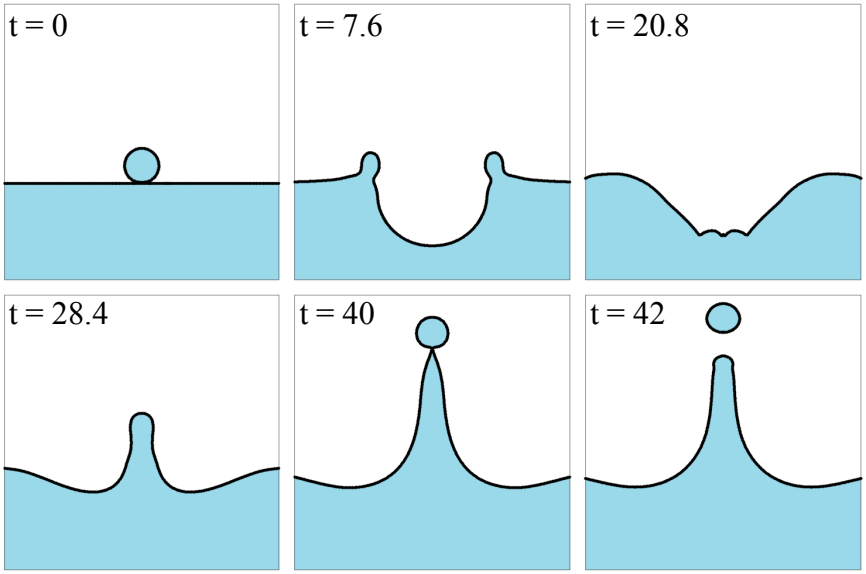

Fig. 3.4 Evolution of the fall of a liquid drop showing the phenomena of formation of long thick jet with a smaller secondary drop ($D_s/D_o < 1$) at different time instants. The corresponding dimensionless parameters are $Fr = 188, We = 310$ and $Re = 8870$.

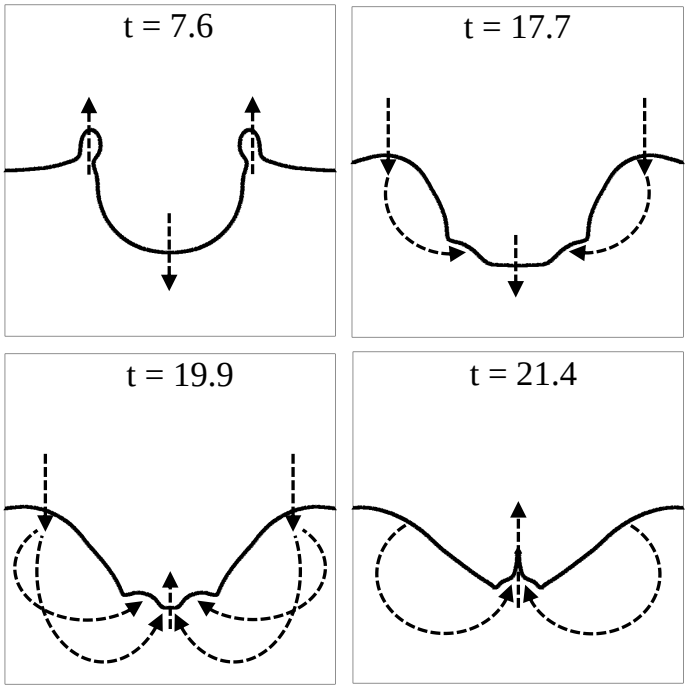

Fig. 3.5 Expansion and retraction stages during the phenomena of formation of long thick jet with a smaller secondary drop ($D_s/D_o < 1$). The arrows denote the typical flow directions.

Figure 3.4 shows the effect of such an impact velocity, the crater formation, and its subsequent retraction leading to the formation of a thick central jet. The flow patterns during the expansion and retraction stages are shown in Figure 3.5. The ratio of the secondary (D_s) to primary drop diameter (D_o) shows that the secondary drop diameter is almost similar to the initial drop diameter, which is evident from the linear fit in Figure 3.6(a). The crater depth remains almost constant for the range of impact velocities. The pinch-off time (t_{pinch}) for the secondary drop increases linearly with the Froude number as observed in Figure 3.6(b). We obtained the following linear regression equations

$$D_s/D_o = 0.00223\ Fr + 0.49\ , \tag{3.4}$$

$$t_{pinch} = 0.18\ Fr + 6.47\ . \tag{3.5}$$

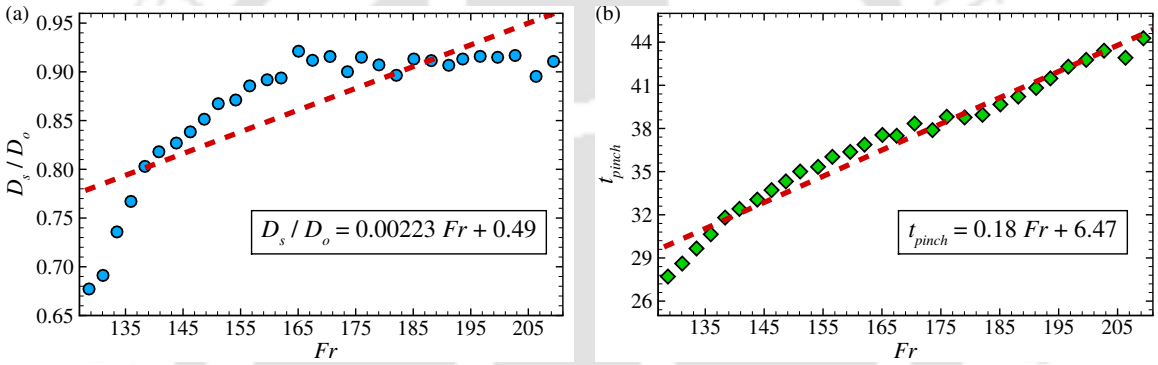

Fig. 3.6 Different quantities vs. the Froude number: (a) secondary to primary diameter ratio (blue circle), and (b) pinch-off time (green diamond). The dashed line represents the linear fit for the corresponding plots, with the fitting value shown in the inset.

3.4.2 Slender jet with multiple secondary drops

The formation of a long thin jet with multiple secondary drops is observed for moderate impact velocities ($2.70 \leq U \leq 3.00$ m/s; $212 \leq Fr \leq 262$). The other dimensionless parameters are $350 \leq We \leq 432$ and $9428 \leq Re \leq 10,476$. As the impact velocity gradually increases, more vertical downward velocity is exerted along the entire crater area. A U-shaped structure with vertical crater sidewalls is formed initially. After the maximum wave swell is reached, the liquid from the wave swell pushes back the crater sidewalls. The crater depth continues to increase, and the retraction of the crater sidewalls begins.

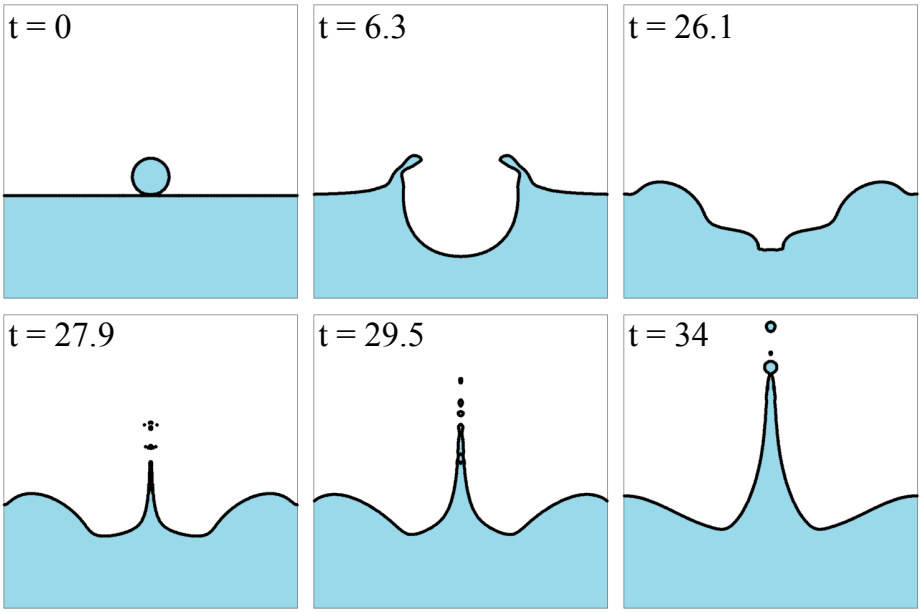

Fig. 3.7 Evolution of the fall of a liquid drop showing the phenomena of formation of long thin jet with multiple secondary drops at different time instants. The corresponding dimensionless parameters are $Fr = 238, We = 393$ and $Re = 9987$.

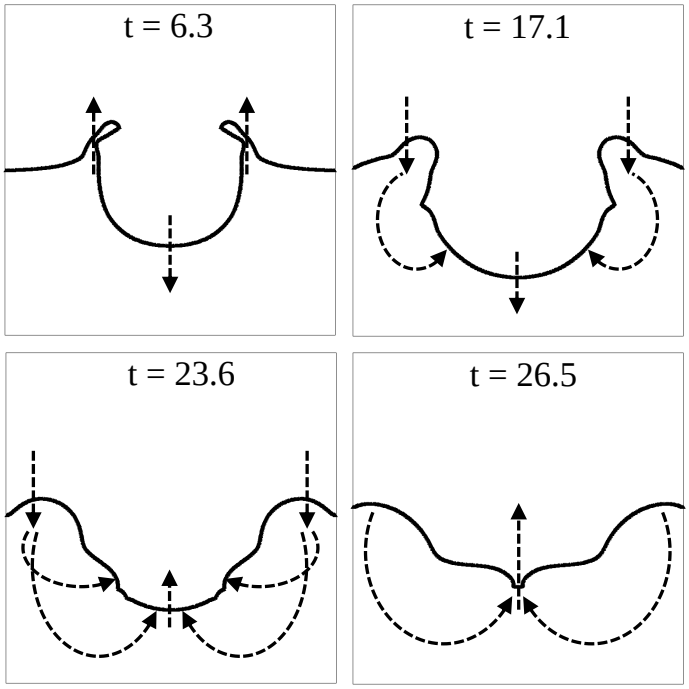

Fig. 3.8 Expansion and retraction stages during the phenomena of formation of long thin jet with multiple secondary drops. The arrows denote the typical flow directions.

Due to the converging flow during retraction, the crater attains a flat and then sharp pointed V-shaped structure, leading to a high-pressure zone at the crater base. As soon as the crater collapses, a thin jet is ejected vertically upwards as can be seen at $t = 27.9$ in Figure 3.7. Due to the reduced jet diameter, the instability leads to the breakup of the jet into numerous drops much smaller than seen earlier. Figure 3.8 shows the flow pattern during the expansion and retraction stages.

3.4.3 Long thick central jet with larger secondary drop

As the Weber number is further increased, the jet transforms from a small thin jet to a long thick jet, as visible in Figure 3.9. The formation of a long thick central jet with secondary drops larger than the original drop is observed for very high impact velocities ($3.02 \leq U \leq 3.80$ m/s; $266 \leq Fr \leq 421$). The other dimensionless parameters are $438 \leq We \leq 693$ and $10,546 \leq Re \leq 13,270$. Due to the greater inertia force during the crater retraction stage, the velocity from the wave swell is higher. High momentum is generated, which pushes more liquid into the central jet. The capillary waves travel slowly, and the pinch-off occurs later, leading to a larger secondary drop. We observe in Figure 3.11(a) that the ratio of the secondary (D_s) to primary drop diameter (D_o) is greater than one, indicating that the secondary drop diameter is larger than the initial drop.

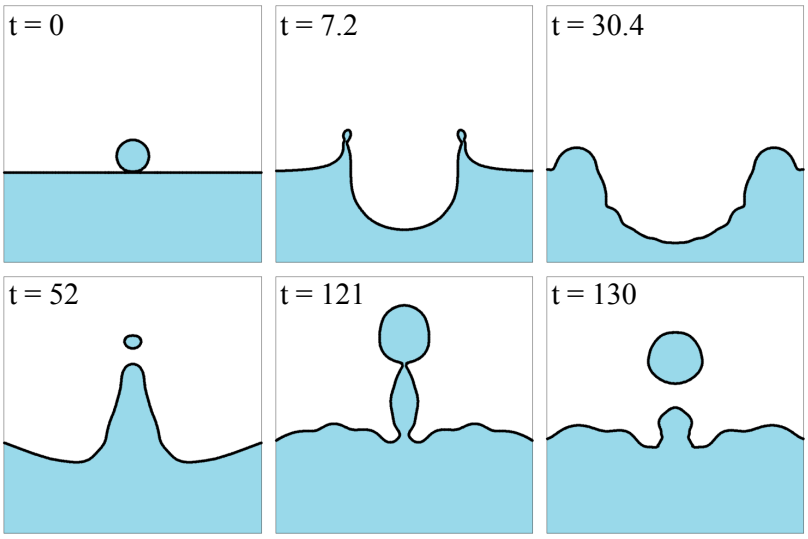

Fig. 3.9 Evolution of the fall of a liquid drop showing the phenomena of formation of long thick jet with a larger secondary drop ($D_s/D_o > 1$) at different time instants. The corresponding dimensionless parameters are $Fr = 407, We = 671$ and $Re = 13,060$.

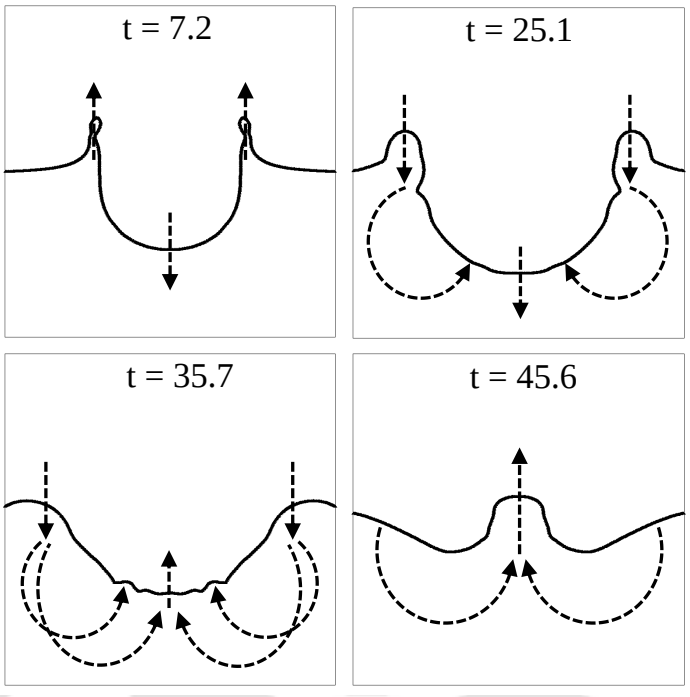

Fig. 3.10 Expansion and retraction stages during the phenomena of formation of long thick jet with a larger secondary drop ($D_s/D_o > 1$). The arrows denote the typical flow directions.

The flow patterns during the expansion and retraction stages are shown in Figure 3.10. For this phenomenon also, the pinch-off time for the secondary drop increases linearly with the increase of Fr, as represented in Figure 3.11(b), but the maximum height reached by the central jet reduces. We obtained the following linear regression equations

$$D_s/D_o = 0.000765\ Fr + 1.18\ , \tag{3.6}$$

$$t_{pinch} = 0.23\ Fr - 5.89\ . \tag{3.7}$$

This phenomenon is observed owing to very high impact velocities or high Weber numbers. Many researchers categorize the thin jet and thick jet phenomena into the splashing zone since these are accompanied by multiple secondary drops. In the systems, such as the rain drops, these are common phenomena since the drops impact from a great height leading to high impact velocities. Due to the greater inertia force, during the crater retraction stage the velocity from the local inventory of liquid in the region

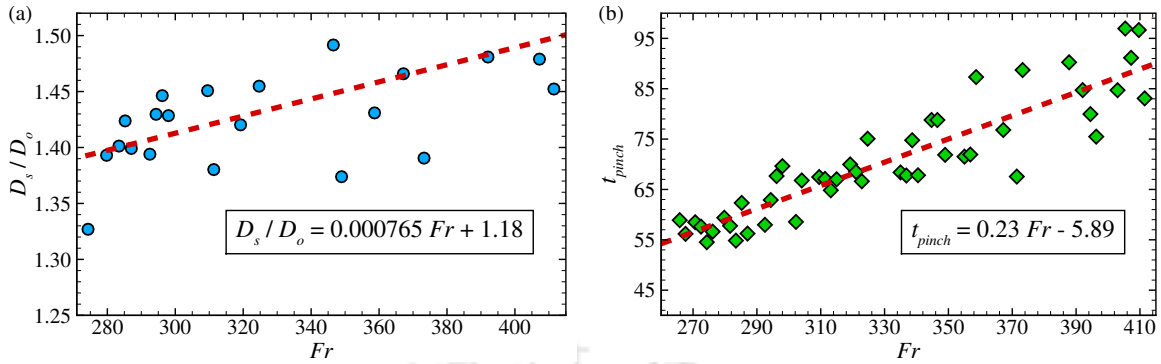

Fig. 3.11 Different quantities vs. the Froude number: (a) secondary to primary diameter ratio (blue circle), and (b) pinch-off time (green diamond). The dashed line represents the linear fit for the corresponding plots, with the fitting value shown in the inset. For this range, we obtain a larger secondary drop diameter compared to the initial drop.

of the wave swell becomes one of the controlling factors. Morton et al. (2000) showed that at impact conditions above the entrainment regime, the surface waves approach the crater base during crater collapse. They indicated the capillary waves by arrows on the sharp corners in the crater wall (see Figure 12 in Morton et al. (2000)) and plotted the radial and axial displacement of the wavefront. The crater retraction continues, and finally, a long thick jet is ejected upwards. The jet grows to a long height, and a few large secondary drops of diameter larger than the initial drop diameter are shed. In Figure 3.9 it is observed that the maximum wave-swell height increases compared to the previous case (see Figure 3.7), and it occurs around $t = 7.2$, at nearly the same instant in time. The maximum crater depth increases, and it occurs at later time $t = 30.4$ than the previous case. The amplitude of the capillary wave increases as the amplitude of the capillary wave is inversely proportional to the surface tension (proportional to We). In conclusion, the regime *Long thick central jet with secondary drop larger than* D_o should be clearly distinguished from the other regimes. The experimental results of Ma et al. (2019) have indicated the possibility of the occurrence of such a situation. However, the present study has identified this regime for the first time. Figure 3.12 shows the ratio of the size of secondary drops to primary drops across the entire range of Fr values that were studied in the numerical simulations. The graph also indicates two linear fits that correspond to the two regimes where secondary drops are formed. The transition zone between these regimes is characterized by the formation of slender jets with multiple secondary drops. Overall, Figure 3.12 provides a detailed insight into the complex dynamics of drop formation and highlights the different regimes where secondary drops are formed.

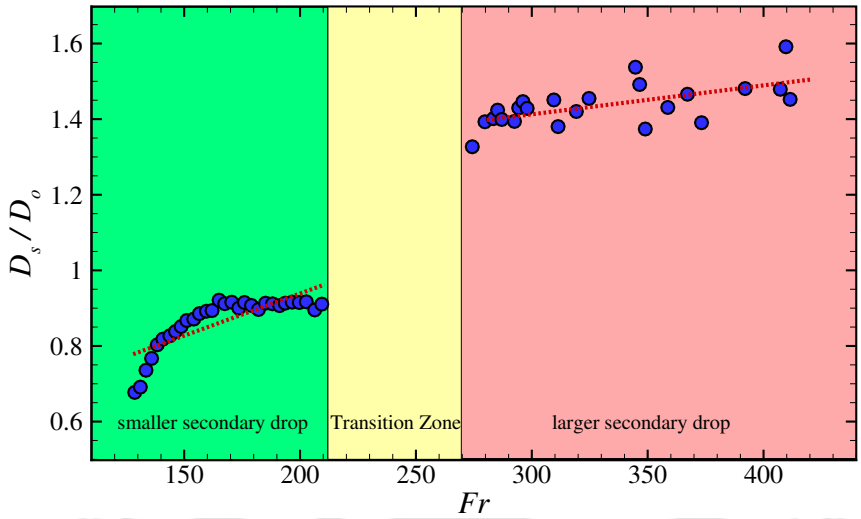

Fig. 3.12 Secondary to primary diameter ratio vs. the Froude number. The dashed line represents the linear fit.

3.4.4 Central jet characterization

The series of phenomena observed when a drop coalesces on a liquid pool are: the short thick jet phenomenon, the short thick jet phenomenon with a secondary drop, the thin jet phenomenon, the thin jet phenomenon with large bubble entrapment, the long thick jet phenomenon with small bubble entrapment and the long thick jet phenomenon. Three basic stages are seen for all these phenomena involving jet formation: (i) crater and wave swell (rim of the crater) expansion, (ii) wave swell retraction leading to crater side retraction, and (iii) crater base retraction. The complete coalescence, crater formation, and subsequent jet formation with a secondary drop can be interpreted as the bouncing of a primary drop. The coefficient of restitution can be defined for such a situation. Earlier, Honey and Kavehpour (2006) developed a theory for the height of an emanating jet based on this concept. Ma et al. (2019) have estimated energy conversion during the impact process using a numerical integration method. It is concluded that the ratio of the secondary drop to the initial drop diameter is approximately within 1.2 to 2, and this diameter ratio correlates linearly with the Froude number. These findings, especially the diameter ratio and its dependence on the Froude number are in close agreement with the present results as obvious from Figures 3.6 and 3.11.

As described earlier, the three phenomena produce jets having different heights and tip velocities. Subsequently, the central jet breaks up and pinches off a secondary

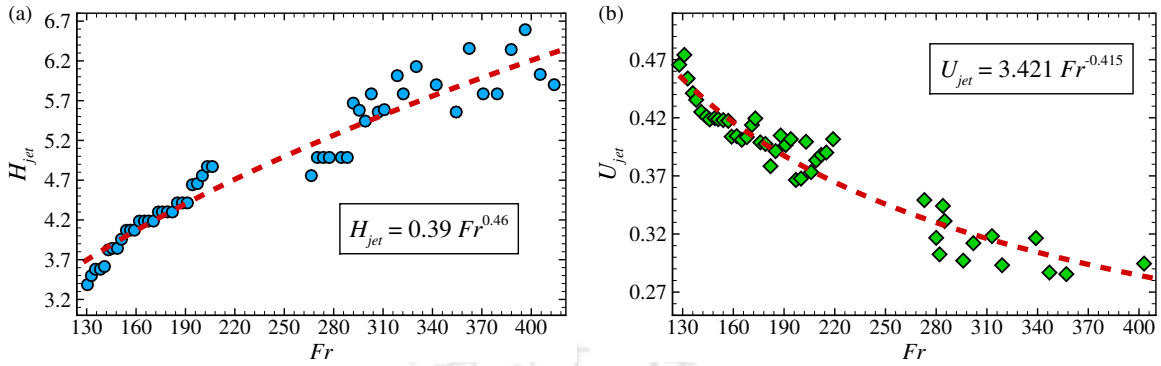

Fig. 3.13 Different quantities vs. the Froude number: (a) central jet height (blue circle), and (b) jet velocity (green diamond). The dashed line represents the linear fit for the corresponding plots, with the fitting value shown in the inset.

drop, whose quantification has been done earlier. To understand the jet dynamics, in Figure 3.13, we plot the normalized jet velocity (U_{jet}) and normalized jet height (H_{jet}) as a function of the impacting speed quantified by the Froude number (Fr). The jet velocity is normalized using the initial impact velocity (U) and is measured when the jet tip passes the free surface level. The jet height is normalized using the initial drop diameter (D_o). Considering an energy balance Fedorchenko and Wang (2004) theoretically derived a relation for the central jet height as $H_{jet} = 1.43\ Fr^{0.25}$, while in our present study we found the relation as

$$H_{jet} = 0.39\ Fr^{0.46} \tag{3.8}$$

Fedorchenko and Wang (2004) also stated the expression for the central jet velocity as $U_{jet} = 0.913\ Fr^{-0.375}\ \cot(\alpha/2)$, where 2α is the cone vertex angle. We also calculated the central jet velocity (U_{jet}) and found the variation with Froude number as

$$U_{jet} = 3.421\ Fr^{-0.415} \tag{3.9}$$

3.5 Summary

The present chapter explores the culmination of a series of phenomena during the impact of a water drop on a deep pool of water. The evolution of the outward jets that form during the collapse of the crater can produce secondary drops. The dimensionless jet velocity can be expressed as a function of the Froude number, Weber number, and the minimum radius of the cavity. Depending on Fr and We, three different scenarios

emerge with the formation of a central jet and the pinch-off of one or more secondary drops. At low impact velocities, a long thick central jet is formed, finally forming a secondary drop which is always smaller than the initial drop. For moderate impact velocities still, a long jet emanates, which is much thinner than in the previous case entailing the breakup of the jet into multiple secondary drops, which are all smaller than the initial drop. In the third paradigm of very high impact velocities, which was clearly identified here for the first time, the emanating jet is long and thick, leading to the pinch-off of a secondary drop, which has a larger diameter than the initial drop. Similar to the case with a long thick jet and a singular secondary drop smaller than the initial drop, in this new regime with an evolving larger drop than the original one, linear relations are observed for the pinch-off time and the maximum jet height as a function of the Froude number.

Chapter 4

Electrohydrodynamic induced interactions between drops

Dispersion of drops in an emulsion is commonly seen in several chemical, pharmaceutical, and petroleum industries. An electric field has been shown to affect the stability of these dispersions. A pair of drops may coalesce or repel each other in the presence of an electric field. However, the inclusion of inertia permits interesting transient behavior, where the drops may attract due to the electrostatic dipole-dipole attraction. This chapter, considering a finite Reynolds number, investigates the dynamics of a pair of leaky dielectric drops/emulsions suspended in a leaky dielectric liquid. The chapter starts by summarizing the previous investigations performed for such interacting pairs (§ 4.1). Then, the computational model used to study electrohydrodynamic flows is described (§ 4.2). Next, the model is validated with earlier studies (§ 4.3). The effects of considering a finite Reynolds number are subsequently explored, and the transient dynamics of drop/emulsion pairs are outlined (§ 4.4). The chapter then concludes with a summary of the outcomes (§ 4.5).

4.1 Introduction

An emulsion is a dispersion of drops of one fluid in another. Emulsions are ubiquitous in nature and are extensively used in chemical, coating, food, cosmetics, agriculture, and medical industries to achieve products with desired properties (Eow and Ghadiri, 2002). Usually, emulsions are stabilized by using compatible surfactants, also called emulsifiers. While the stability of emulsions is desired in most applications, in some applications, naturally occurring emulsions need to be phase separated. Application of an electric

field across an emulsion has been shown to affect the stability of emulsions (Barnes, 1994; Goodarzi and Zendehboudi, 2019; Kilpatrick, 2012). A drop placed in an electric field polarizes due to the difference in electrical properties with the suspending fluid. The balance between the electrostatic and viscous fluid stresses results in either oblate or prolate drop deformation (Taylor, 1966). Other complex dynamics are observed at strong fields, such as break up, streaming from poles or equator, and electrorotation (Das and Saintillan, 2017b; Sengupta et al., 2017; Wagoner et al., 2020; Wang et al., 2019). While studies on isolated drops are abundant (Vlahovska, 2019), investigations of the collective dynamics of many drops are scarce (Fernández, 2008a,b). The studies on drop dynamics and interactions at arbitrary separations have been considered mainly in the case of drop pairs aligned with the electric field (Mhatre et al., 2015a; Zabarankin, 2020). Baygents et al. (1998) performed axisymmetric simulations of interactions between two leaky-dielectric drops in leaky-dielectric ambient fluid and showed that the hydrodynamic forces dominate the electrostatic forces in the limit of a small Reynolds number and dictate the stability of emulsions. Tomar et al. (2007) proposed a CLSVOF-based method to simulate two-phase electrohydrodynamics and agreed with the results of Baygents et al. (1998). Studies are also conducted on electric field applied at an arbitrary angle to the line joining the centres of the drops (Dong and Sau, 2018; Mhatre et al., 2015a; Sorgentone et al., 2021). The result was not a simple attraction or repulsion, but rather depending on the configurations, drops could move towards each other and then separate in transverse directions.

In this chapter, we use a finite Reynolds number to investigate drop-drop interactions in single and double emulsions in an electric field. The scaling for the relative velocity between the interacting drops is studied, which can vary depending upon the Reynolds number of the flow generated by the tangential electric stresses. By comparing time scales for charge relaxation in the drop and the ambient fluid with that of the viscous time scale, we show that the transient behavior of an emulsion in an externally applied electric field can be explained. The drops can attract for particular electrical properties. However, the coalescence phenomenon is delayed due to the slow drainage of the film between the drops, and a drop-pair doublet is formed. These nonlinear effects due to the finite Reynolds number have not been explored earlier. We also study the behavior of compound drops in an electric field and the effect of the electric field on the drop-drop interactions between compound drops.

4.2 Formulation

4.2.1 Computational domain

We study the interaction dynamics of a pair of leaky-dielectric single and compound drops in a leaky-dielectric ambient fluid under the influence of an externally applied electric field in an axisymmetric cylindrical coordinate system (r, z). The initial configuration of the emulsion drops for the computations is shown in Figure 4.1. The dashed line marks the axis of symmetry. The extent of the domain in both the radial and axial directions is $16a$, where a is the radius of the outer shell of the compound drop. The inner core of the compound drop has a radius of $a/3$. The initial separation distance between the drops is $h = 4a$. In the studies of single emulsion, the inner core is absent. The properties of the shell of the compound drop are denoted by subscript 1, whereas the ambient fluid and the core of the compound drop are denoted using the subscript 2. The drops are neutrally buoyant with densities $\rho_1 = \rho_2$. Viscosity of the fluids 1 and 2 are given by μ_1 and μ_2, respectively. Electric permittivities and

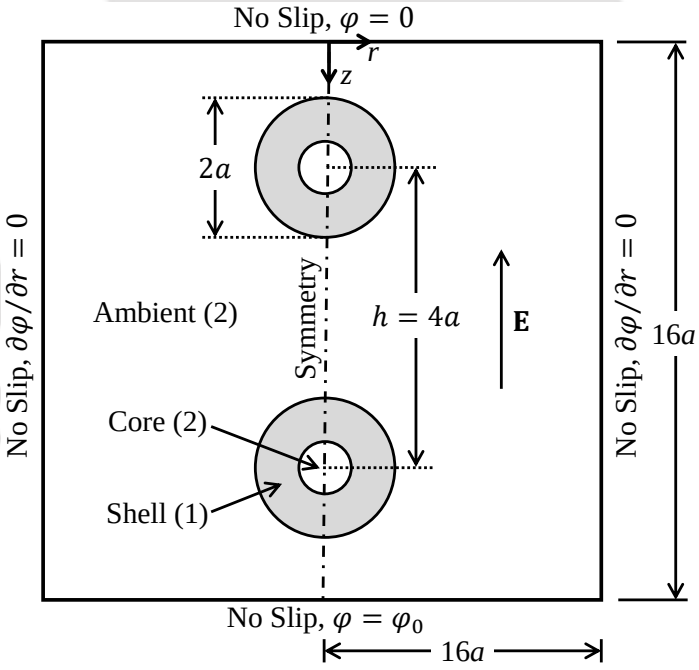

Fig. 4.1 Schematic diagram (not to scale) showing a pair of compound drops interacting in the presence of an externally applied electric field in an axisymmetric cylindrical coordinate system (r, z). The radius of the outer drop (shell) and the inner drop (core) are a and $a/3$, respectively. Electric field ($\mathbf{E}$) is applied along negative z axis. The size of the domain is $16a \times 16a$.

conductivities are ε_1 and σ_1, respectively, for the shell, and ε_2 and σ_2 for the core and ambient fluid. The fluids involved are assumed to be incompressible, and Newtonian, and the surface tension coefficient of the interface between the two fluids is given by $\gamma_{12} = \gamma$. The chosen computational domain is large enough to neglect the effect of boundaries on the dynamics of the drops at the time scales considered in this study.

4.2.2 Solution methodology

The two-phase system discussed above is governed by the modified incompressible Navier-Stokes equations using the one-fluid formulation. The modified momentum equation incorporates the surface tension force at the interface and the electric force for the volume.

$$\boldsymbol{\nabla} \cdot \mathbf{u} = 0 \,,$$

$$\rho \left[\frac{\partial \mathbf{u}}{\partial t} + \mathbf{u} \cdot \boldsymbol{\nabla} \mathbf{u} \right] = -\boldsymbol{\nabla} p + \boldsymbol{\nabla} \cdot (2\mu \mathbb{D}) + \boldsymbol{\nabla} \cdot \varepsilon \left(\mathbf{E}\mathbf{E} - \frac{E^2}{2} \mathbf{I} \right) + \gamma \kappa \delta_s \hat{\mathbf{n}} \,.$$

An external electric field ($\mathbf{E}$) is applied along the axial direction. It is imposed by applying electric potential φ using the boundary condition on the bottom boundary $(r, z = 16a)$

$$\varphi = \varphi_0 \,, \qquad u = v = 0 \,. \tag{4.1}$$

The top boundary is electrically grounded using the boundary condition $(r, z = 0)$

$$\varphi = 0 \,, \qquad u = v = 0 \,. \tag{4.2}$$

Neumann boundary condition for the electric potential is imposed on the right boundary $(r = 16a, z)$

$$\frac{\partial \varphi}{\partial r} = 0 \,, \qquad u = v = 0 \,. \tag{4.3}$$

Symmetry boundary conditions are imposed on the axis of symmetry for the velocity field and the electric potential $(r = 0, z)$

$$\frac{\partial \varphi}{\partial r} = 0 \,, \qquad u = 0 \,, \qquad \frac{\partial v}{\partial r} = 0 \,. \tag{4.4}$$

No-slip and impervious velocity conditions are imposed on the other boundaries. The details of the governing equations are defined in Section 2.2.1. The numerical simulations are carried out using the Basilisk solver described extensively in Section 2.2.2.

4.2.3 Dimensionless parameters

The governing equations and the boundary conditions are made dimensionless using the drop radius a as the length scale, U_e as the velocity scale which is defined based on the flow generated by the electric forces, and $\rho_2 U_e^2$ as the pressure scale. The scaling for velocity generated due to the electric forces can be obtained by balancing viscous stresses with Maxwell stresses at the interface. The scale for the velocity is thus given by $U_e \sim a\varepsilon_2 E_\infty^2/\mu_2$, where E_∞ is the scaling factor for the electric field. The following dimensionless parameters govern the dynamics of drops due to electrostatic forces and the flow generated by them. Electric capillary number $Ca_E = \varepsilon_2 E_\infty^2 a/\gamma$ gives the ratio of relative magnitudes of the electric forces and interfacial tension force, which are the two forces balanced to obtain the drop deformation. Reynolds number, based on U_e, can be defined as, $Re = \rho_2\varepsilon_2 a^2 E_\infty^2/\mu_2^2$, which gives the ratio of inertial forces to the viscous forces. An electrical equivalent of the hydrodynamic Reynolds number can also be defined by taking the ratio of charge convection to conduction as $Re_E = \varepsilon_2 U_e/a\sigma_2$. Feng (1999) showed that the electric Reynolds number has an effect on the extent of deformation of the drop. The two phase system can be categorized by the following ratios of different properties: $\rho_r = \rho_1/\rho_2$, $\mu_r = \mu_1/\mu_2$, $R = \sigma_1/\sigma_2$, and $Q = \varepsilon_1/\varepsilon_2$. A detailed derivation of the dimensionless equations is described in Appendix B.

We note here that in the above scaling for velocity, a factor of $(1-\tau_e^1/\tau_e^2)R/(R+2)^2$ would yield a more appropriate scaling following the solution for velocity given in Taylor (1966), where, $\tau_e^1 = \varepsilon_1/\sigma_1$ and $\tau_e^2 = \varepsilon_2/\sigma_2$, are the charge relaxation time constants for fluid 1 and fluid 2, respectively. Indeed, in our simulations for $\tau_e^1 = \tau_e^2$, no electrohydrodynamic flow is observed (not shown here). Thus, the above scaling for velocity, in some cases, may be an order of magnitude different from the observed values. However, for non-dimensionalizing velocity, we use U_e defined above as also proposed in Baygents et al. (1998), since it allows the delineation of the effects of electrical parameters while comparing results for different values of R and Q. Nevertheless, later when we compute scaling for electrostatic and hydrodynamic forces, as well as, flow, interface and charge relaxation time scales, we account for the effect of other electrical properties of the fluids on velocity scaling.

Another important parameter that requires attention is the amount of free charge per unit area that develops at the interface: $q_s \sim 3\varepsilon_2 E_\infty(1-\tau_e^1/\tau_e^2)/(R+2)$ (computed from an exact solution for a spherical drop). The ratio of the charge relaxation time constants for the two fluids, (τ_e^1/τ_e^2), in the above expression, essentially indicates the nature of the charge distribution on the surface of the drop. If the ratio is greater than

one, the outer fluid carries away the charge rapidly, and a negative charge develops at the interface, whereas if the ratio is less than one, the inner fluid supplies positive charge in response to the applied electric field, at a more rapid rate than the ambient fluid can carry that away, and thus a positive charge accumulates at the surface. The positive or negative charge determines the direction of the tangential stress and thus also the sense of circulation produced by the electrohydrodynamic forces, which in turn determines whether the nature of the interaction between the drops is attractive or repelling. At low Reynolds number, hydrodynamic viscous forces are stronger and drive the interaction between the drops, whereas at higher Reynolds numbers, the relative velocity during attraction is governed by the electrostatic interaction between the drops.

4.3 Validation

4.3.1 Comparison with literature

We validate the numerical model used in this study by comparing the deformation of a drop with the theoretical predictions (Ajayi, 1978; Taylor, 1966), and previous computational studies (Tomar et al., 2007). We consider a drop of radius a placed at the center of the domain (see Figure 4.1), and an electric field is applied. We perform all the computations up to the steady state in an axisymmetric domain of size $16a \times 16a$. Figure 4.2 shows the variation in degree of deformation D with R for a fixed permittivity ratio of $Q = 10$. The other dimensionless parameters used for this validation study are $Ca_E = 0.18$, $Re = 0.10$, $Re_E = 0.01$, $\rho_r = 1$, and $\mu_r = 1$. Taylor (1966) provided an analytical expression (Equation (4.5)) for the deformation of a drop as a function of the fluid properties and the electric field intensity, in the limit of small deformation, as D, where $D = (L - B)/(L + B)$ is the Taylor deformation parameter, with L being the length of the drop along the direction of the electric field and B is the width of the drop in the direction perpendicular to the applied electric field.

$$D = \frac{9}{16}\frac{Ca_E}{(2+R)^2}\left[R^2 + 1 - 2Q + \frac{3}{5}(R-Q)\frac{2+3\mu_r}{1+\mu_r}\right] \tag{4.5}$$

In the presence of an electric field, depending on the electrical properties of the two phases, a drop deforms either into an oblate ($D < 0$) or a prolate shape ($D > 0$). We observe that the drop deforms into an oblate shape for low values of R, and into a

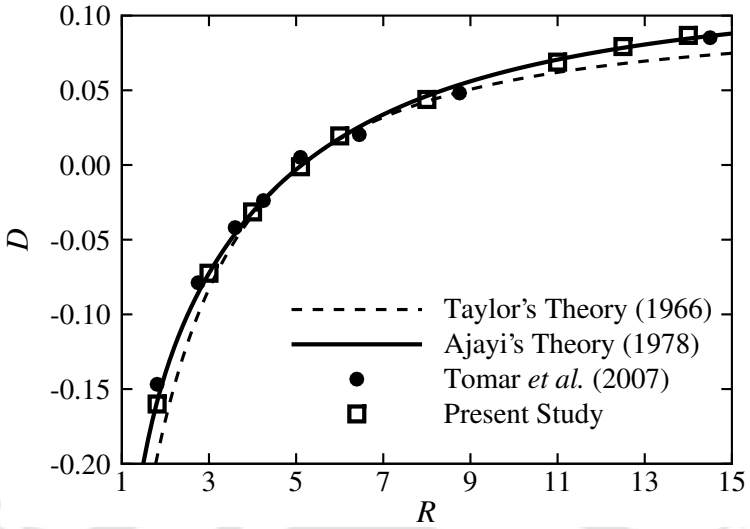

Fig. 4.2 Comparison of deformation (D) of a single drop with theoretical and computational studies. Other dimensionless parameters for the computations are $Q = 10$, $Ca_E = 0.18$, $Re = 0.10$, $Re_E = 0.01$, $\rho_r = 1$, and $\mu_r = 1$.

prolate shape for higher values of R. We also observe that for small drop deformation there is good agreement between the computational results with the theory of Taylor (1966) and only at larger D, there is deviation from the theory essentially due to the breakdown of the assumption of linearity. Comparison with the second order theory of Ajayi (1978) shows good agreement with the simulated results.

4.3.2 Grid independence studies

We exploit the Adaptive Mesh Refinement (AMR) capability of the present solver to enhance computational efficiency while maintaining the required accuracy of the simulations. We employ the AMR using a cost function based on the volume fraction gradient, thus using a very fine mesh near the interface while maintaining a relatively coarser mesh elsewhere. As mentioned in Section 2.2.3, the domain is divided into smaller volumes where the size of the cell is represented by its level l. We use the Taylor deformation parameter D to compare numerical convergence with the increase in refinement. We perform the computations up to the steady state using a drop of radius a in an axisymmetric domain of size $16a \times 16a$. The parameters used for the study are $R = 0.1$, $Q = 2$, $Ca_E = 0.2$, $Re = 5$, $Re_E = 0.01$, $\rho_r = 1$, and $\mu_r = 1$. Simulations using different grid sizes are performed, and the temporal evolution of D is plotted as shown in Figure 4.3. The curves corresponding to $a/\Delta x_{min} = 256$ ($l = 12$)

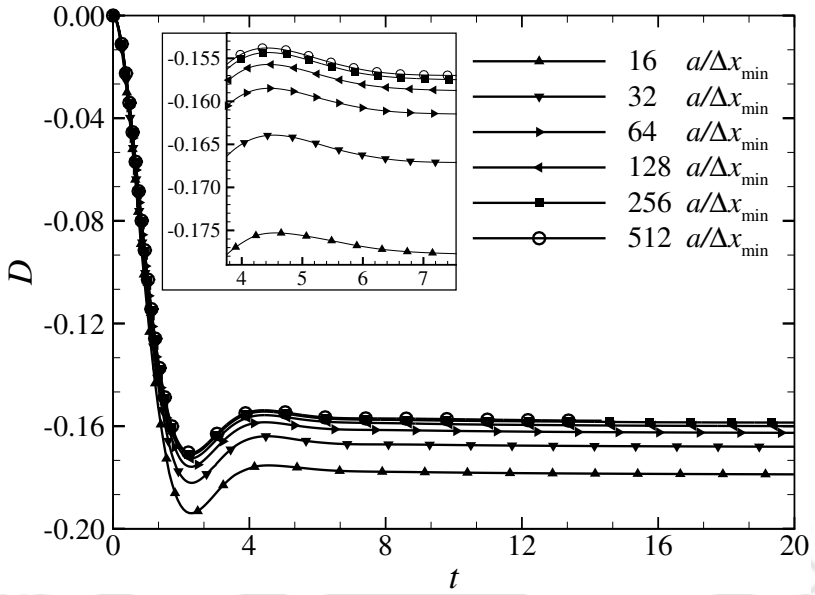

Fig. 4.3 Temporal variation of deformation D of the drop under a steady electric field, using six different grid refinements. The inset shows the zoomed view for better convergence analysis. The parameters considered for the simulations are $R = 0.1$, $Q = 2$, $Ca_E = 0.2$, $Re = 5$, and $Re_E = 0.01$.

and 512 ($l = 13$) are very close with a maximum difference of 0.28%. Here, Δx_{min} is the minimum grid size used in the simulations. The entire interface is resolved using Δx_{min}, and the grid is progressively coarsened away from the drop. Based on the grid independence study, we use $a/\Delta x_{min} = 256$ for the rest of the simulations presented in this study.

4.4 Results and discussion

In this section, we study the dynamics and interactions of a one/pair of drops, single and compound, suspended in another immiscible fluid under the action of an externally applied electric field. For all the studies we assume $Re_E = 0.01$, $\rho_r = 1$ and $\mu_r = 1$. First, we present results for drops in a single emulsion. Subsequently, we discuss the studies for compound drops. Based on the interaction dynamics, we comment on the stability of an emulsion in the presence of an electric field.

4.4.1 Interaction dynamics of single emulsion

The accuracy of Taylor's linear theory has been discussed in several previous studies (Ajayi, 1978; Feng, 1999), especially in the context of a not-so-good agreement with some of the experiments of Torza et al. (1971) for low conductivity fluids. In particular, the drop deformation is expected to be proportional to E_∞^2 from the theory. However, the experiments of Torza et al. (1971) showed only qualitative agreement, and the extent of deformation in some cases was over two folds of the predictions from the theory. Feng (1999) suggested that the possible origin of this discrepancy could be due to the neglect of charge convection in Taylor's theory. At low but finite electric Reynolds numbers (Re_E), the deviation was significant, especially for very low conducting fluids such as silicon and castor oils.

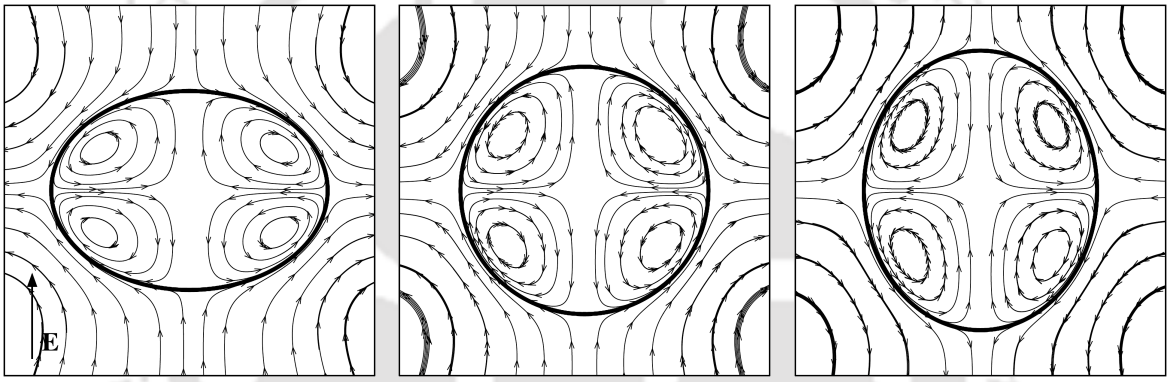

(a) $R = 1.81$ (b) $R = 5.1$ (c) $R = 14$

Fig. 4.4 Streamlines and variation in the drop shape for different conductivity ratios. The other computation parameters are $Q = 10$, $Ca_E = 0.18$, and $Re = 0.10$.

Figure 4.4 shows the drop shapes and the streamlines of the flow generated by the tangential electric forces. Due to the accumulation of the free charge at the drop interface, a tangential electric force acts at the interface that leads to fluid flow inside the drop as well as in the ambient fluid, as shown in Figure 4.4 for three different values of R. Other parameters for all three cases are $Q = 10$, $Ca_E = 0.18$, and $Re = 0.10$. For $R = 1.81$ and $R = 5.1$, the flow is from poles to the equator, resulting in the oblate shape for $R = 1.81$, but the drop remains spherical for $R = 5.1$. This no-deformation case ($R = 5.1, Q = 10$) corresponds to the electrical and fluid properties for which the Maxwell stresses are exactly balanced by the normal viscous stress and the surface tension forces for a spherical-shaped drop. Nevertheless, non-zero tangential electric stresses generate a flow from poles to the equator, as shown in Figure 4.4(b). The

switch-over of the flow from poles-to-equator to equator-to-poles occurs when $R > Q$ as shown in the Figure 4.4(c) for $R = 14$ and $Q = 10$. All the computations shown here are in good agreement with the analytical results, as well as with the previous computational studies (López-Herrera et al., 2011; Tomar et al., 2007).

We now investigate the interaction dynamics of a pair of drops in a single emulsion in the presence of an electric field. The computational domain is the same as defined in Section 4.2.1, with the only change of no inner core. Charge accumulation at the interface of initially neutrally charged drops results in the formation of charge dipoles, and the drops interact electrostatically through dipole-dipole electrostatic forces. In the large separation limit, the electrostatic force between the drops can be proportional to E_∞^2/h^4, where h is the center-to-center spacing between the drops. On the other hand, flow generated by the electric stress would generate a drag proportional to the relative velocity in the low Re limit. Thus, the hydrodynamic drag force on one drop due to the flow generated by the other is proportional to E_∞^2/h^2. However, at higher Re, the hydrodynamic drag is proportional to velocity square, and thus a drag force proportional to E_∞^4/h^4 should be expected. Simulations presented in this study are for low Re values, and therefore we expect the linear drag law to be valid.

As discussed earlier, the flow direction depends upon the sign of $(1 - \tau_e^1/\tau_e^2)$, which is also expected to govern the hydrodynamic interactions between the drops in an emulsion. Based on the convection currents, the drops are expected to move towards each other for $\tau_e^1/\tau_e^2 > 1$, or equivalently, $R < Q$, whereas they will move away from each other for $\tau_e^1/\tau_e^2 < 1$, that is, $R > Q$. Here, we present two cases with parameters chosen from Baygents et al. (1998) such that the drops attract in the first case with

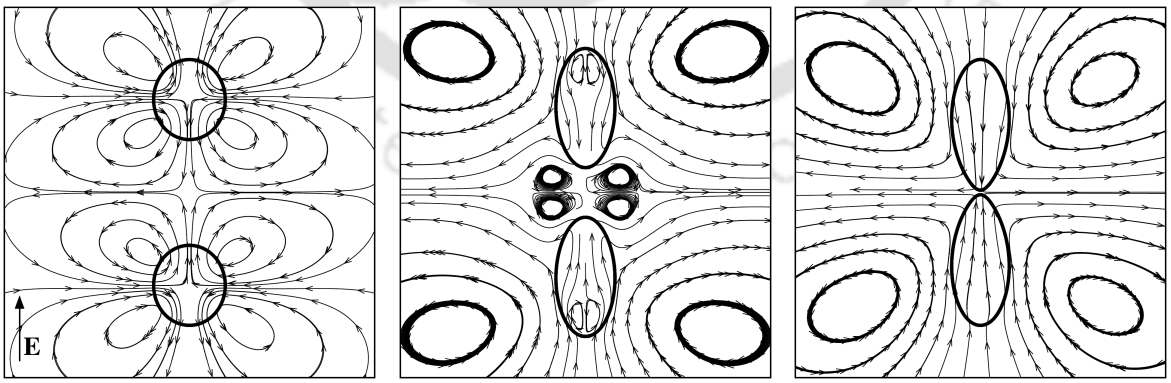

(a) $t = 1$ (b) $t = 20$ (c) $t = 30$

Fig. 4.5 Drop interaction along with the streamline patterns observed for $R = 6$ and $Q = 8$ at $Ca_E = 1.5$ and $Re = 0.10$.

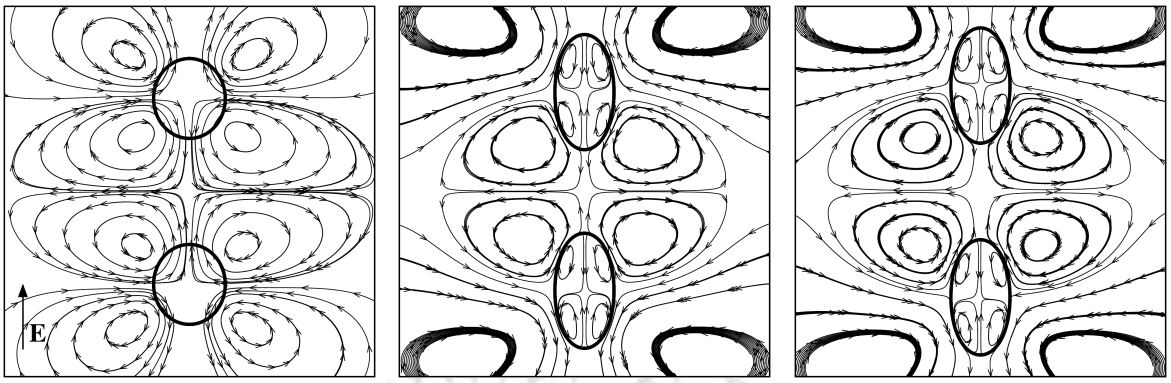

(a) $t = 1$ (b) $t = 40$ (c) $t = 120$

Fig. 4.6 Drop interaction along with the streamline patterns observed for $R = 1.04$ and $Q = 0.2$ at $Ca_E = 1.5$ and $Re = 0.10$.

$R = 6$ and $Q = 8$ ($\tau_e^1/\tau_e^2 = Q/R = 1.33 > 1$) as shown in the Figure 4.5 and therefore render the emulsion unstable. In contrast, the drops repel each other for $R = 1.04$ and $Q = 0.2$ ($\tau_e^1/\tau_e^2 = Q/R = 0.2 < 1$) as shown in Figure 4.6, and the electric field is expected to stabilize the emulsion. In the first case with $\tau_e^1/\tau_e^2 > 1$, charge develops very quickly, $t \sim 0.02 \ll 1$, much faster than the morphological evolution of the drop $t \sim 2$. Also, the morphological evolution is much faster than the drop migration timescale $t \sim 40$. Thus, the drops first deform and then, without deforming much, migrate either towards each other or away depending upon the ratio τ_e^1/τ_e^2. The streamlines for $t \sim 1$ are similar (see Figures 4.5(a) and 4.6(a)) for both the cases due to the initial prolate deformation. Subsequently, the electric stresses result in a flow that is opposite for the two cases, as shown in Figures 4.5(b) and 4.6(b). Drops in Figure 4.5 coalesce, whereas those shown in Figure 4.6 move apart.

Figure 4.7 shows the variation in the charge density on the drop surface for different time instances. As discussed earlier, the sign of the charges developing on the drop surface is opposite for the two cases. Free charge distribution on the interface for a spherical shaped drop is given by $q_s \cos(\theta)$, where the angle θ is measured from the horizontal direction aligned with the applied electric field (as marked in the inset of Figure 4.7). Thus, the charge is maximum at the poles and zero at the equator. In the first case, a negative charge develops on the northern hemisphere of the drop, with the axis of the drop aligned with the electric field, whereas a positive charge appears in the second case. Initially, the charge develops symmetrically on the northern and southern hemispheres when the drops are far apart, similar to the isolated drop case. However, when the interfaces of the drops come closer than one diameter due to non-uniformity

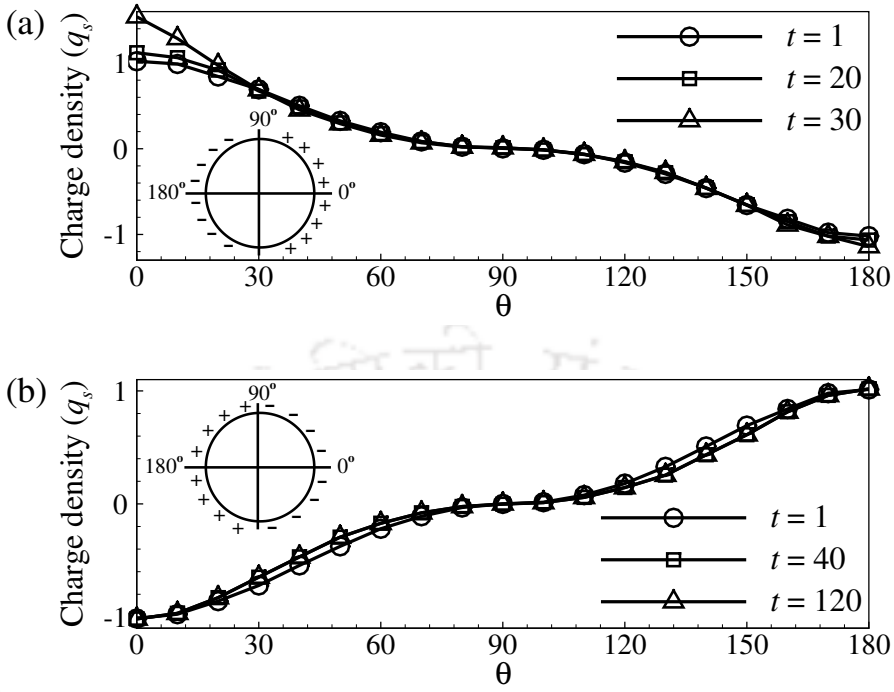

Fig. 4.7 Temporal variation in surface charge density (q_s) along the interface and the charge distribution around the interface for (a) $R = 6$ and $Q = 8$ and (b) $R = 1.04$ and $Q = 0.2$ at $Ca_E = 1.5$ and $Re = 0.10$.

in the electric field in the region between the drops, the charge increases in the regions where the drops face each other.

The dynamics of the drops shown in the sequence of images in Figures 4.5 and 4.6 can be understood by comparing the time scales for the different phenomena active during the interaction between the drops. The time scale of charge accumulation at the drop surface is given by τ_e/τ_q, which is much shorter due to the relatively high conductivities of the fluids considered in the simulations presented in this study. Here, τ_e is the charge relaxation time constant, and τ_q is the inertial capillary time scale. The time scale for the development of the flow due to the tangential electric stresses is given by the time scale for the diffusion of the momentum $\tau_\mu \sim h^2\rho_2/\mu_2$, where h is the distance between the drops. Thus, $\tau_\mu/\tau_q \sim (h/a)^2(Re/Ca_E)^{1/2} \sim (h/a)^2/Oh$ yields the time scale for the influence of the electric stress driven flow near one drop to reach the other drop. Here, $Oh = \sqrt{Ca_E/Re}$ represents the Ohnesorge number. If the drops are far apart, it will take longer for the flow to develop. Thus, electrostatic forces may initially influence the drops before being overtaken by the hydrodynamic forces. Similarly, for low Re values, even for drops as close as $h/a \sim 5$, τ_μ/τ_q will be large,

and drops would first respond to the attractive electrostatic forces. Thus, to determine the nature of the interaction between the drops, it is not sufficient to examine the ratio of the relaxation time constants (or the direction of the electrically driven convective flow) alone. Baygents et al. (1998) also suggested that, in the low Reynolds number limit, the drops interact hydrodynamically when the separation distance is large, and they are essentially driven by electrostatic forces when the separation distance is of the order of two drop diameters. In what follows, we estimate the hydrodynamic and electrohydrodynamic forces and use the ratio of the forces to determine the nature of the dynamics of a pair of drops.

Assuming linear drag law for low Re cases discussed here, we can estimate the net hydrodynamic force on the drop as (cf. sec 4.9 in Batchelor (2000))

$$F_h \sim 2\pi a \mu_2 U_e \frac{2+3\mu_r}{1+\mu_r}(\mathbf{u}-\mathbf{v}) \ , \tag{4.6}$$

where $\mathbf{v}$ is the velocity of the center of mass of the drop, made dimensionless using U_e, and the magnitude of the ambient flow velocity $\mathbf{u} \sim (a/h)^2(R-Q)/(R+2)^2$ defines the dimensionless velocity of the ambient fluid. The factor $(R-Q)/(R+2)^2$ is the correction for the velocity scale, as discussed in the previous section. The electrostatic force between the drops can be estimated by considering the interactions between the dipoles defined by the sum of the net free and bound charges on the drop surface. For spherical drops in an electric field, the total charge in the northern hemisphere is given by

$$q_{net} = 3\pi\varepsilon_0 E_\infty a^2 \frac{(R-1)}{(R+2)} \ , \tag{4.7}$$

where ε_0 is the permittivity of the free space. An estimate for the corresponding electrostatic force between the drops (dipole-dipole interaction), placed at a center-to-center separation distance of h, can be obtained as

$$F_e \sim \frac{2q_{net}^2}{4\pi\varepsilon_2}\frac{a^2(a^2-3h^2)}{h^2(a^2-h^2)^2} \tag{4.8}$$

The above electrostatic force in the limit of large h results in E_∞^2/h^4 dependence as discussed in Baygents et al. (1998). The relative strengths of the electrostatic to hydrodynamic forces can be estimated from the following expression

$$\frac{F_e}{F_h} \sim \frac{9}{8}\left(\frac{\varepsilon_0}{\varepsilon_2}\right)^2 \frac{(R-1)^2}{(R-Q)}\left(\frac{1+\mu_r}{2+3\mu_r}\right)\frac{1-3(h/a)^2}{\left[1-(h/a)^2\right]^2} \tag{4.9}$$

Thus, from the above expression, we can observe that the key parameters which govern the relative velocity between the drops are the ratio of electric conductivities, R, the initial separation distance between the drops, h/a, the ratio of charge relaxation time $\tau_e^1/\tau_e^2 = Q/R$, and also the permittivity of the ambient fluid ε_2. The permittivity of the ambient fluid has a detrimental effect on the electrostatic interactions due to dielectric screening effects.

For the cases shown in Figures 4.5 and 4.6, $t_R/t_q \sim 0.42$ corresponding to a fast deformation of the drops in response to the electrostatic forces and $\tau_\mu/t_q \sim 39.68$ which corresponds to the time scale of migration of the drops. The order of this time scale is in good agreement with the observations from the simulations. For these cases, F_e/F_h, are 2.35 and 0.00036, thus clearly suggesting that electrostatic forces are dominant in the first case for $R = 6$ and $Q = 8$, whereas for $R = 1.04$ and $Q = 0.2$, hydrodynamic forces are dominant. Thus, the velocity of attraction is expected to be proportional to $1/h^4$ for the former case and $1/h^2$ for the latter. In Figure 4.8, we present the variation in the relative center-of-mass velocity with the separation distance between the drops on a log-log scale. As expected, the relative velocity between the drops varies as $1/h^4$ in approaching case as shown in Figure 4.8(a) and as $1/h^2$ for repelling drops as shown in Figure 4.8(b).

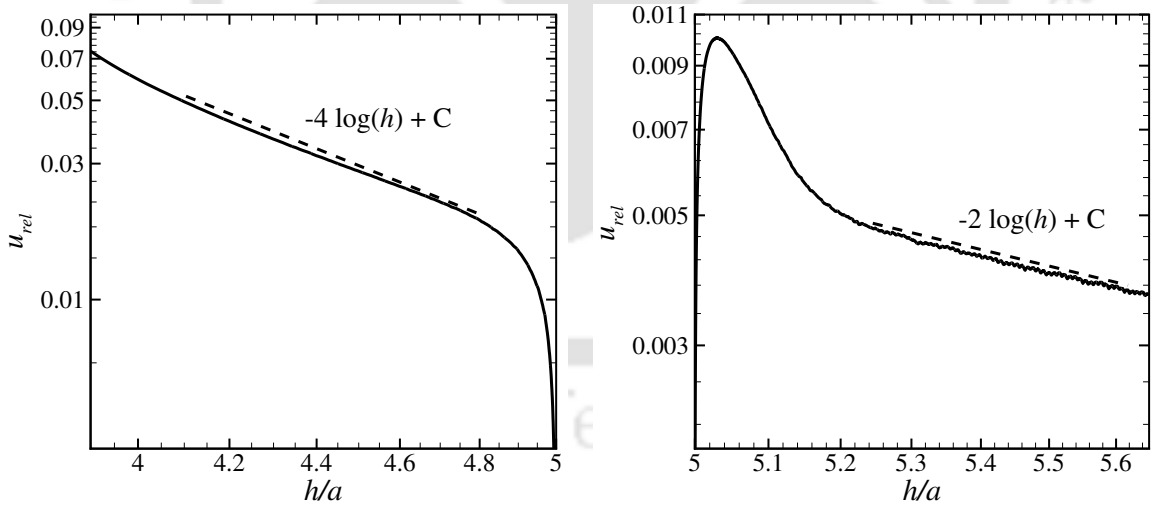

(a) Drops attract (b) Drops repel

Fig. 4.8 Velocity variation with respect to center-to-center distance between the drops for (a) $R = 6$ and $Q = 8$ and (b) $R = 1.04$ and $Q = 0.2$ at $Ca_E = 1.5$ and $Re = 0.10$.

Other possible interesting behavior is also observed for a particular set of parameters. For instance, we show that the drops may approach each other, come close, but not

coalesce and instead form a doublet as shown in Figure 4.9. For $R = 25$ and $Q = 2$, when the drops are initially at a separation of $h/a = 4$, we obtain $F_e/F_h \sim 4.71$ where the electrostatic forces are attractive, but the hydrodynamic forces are repulsive. Since electrostatic forces are stronger, the drops attract. However, the drainage of the film between the drops is delayed leading to the formation of a drop-drop doublet that is separated by a thin film of the ambient fluid as shown in the zoomed-in view in Figure 4.9. A low Re indicates a much stronger influence of electrostatic forces compared to hydrodynamic drag, which should have led to the coalescence of the drops. However, due to the nature of the hydrodynamic flow around the drops, a thin film of the ambient fluid is captured. To resolve the thin film, we used a more refined grid with $\Delta x_{min} = a/512$ for the current study. The gap at $t \sim 44$ is less, whereas a dimple forms at the center of the drops around $t \sim 50$ and remains stable at later times, as shown in the figure for $t \sim 70$. We note that once the flat film is fully formed at $t \sim 44$, further evolution leads to the formation of a dimple essentially due to the drop shape relaxation during which the thin film is pulled together, thus resulting in the formation of the dimple. The minimum thickness of the film towards the periphery is $0.0073a$, and in the dimple region, it is $0.061a$. The streamlines shown in the figure indicate that the ambient fluid is driven towards the thin film from the surface of the drops, essentially slowing the drainage of the film. In the simulations, these doublets do not change significantly with time, indicating a steady-state behavior in the timescales of

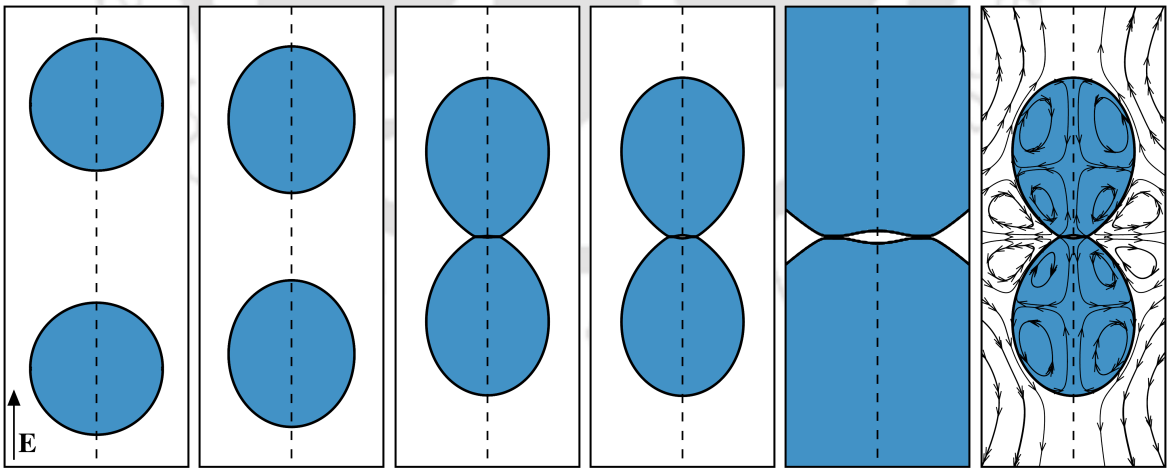

(a) $t = 0$ (b) $t = 30$ (c) $t = 44$ (d) $t = 70$ (e) $t = 70$ (f) $t = 70$

Fig. 4.9 Temporal evolution of a pair of non-coalescing drops for $R = 25$ and $Q = 2$ at $Ca_E = 0.2$ and $Re = 1$. Also shown are the zoomed-in views (representing the same area) and streamlines at $t = 70$.

interest. Since we are not incorporating the effect of van der Waals forces, the drainage time is dictated by the slow viscous time scale, which in this case, is further slowed down due to the ambient fluid flow toward the film. The dimple formation in the center is similar to those observed during the coalescence of bubbles or the impact of a drop on a flat surface. The above phenomenon of non-coalescence and formation of a drop-drop doublet is different from the non-coalescence phenomenon observed for charged droplets, where charged droplets initially approach each other, form a conical neck, exchange charge, and then repel each other (Anand et al., 2019; Aryafar and Kavehpour, 2007; Ristenpart et al., 2009; Sunder and Tomar, 2020). Although there is no direct mention of the above phenomenon in experimental observations, there is evidence in certain experiments, for example, see Figures 3 and 4(a) in Zimmermann and Vienken (1982), showing two vesicles forming doublets during cell-cell fusion in the presence of the electric field. Also, see Figure 5 in Holto et al. (2009) suggesting the formation of a chain of water droplets in oil and indicating that the droplets align with the electric field but do not coalesce despite being in the immediate neighborhood of each other. We note that the electric stability of the ambient medium will also play a role in determining the complete physics of interaction since electric field intensity between the drops is high, which can lead to an electric breakdown leading to a more complex phenomenon involving local heating as discussed in the case of particles in Arp and Mason (1977).

4.4.2 Interaction dynamics of double emulsion

In this section, we first simulate the deformation of a single compound drop, constituting a double emulsion in an externally applied electric field, and compare the results with Abbasi et al. (2017). A compound drop with a shell radius of a and an inner core of radius $a/3$ is suspended in a continuous medium, and an externally applied electric field acts along the horizontal direction. An axisymmetric computational domain of size $(16a \times 16a)$ is chosen with the compound drop at the center of the domain. An external electric field is applied such that the bottom boundary of the domain is considered at a higher potential and the top boundary is grounded as discussed earlier in Section 4.2.1. The deformation of the outer drop is similar to the one expected for single drops for low aspect ratios. For the inner drop, the deformation will depend on the reduced electric field intensity in the outer drop and the ratio of the permittivities and conductivities. However, for higher aspect ratios, some deviation is expected (see Abbasi et al. (2017)). The stability of a compound drop was investigated numerically

by Abbasi et al. (2017), where it was suggested that if $R < Q$, the compound drop is unstable and the inner drop would exit the outer drop, whereas if $R > Q$ the inner drop migrates to the center of the outer drop. Abbasi et al. (2017) also investigated the drop bursting due to excessive deformation of the inner drop, especially when the aspect ratio is large.

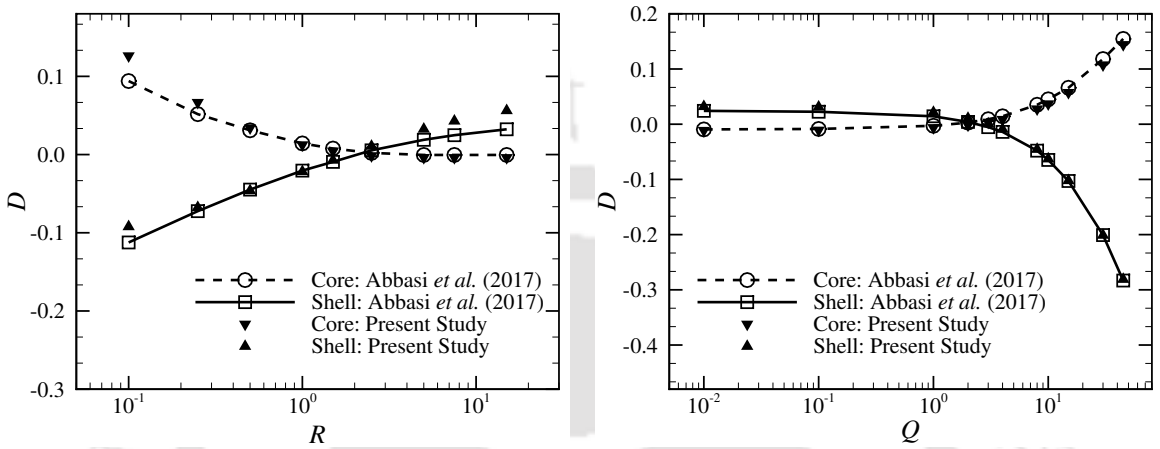

Fig. 4.10 Comparison of deformation of the core and the shell of a compound drop at $Ca_E = 0.2$ and $Re = 0.10$ for (a) $Q = 2$ and (b) $R = 2.5$.

In Figure 4.10(a), Q is kept constant at 2, and simulations are performed over a range of R varying from 0.1 to 20. When $R < Q$, we can observe that both interfaces experience large deformation. When $R > Q$, the magnitude of deformation at both interfaces decreases, which is depicted by the flattening of the curves. In Figure 4.10(b), R is kept constant at 2.5, and simulations are performed over a range of Q varying from 0.01 to 50. When $Q < R$ (for a sufficiently large R for a given Q as discussed in the case for an isolated single drop previously), the core shows oblate deformation, whereas the shell shows prolate deformation. For $Q > R$, the shell shows oblate deformation, and the core shows prolate deformation. We note that the inner and outer drop deformation obtained from the simulations presented in this study are in good agreement with the simulations of Abbasi et al. (2017). We plot the streamlines for two cases $R = 0.25, Q = 2$ and $R = 15, Q = 2$ as shown in Figure 4.11. In the case of $R < Q$, the flow in the ambient is from the poles to the equator, the same as the single drop. The shell has a flow circulation in a direction opposite to the ambient, while the core has the same circulation direction as the ambient. All sense of flow circulation reverses for $R > Q$.

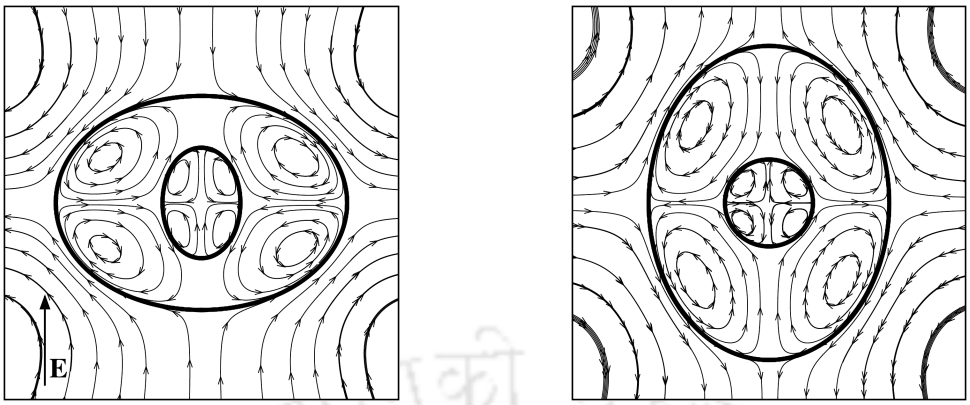

(a) $R = 0.25, Q = 2$ (b) $R = 15, Q = 2$

Fig. 4.11 Streamlines and variation in the shape of the core and shell for different conductivity and permittivity ratios. The other computation parameters are $Ca_E = 0.2$, and $Re = 0.10$.

Interactions between compound drops in a double emulsion can lead to various interesting configurations for different values of R and Q. To investigate this, we consider the setup as described in Section 4.2.1. The flow parameters used for the simulations are $Ca_E = 0.12$ and $Re = 1$. In Figure 4.12, for $R = 10$ and $Q = 25$ ($R < Q$), drops attract towards each other and so do the inner drops, leading to coalescence and the formation of a single bigger compound drop. The outer drop (shell) deforms prolately, whereas the deformation of the inner drop (core) is small. Electric field intensity inside the outer drop is $\sim 3E_\infty/(R+2)$ and thus for higher R is expected to reduce significantly. The effective Ca_E for the inner drops is thus much smaller due to reduced electric field intensity and increased capillary pressure because of the smaller radius. Therefore, inner drops deform significantly less. Interestingly, during coalescence, the inner drops approach faster than the centroid of the outer drop. Since the ratio of the electrostatic to hydrodynamic forces is $F_e/F_h \sim 1.02$, electrostatic forces dominate and drive the drops together and thus also drag the inner drops along. Subsequently, hydrodynamic forces on the inner drops drag the inner drop further toward the periphery. This suggests the possibility of the inner drop escaping the outer drop, as shown later for $R = 10$ and $Q = 30$. For $R = 3$ and $Q = 0.15$ ($R > Q$), shown in Figure 4.13, the outer drops move apart at a very slow rate, and therefore do not show much variation in terms of drop shapes with time in the duration investigated in this study. Further, since $R > Q$, the inner drops also remain at the center of the compound drop. This is in agreement with the observations from the simulations of Abbasi et al. (2017), where for $R < Q$, an off-centered inner drop is driven by a flow

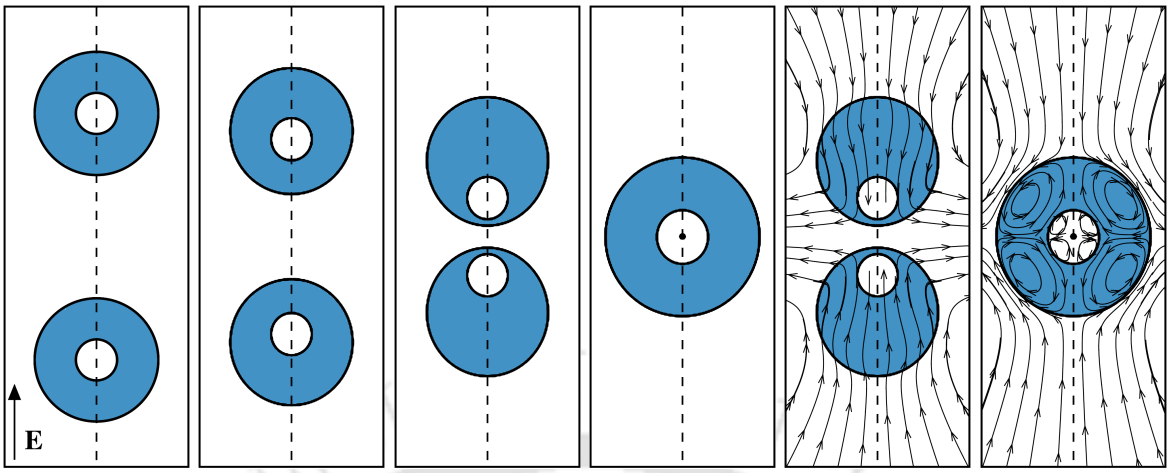

(a) $t = 0$ (b) $t = 17$ (c) $t = 29$ (d) $t = 40$ (e) $t = 29$ (f) $t = 40$

Fig. 4.12 Drop deformation and translation at different time instances for $R = 10$ and $Q = 25$ using the flow parameters $Ca_E = 0.12$ and $Re = 1$. We also plot the flow patterns in and around the core and shell at $t = 29$ and $t = 40$.

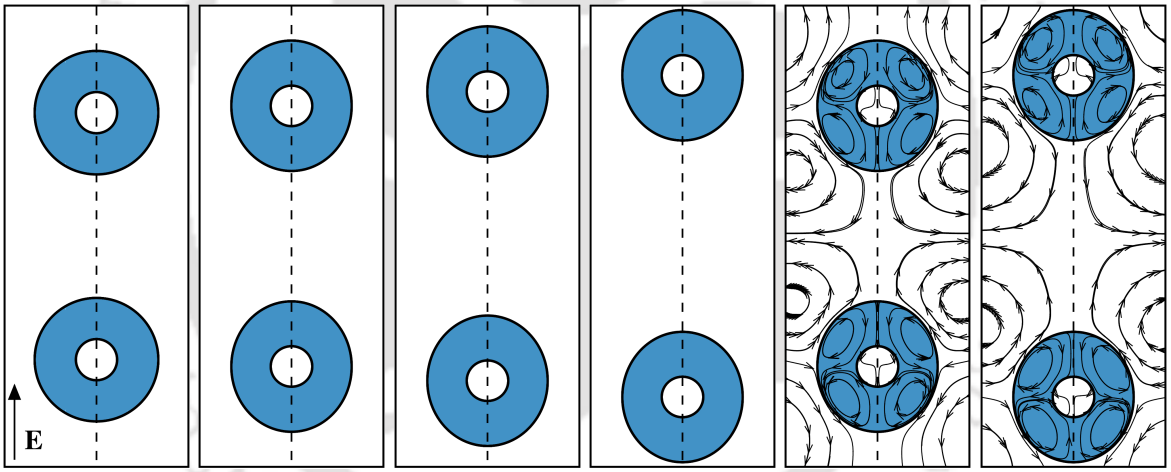

(a) $t = 0$ (b) $t = 30$ (c) $t = 100$ (d) $t = 200$ (e) $t = 30$ (f) $t = 200$

Fig. 4.13 Drop deformation and translation at different time instances for $R = 3$ and $Q = 0.15$ using the flow parameters $Ca_E = 0.12$ and $Re = 1$. We also plot the flow patterns in and around the core and shell at $t = 30$ and $t = 200$.

in the outer drop from the center towards the pole, and the inner drop is ejected out of the outer drop. On the other hand, if the flow generated in the outer drop is such that the flow is from the poles towards the center along the center-line of the drop (as observed for $R > Q$), the inner drop would be pushed back to the center of the outer drop. Figure 4.14 shows the variation in the relative velocity of the compound drops with the separation distance. Oscillations in the relative velocity of the outer drop as

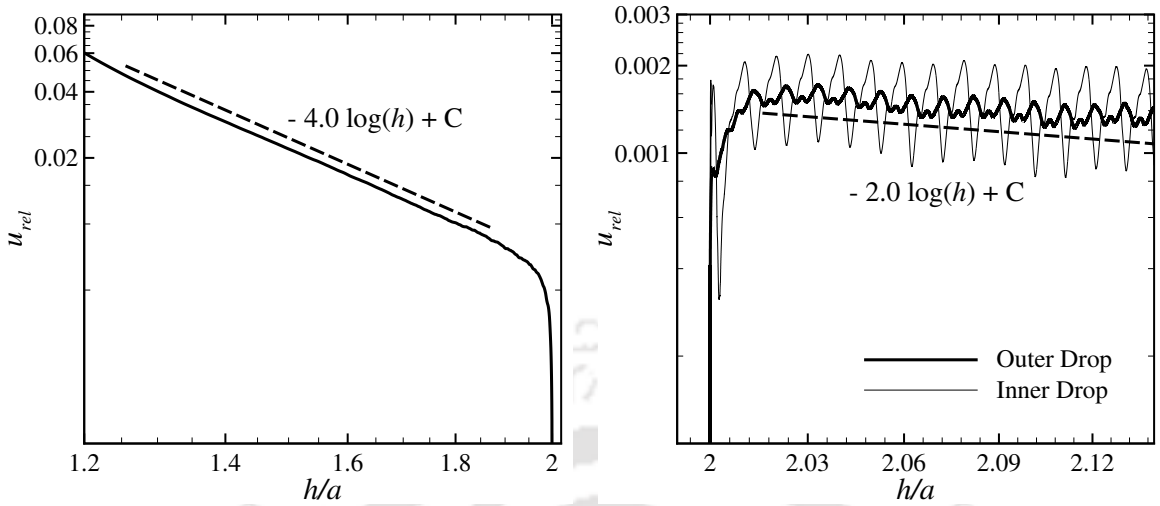

(a) Drops attract (b) Drops repel

Fig. 4.14 Velocity variation with respect to center-to-center distance between the drops for (a) $R = 10$ and $Q = 25$ and (b) $R = 3$ and $Q = 0.15$ at $Ca_E = 0.12$ and $Re = 1$. The motion of the inner core drop is also depicted.

well as for the inner drop are observed in the repulsion case, as shown in figure 4.14(b). Since the velocities are relatively small, the oscillations are more prominently visible in the repulsion case. Since F_e/F_h for $R = 10$ and $Q = 25$ is 1.02 a scaling of $1/h^4$ is observed for the approach velocity of the drops (see Figure 4.14(a)), whereas for $R = 3$ and $Q = 0.15$, $F_e/F_h \sim 0.26$, drops repel each other, governed essentially by the hydrodynamic forces resulting in a relative velocity that decreases as $1/h^2$.

For $R = 1.5$ and $Q = 10$, as shown in Figure 4.15, the inner drops escape the compound drops from the rear ends, as the two compound drops approach each other. Whereas, for $R = 10$ and $Q = 30$, the inner drops are released from the approaching ends of the two compound drops before they coalesce as depicted in Figure 4.16, thus resulting in the breakup of the double emulsion into a single emulsion which as expected for $R < Q$ would result in an unstable emulsion in the presence of an electric field. For $R = 1.5$ and $Q = 10$, $F_e/F_h \sim 0.0056$, whereas for $R = 10$ and $Q = 30$, $F_e/F_h \sim 0.76$. Therefore, in the former case, electrostatic forces are much weaker compared to the hydrodynamic forces, and the small inertial lag of the inner drop leads to a biased ejection of the inner drop from the portion of the periphery of the drop that faces away from the other compound drop. On the other hand, for $R = 10$ and $Q = 30$, electrostatic forces drive the drops together initially. However, they are not sufficiently stronger as was the case for $R = 10$ and $Q = 25$, and therefore inner drops eject from

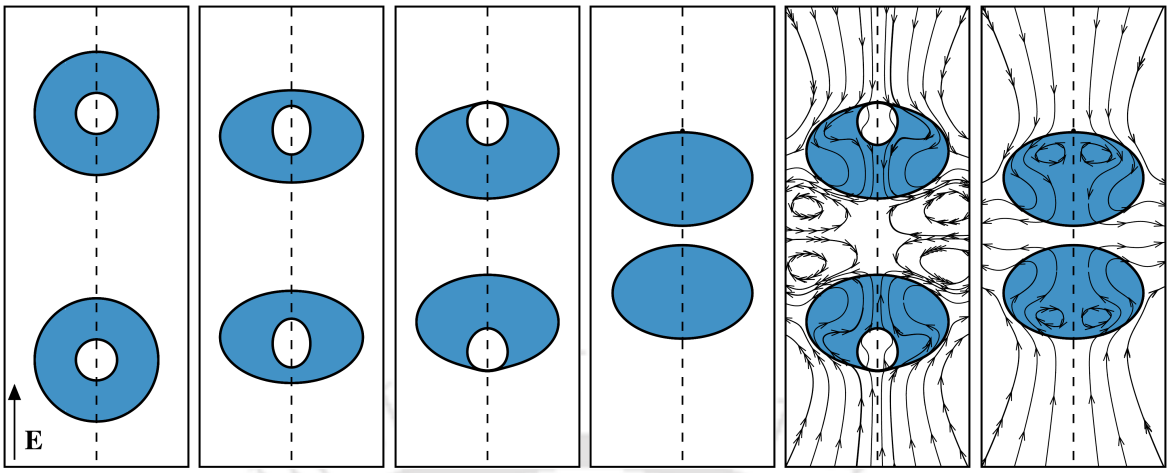

(a) $t = 0$ (b) $t = 10$ (c) $t = 14$ (d) $t = 20$ (e) $t = 14$ (f) $t = 20$

Fig. 4.15 Drop deformation and translation at different time instances for $R = 1.5$ and $Q = 10$ using the flow parameters $Ca_E = 0.12$ and $Re = 1$. We also plot the flow patterns in and around the core and shell at $t = 14$ and $t = 20$.

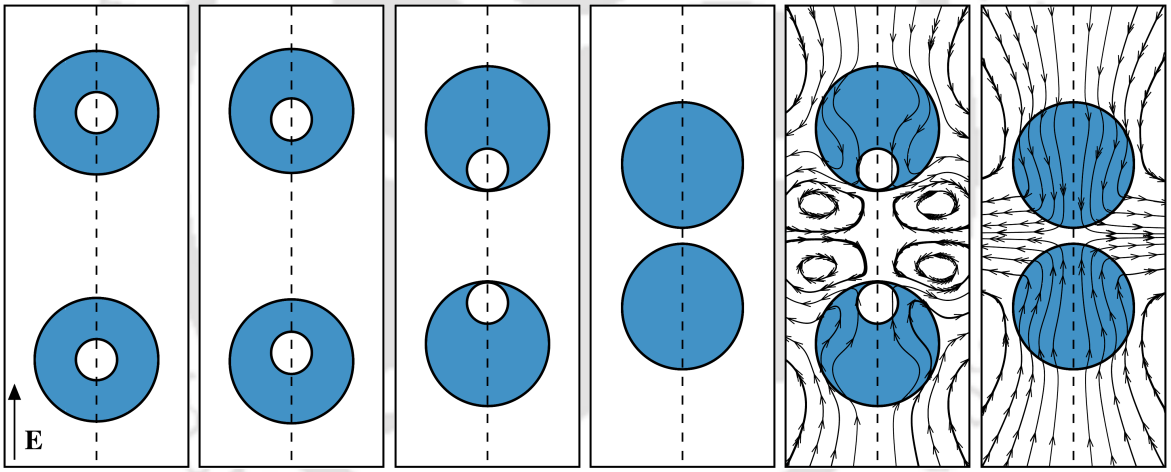

(a) $t = 0$ (b) $t = 20$ (c) $t = 34$ (d) $t = 50$ (e) $t = 34$ (f) $t = 50$

Fig. 4.16 Drop deformation and translation at different time instances for $R = 10$ and $Q = 30$ using the flow parameters $Ca_E = 0.12$ and $Re = 1$. We also plot the flow patterns in and around the core and shell at $t = 34$ and $t = 50$.

the portion of the outer drops facing each other. We note that the hydrodynamic response of the drops can be weakened by reducing Re leading to a possible entrapment of the inner drops even for the case with $R = 10$ and $Q = 30$.

Finally, we present three other cases showing interesting dynamics of the compound drops. In the first one, the outer drops approach each other but do not coalesce but form a drop-drop doublet, as shown in Figure 4.17 for $R = 20$ and $Q = 1$. As discussed

earlier for the single drops with the same electric properties, this interesting physics is due to the initial strong electrostatic attraction and subsequent delay in the drainage of the thin film between the two drops due to the nature of the flow around the drops as shown by the streamlines at $t = 50$. Since electrostatic forces are much stronger than the hydrodynamic forces, as suggested by $F_e/F_h \sim 3.57$, the drops are initially driven together. The flow around the drops is developed by the motion of the drops as indicated by the streamlines at $t = 30$. However, the flow lines reverse after the development of the flow generated by the tangential electrical stresses as shown by the streamlines at $t = 50$. However, for $R = 30$ and $Q = 10$, $F_e/F_h \sim 7.91$, indicating an even stronger electric field that drives the drops to approach each other and eventually coalesce as seen in Figure 4.18. These cases clearly indicate that the simple rule depending on the sign of $(R - Q)$ for determining the interactions between the drops is insufficient, and the relative strengths of electrostatic and hydrodynamic forces, along with inertial effects governed by Re, need to be accounted for. Interestingly, the inner drops for $R = 30$ and $Q = 10$ do not coalesce (even when simulations are run up to $t \sim 400$). For $R = 7$ and $Q = 10$ shown in Figure 4.19, the inner drops form a configuration similar to that in Figure 4.18 but eventually the inner drops repel (since $R < Q$) and are ejected out.

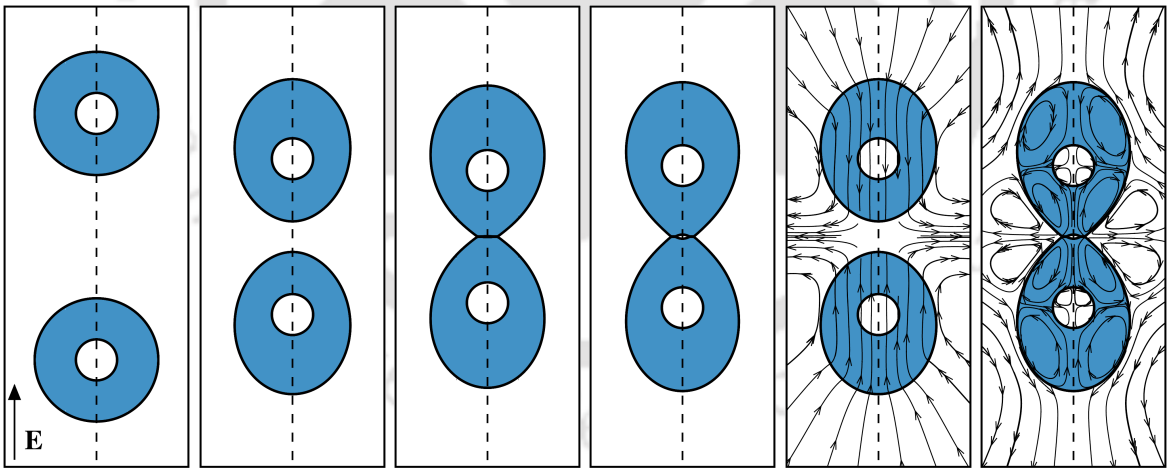

(a) $t = 0$ (b) $t = 30$ (c) $t = 32$ (d) $t = 50$ (e) $t = 30$ (f) $t = 50$

Fig. 4.17 Drop deformation and translation at different time instances for $R = 20$ and $Q = 1$ using the flow parameters $Ca_E = 0.12$ and $Re = 1$. We also plot the flow patterns in and around the core and shell at $t = 30$ and $t = 50$.

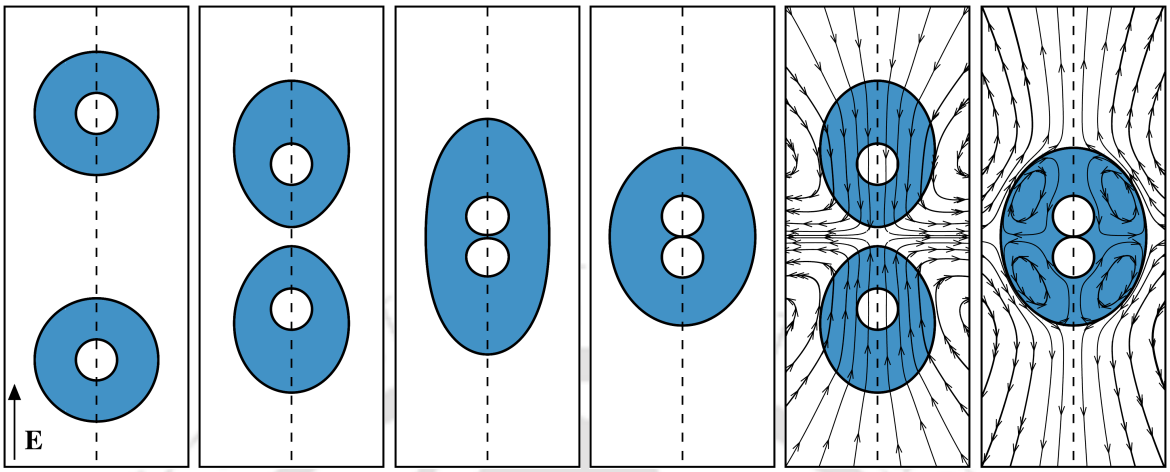

(a) $t = 0$ (b) $t = 24$ (c) $t = 27$ (d) $t = 60$ (e) $t = 24$ (f) $t = 60$

Fig. 4.18 Drop deformation and translation at different time instances for $R = 30$ and $Q = 10$ using the flow parameters $Ca_E = 0.12$ and $Re = 1$. We also plot the flow patterns in and around the core and shell at $t = 24$ and $t = 60$.

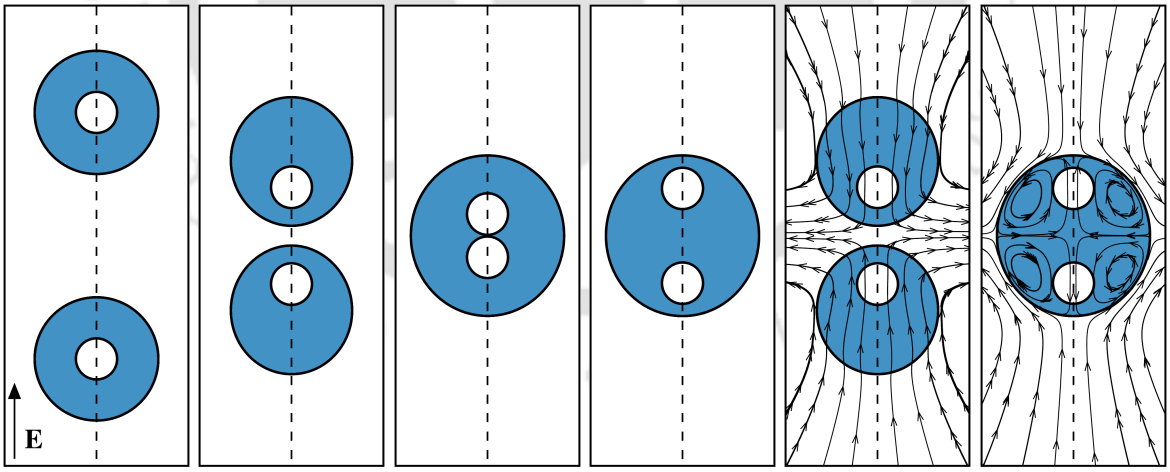

(a) $t = 0$ (b) $t = 50$ (c) $t = 60$ (d) $t = 100$ (e) $t = 50$ (f) $t = 100$

Fig. 4.19 Drop deformation and translation at different time instances for $R = 7$ and $Q = 10$ using the flow parameters $Ca_E = 0.12$ and $Re = 1$. We also plot the flow patterns in and around the core and shell at $t = 50$ and $t = 100$.

4.5 Summary

In the present chapter, we have numerically investigated the interaction dynamics of a pair of drops (single and compound) in a uniform electric field. A leaky dielectric model is utilized for this study, with the core and the ambient phase being the same and the shell of the compound drop being different. We note that the stability of a compound drop as well the relative motion between a pair of drops, depends essentially on the charge relaxation time constant ratio of the ambient and the outer shell of the compound drop (τ_e^1/τ_e^2).The apriori expectation of the stability of an emulsion in an electric field would require consideration of the relative time scales of electrostatic attraction, charge relaxation, and flow time scale. Moreover, the relative strength of the electrostatic and hydrodynamic forces, given by the ratio F_e/F_h in Equation (4.9), also determines the interaction dynamics of the drops. We believe this study would motivate more experiments in regimes that show intriguing dynamics of the drops, such as the formation of a drop-drop doublet.

Chapter 5

Noncoalescence in leaky-dielectric emulsions

The interaction dynamics of a pair of freely suspended drops in a uniform electric field are investigated using a computational framework. The system consists of a pair of leaky-dielectric drops in another leaky-dielectric medium. A finite Reynolds number has been considered for this study. The applied electric field induces a dipole in the drops, leading to various interaction dynamics. This chapter is a continuation of the previous chapter investigating the non-coalescence phenomena. The chapter starts with an overview of the previous investigations performed for drop pairs under electric field (§ 5.1). Then, the computational model used to study interaction dynamics is described (§ 5.2). Next, the numerical model is validated with earlier studies (§ 5.3). The effects of considering a finite Reynolds number are subsequently explored, and a regime map is drawn to demarcate the different interacting phenomena (§ 5.4). The chapter then concludes with a summary of the outcomes (§ 5.5).

5.1 Introduction

Separation of emulsified mixtures into constituent components, such as that of oil and water, is desired in petroleum and other chemical and food industries (Gañán-Calvo et al., 2018; Priti Sinha et al., 2020). Demulsification using electrocoalescence is the preferred method compared to other mechanical, thermal, or chemical means (Dezhi et al., 1999; Eow et al., 2001; Klasson et al., 2005; Wu et al., 2003).

The classical study by Taylor introduced the leaky-dielectric model to investigate fluids having small but finite electrical conductivity (Taylor, 1966). Although the study

of an isolated drop in an external electric field is well understood, several features of the collective dynamics of drops in an electric field, such as drop-chain formation, remain unexplained (Brazier-Smith, 1971; Sozou, 1975). Unlike the symmetrical state of an isolated drop, an asymmetrical electric field is produced for a pair of drops due to the presence of the neighboring drop. This is the well-known phenomenon of dielectrophoresis, in which the intensity of the electric field at one side of a drop is stronger than the other side (Pohl and Crane, 1971). For small separation distance, Atten (1993), assuming droplets to behave as point dipoles, showed that for coalescence, there exists a critical separation distance and a critical magnitude of the applied electrical field. Depending upon the electrical properties of the constituents of the emulsions and the nature of the flow of current through the emulsion, various possible scenarios can occur. If the ambient phase is a poor conductor of electricity compared to the drop phase, such as in water-in-oil systems, electrocoalescence, partial coalescence, and non-coalescence occur depending upon the strength of the applied electric field (Anand et al., 2020; Bird et al., 2009; Huang et al., 2020). Bird et al. (2009) showed that drops do not coalesce even after contact above a critical electric capillary number, and many move apart. Non-coalescence in systems where droplets are charged has been well understood (Bird et al., 2009). However, systems where droplets are initially uncharged, have been shown to form chains. Droplet chain formation in emulsions is a severe deterrent in the de-emulsification process (Mhatre et al., 2015a; Mohammed et al., 1993; Pearce, 1954). Although several strategies have been proposed to inhibit chain formation, the mechanism of chain formation is still not known (Bailes et al., 2000; Chen et al., 1994; Midtgård, 2012).

However, chain formation has also been observed in leaky-dielectric systems (Melcher and Taylor, 1969; Saville, 1997) where both phases have electric conductivity that does not defer by more than an order (Mhatre et al., 2015a). In these systems where the current can flow through the bulk, the above non-coalescence of uncharged droplets in the presence of an electric field is not expected. In such systems, tangential electric stresses generate sufficient flow in the continuous phase of the emulsion for the droplets to hydrodynamically repel, where electric forces tend to always make the droplets attract (Baygents et al., 1998; Sorgentone et al., 2021; Vlahovska, 2019). In this chapter, we show that drop pair systems in certain regimes of electrical conductivity and permittivity ratios show non-coalescence. By performing detailed numerical electrohydrodynamics simulations for drop pairs, we show the formation of a stable thin film that prevents coalescence.

5.2 Formulation

5.2.1 Computational domain

An axisymmetric domain, as shown in Figure 5.1, is considered for the present study, with the axis of symmetry lying along the z-axis. We study the interaction dynamics of a pair of leaky-dielectric drops suspended in a leaky-dielectric ambient fluid under the influence of an externally applied electric field. The domain spans $16a$ along axial and radial directions, where a is the undeformed spherical drop radius. The drops are initially placed with a center-to-center distance of $h = 4a$. Fluid properties such as density, viscosity, electrical conductivity, and electrical permittivity are represented by ρ, μ, σ, and ε, respectively. The subscripts 1 and 2 are used to distinguish the drop phase and the ambient phase. The fluids are Newtonian, and the interfacial tension $\gamma_{12} = \gamma$ between the drop and ambient is assumed to be uniform. The drops are neutrally buoyant with densities $\rho_1 = \rho_2$. The computational domain is large enough to avoid the effect of the boundary on the dynamics of the drops.

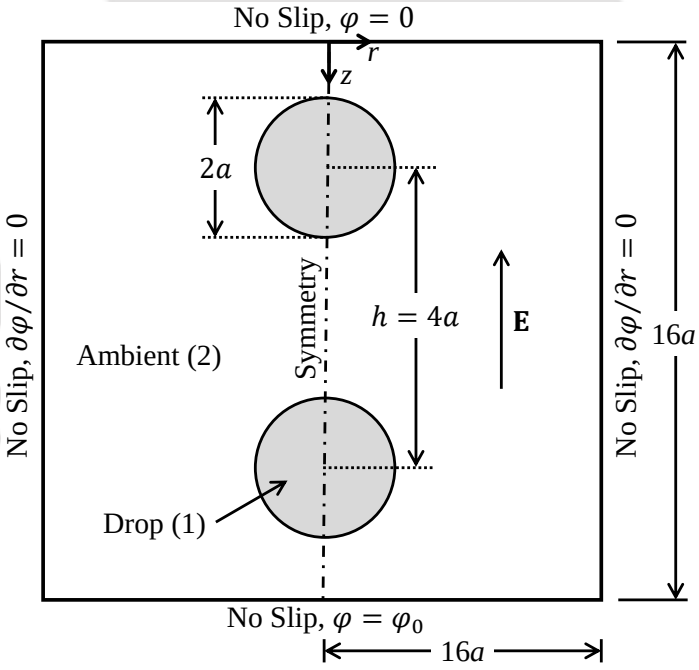

Fig. 5.1 Schematic diagram (not to scale) showing a pair of drops interacting in the presence of an externally applied electric field in an axisymmetric cylindrical coordinate system (r, z). The radius of the drops are a and are placed at a separation of $h = 4a$. Electric field ($\mathbf{E}$) is applied along negative z axis. The size of the domain is $16a \times 16a$.

5.2.2 Solution methodology

We solve the full Navier-Stokes equations coupled with electric field equations using the leaky-dielectric model proposed by Melcher and Taylor (1969). The two-phase system is governed by the modified incompressible Navier-Stokes equations using the one-fluid formulation.

$$\boldsymbol{\nabla}\cdot\mathbf{u}=0\ ,$$

$$\rho\left[\frac{\partial\mathbf{u}}{\partial t}+\mathbf{u}\cdot\boldsymbol{\nabla}\mathbf{u}\right]=-\boldsymbol{\nabla}p+\boldsymbol{\nabla}\cdot(2\mu\mathbb{D})+\boldsymbol{\nabla}\cdot\varepsilon\left(\mathbf{EE}-\frac{E^2}{2}\mathbf{I}\right)+\gamma\kappa\delta_s\hat{\mathbf{n}}\ .$$

An external electric field ($\mathbf{E}$) is applied along the axial direction. It is imposed by applying electric potential φ using the boundary condition on the bottom boundary $(r, z = 16a)$

$$\varphi=\varphi_0\ ,\qquad u=v=0\ . \tag{5.1}$$

The top boundary is electrically grounded using the boundary condition $(r, z = 0)$

$$\varphi=0\ ,\qquad u=v=0\ . \tag{5.2}$$

Neumann boundary condition for the electric potential is imposed on the right boundary $(r = 16a, z)$

$$\frac{\partial\varphi}{\partial r}=0\ ,\qquad u=v=0\ . \tag{5.3}$$

Symmetry boundary conditions are imposed on the axis of symmetry for the velocity field and the electric potential $(r = 0, z)$

$$\frac{\partial\varphi}{\partial r}=0\ ,\qquad u=0\ ,\qquad \frac{\partial v}{\partial r}=0\ . \tag{5.4}$$

No-slip and impervious velocity conditions are imposed on the other boundaries. The details of the governing equations are defined in Section 2.2.1. The numerical simulations are carried out using the Basilisk solver described extensively in Section 2.2.2. This solver has been used by many researchers successfully in the past for solving various electrohydrodynamic flow problems (Behera et al., 2019; Borthakur et al., 2021; Ghasemi et al., 2018).

5.2.3 Dimensionless parameters

The governing equations, along with the boundary conditions, are made dimensionless using the following scaling parameters: undeformed spherical drop radius a is taken as the characteristic length scale, U_e is taken as the characteristic velocity scale based on the flow generated by the electric forces, and E_∞ is chosen as the characteristic scale for the electric field. The scaling for the flow field generated due to the electric forces can be obtained by balancing viscous stresses with Maxwell stresses at the interface and is given as $U_e \sim a\varepsilon_2 E_\infty^2/\mu_2$. The pressure term is scaled using $\rho_2 U_e^2$. All the fluid properties are scaled using the respective properties of the ambient phase. We obtain the following dimensionless parameters using the above scaling:

$$Re = \frac{\rho_m \varepsilon_m a^2 E_\infty^2}{\mu_m^2}\,, \qquad Ca_E = \frac{\varepsilon_m a E_\infty^2}{\gamma}\,, \qquad Re_E = \frac{\varepsilon_m^2 E_\infty^2}{\mu_m \sigma_m}\,. \tag{5.5}$$

Reynolds number Re represents the ratio of the inertia forces to the viscous forces, and the electric capillary number Ca_E represents the ratio of the electrostatic forces to the surface tension forces. The term Re_E is the electric Reynolds number which denotes the ratio of the charging time scale to the flow time scale. For leaky-dielectric drops, typically $Re_E \ll 1$, which signifies that charge accumulates instantaneously at the interface. The dimensionless parameters for the fluid properties are the electrical conductivity ratio $R = \sigma_1/\sigma_2$, the electric permittivity ratio $Q = \varepsilon_1/\varepsilon_2$, the viscosity ratio $\mu_r = \mu_1/\mu_2$, and the density ratio $\rho_r = \rho_1/\rho_2$. We have considered $\mu_r = 1$ and $\rho_r = 1$ in the present study. A detailed derivation of the dimensionless equations is described in Appendix B.

5.3 Validation

5.3.1 Comparison with literature

Mhatre et al. (2015a) investigated the dynamics of suspended drop pairs using experiments, analytical theory, and numerical calculations (in particular, they used the boundary element method). We validate the present computational model with the experimental work of Mhatre et al. (2015a). They considered two systems: (i) a pair of perfect conductor drops in a perfect dielectric fluid and (ii) a pair of leaky-dielectric drops in another leaky-dielectric fluid. Since our present study focuses on a pair of leaky-dielectric drops suspended in another leaky-dielectric fluid, we compare our

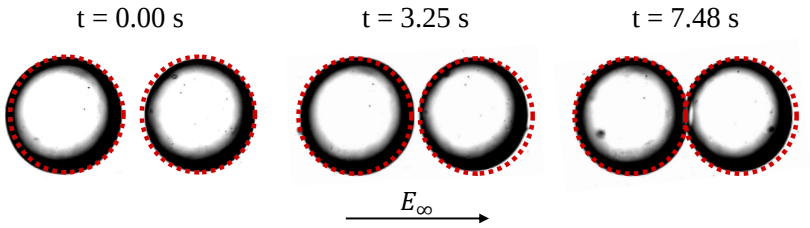

Fig. 5.2 Comparison of the interaction of a silicone oil drop pair in castor oil under uniform DC electric field of $E_\infty = 2.22$ kV/cm. The radius of the drop is $a = 270\mu m$. The experimental result is obtained from Figure 14 of Mhatre et al. (2015a). The red dotted lines are the results from the present solver.

numerical results with their respective experimental studies. Figure 5.2 compares the interaction dynamics of a silicone oil drop pair suspended in castor oil. The initial separation between the drops was $h/a = 2.34$, and the applied DC uniform electric field strength was $E_\infty = 2.22$ kV/cm. The corresponding electric capillary number was $Ca_E = 0.138$. The other fluid properties considered were $\mu_r = 0.44$, $R = 0.02$, and $Q = 0.56$. The drops come close as this system has $R < Q$. As evident from the Figure 5.2, an excellent qualitative match is obtained for this present numerical study with their experimental work.

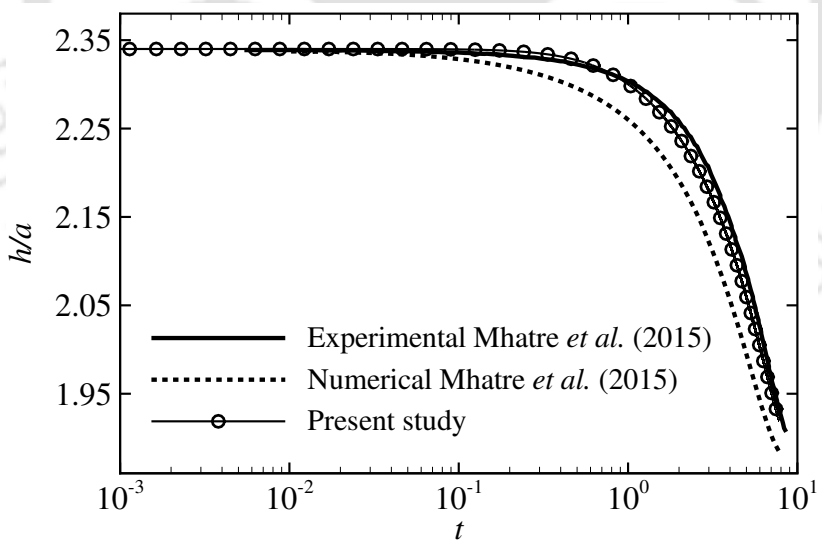

Fig. 5.3 Comparison of the interaction of a silicone oil drop pair in castor oil under uniform DC electric field of $E_\infty = 2.22$ kV/cm. The radius of the drop is $a = 270\mu m$. The experimental result is obtained from Figure 14 of Mhatre et al. (2015a).

Mhatre et al. (2015a) also plotted the kinetics of the approach for the silicone-castor oil system and compared their experimental work with their numerical work using

the boundary element method. We also compared this kinetics of the approach of the drops as shown in Figure 5.3. Our present numerical study agrees well with their experimental work. We can also observe that our computational model predicts the drop kinetics better than their numerical study.

5.3.2 Grid independence studies

In order to optimize the computational cost, an adaptive mesh refinement approach is employed in the present study. The grid is adapted based on the volume fraction gradient to have a very fine mesh near the interface and a relatively coarser mesh elsewhere. A grid convergence test is performed to ensure the results are independent of the grid resolution. The entire interface is resolved using Δx_{min}, and the grid is progressively coarsened ($l = 6$) away from the drop. The operating parameters used for the test are $R = 10$, $Q = 20$, $Re = 1$, $Ca_E = 0.12$, $h/a = 4$, $\mu_r = 1$ and $\rho_r = 1$. The relative velocity of the two drops (u_{rel}) is plotted against the separation between the drops (h/a). It can be observed from the inset in Figure 5.4 that the curves corresponding to $a/\Delta x_{min} = 256$ ($l = 12$) and 512 ($l = 13$) are very close, and further grid refinement has a negligible effect. The maximum difference was 0.36%. Hence, a grid refinement level of 12 has been used for the rest of the study.

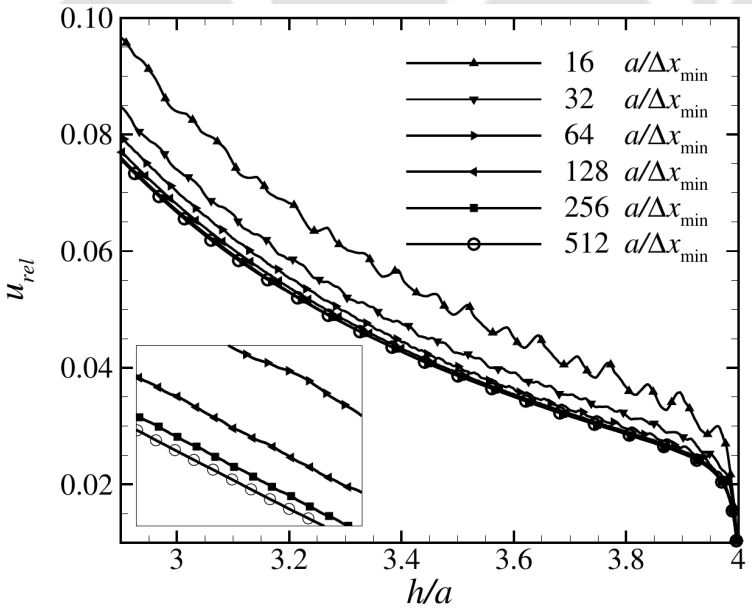

Fig. 5.4 Plot of relative velocity and the separation between the drops at six different grid refinements. The parameters considered for the computations are $R = 10$, $Q = 20$, $Re = 1$, $Ca_E = 0.12$, $h/a = 4$, $\mu_r = 1$ and $\rho_r = 1$.

5.4 Results and discussion

The interaction dynamics between a leaky-dielectric drop pair suspended in another leaky-dielectric medium, when subjected to an external electric field, is guided by two mechanisms: (i) a far-field dipole, developed by an induced electric field which always tends to drive the drops closer, and (ii) hydrodynamic flow which can make the drops come closer or move apart based on the flow circulation pattern. For $R < Q$, the bulk flow occurs from the poles to the equator, and the drops come closer. While for $R > Q$, the sense of flow is reversed, i.e., the bulk of the fluid moves from the equator to the poles, and the drops move apart. Based on creeping flow conditions and far-field argument, Baygents et al. (1998) proposed a map of the expected dynamics for a pair of drops as shown in Figure 5.5. A zero deformation curve represented by $\mu_r = 1$ distinguishes the condition for prolate or oblate drop shape, while the $R = Q$ line separates the electrically driven circulation patterns that are attractive from those that are repulsive. Baygents et al. (1998) characterized the conditions leading to oblate-shaped drops that came closer, prolate-shaped drops that came closer, and prolate-shaped drops that moved apart. However, they also mentioned that only some qualitative drop pair interaction features could be predicated on their map. In

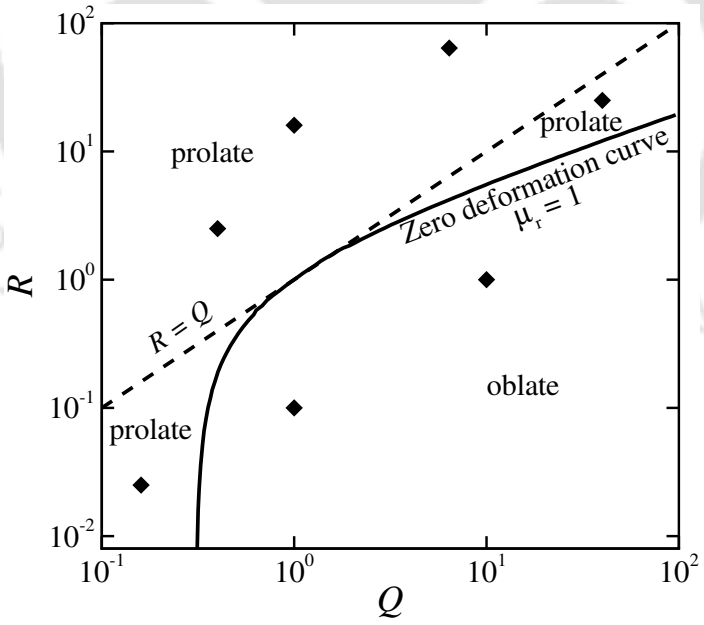

Fig. 5.5 Phase diagram of the expected shape response and the circulation patterns as a function of the conductivity (R) and permittivity (Q) ratios. The zero deformation curve and the $R = Q$ line delineate three combinations of deformation and circulation. The marked points are the (R, Q) parameters presented in this study.

the previous chapter, we gave an estimate of the ratio of electrostatic forces (F_e) and hydrodynamic forces (F_h) to determine the nature of the interaction dynamics of a pair of drops. The expression was derived based on a dipole-dipole interaction and linear drag law as

$$\zeta = \frac{F_e}{F_h} \sim \frac{9}{8}\left(\frac{\varepsilon_0}{\varepsilon_2}\right)^2 \frac{(R-1)^2}{(R-Q)}\left(\frac{1+\mu_r}{2+3\mu_r}\right)\frac{1-3(h/a)^2}{\left[1-(h/a)^2\right]^2} \tag{5.6}$$

We perform systematic simulations using the full Navier-Stokes equations to understand the interaction dynamics of a pair of leaky-dielectric drops. We have considered a finite Reynolds number of $Re = 1$ in our simulations, and the value of the electric Reynolds number is taken as $Re_E = 0.01$ for neglecting charge convection. Since we study only the effect of conductivity and permittivity ratios, other fluid properties are kept constant throughout the study. The initial center-to-center drop distance is kept as $h/a = 4$, the electric capillary number is $Ca_E = 0.12$, the viscosity ratio is $\mu_r = 1$, and the density ratio is $\rho_r = 1$. We carried out several simulations to produce a regime map. We do not show the results for all the simulations individually for brevity. Instead, we have present seven leaky-dielectric systems having (R, Q) as represented in Figure 5.5.

5.4.1 Interaction between leaky-dielectric drops

Figure 5.6 shows the drop translation and the associated hydrodynamic flow phenomena for the system $(R, Q) = (2.5, 0.4)$. Due to the nature of the electric stresses, the initial spherical drops deform into a prolate shape. Here $R > Q$ and the bulk hydrodynamic flow is from the equator to the poles. The electrostatic forces always tend to bring the drops closer. However, the flow patterns tend to move the drops apart. The value of ζ for this system is around 0.2, implying that the hydrodynamic forces overcome the electrostatic forces and make the drops move apart. The flow dynamics for both inner and outer regions around the drop can be seen clearly in Figure 5.6(f). Inside the drop, two asymmetric vortex pairs are formed. The relative strengths of the hydrodynamic forces by these vortex pairs suggest that a net force makes the drops move apart. Together with the outer flow circulations, these vortex pairs incessantly make the drops move apart.

Figure 5.7 shows the drop translation and the associated hydrodynamic flow phenomena for the system $(R, Q) = (16, 1)$. Due to the nature of the electric stresses,

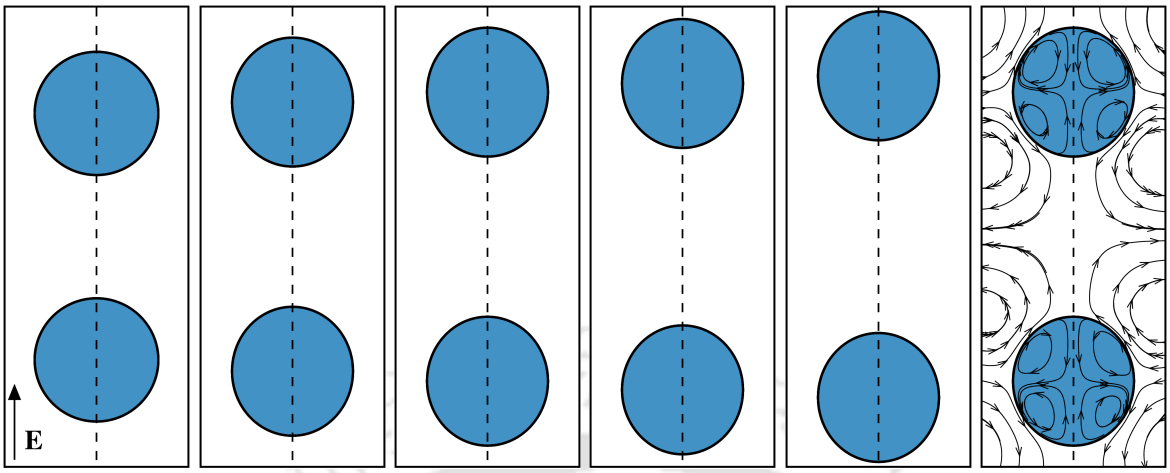

(a) $t = 0$ (b) $t = 50$ (c) $t = 100$ (d) $t = 150$ (e) $t = 200$ (f) $t = 100$

Fig. 5.6 Drop deformation and translation at different time instances for $R = 2.5$ and $Q = 0.4$ using the flow parameters $Ca_E = 0.12$ and $Re = 1$. We also plot the flow patterns at $t = 100$.

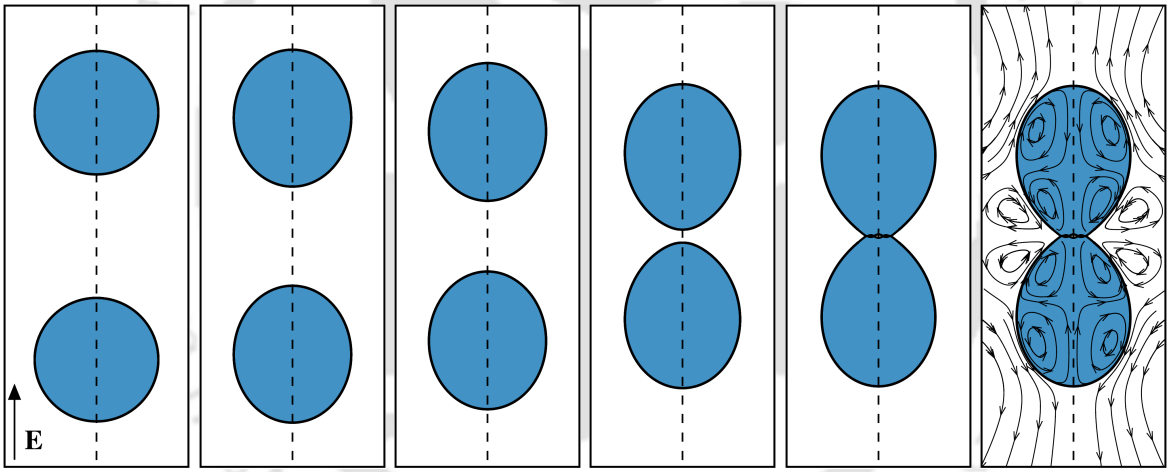

(a) $t = 0$ (b) $t = 10$ (c) $t = 25$ (d) $t = 36$ (e) $t = 50$ (f) $t = 50$

Fig. 5.7 Drop deformation and translation at different time instances for $R = 16$ and $Q = 1$ using the flow parameters $Ca_E = 0.12$ and $Re = 1$. We also plot the flow patterns at $t = 50$.

the initial spherical drops deform into a prolate shape. Here $R > Q$ and the bulk hydrodynamic flow is from the equator to the poles. The value of ζ for this system is around 2.82, implying that the hydrodynamic forces are weaker than the electrostatic forces. The drops respond to the dipole forces and come closer. As the drops translate toward each other, they eventually come very close, creating a thin film between them. After the thin film formation, the flow dynamics for both inner and outer regions

around the drop can be seen clearly in Figure 5.7(f). Inside the drop, two asymmetric vortex pairs are formed. The relative strengths of the hydrodynamic forces by these vortex pairs suggest a net force that makes the drops move apart. Nevertheless, the electrostatic forces keep them together. This balance between the forces makes the thin film stable, and the system achieves a steady state.

Figure 5.8 shows the drop translation and the associated hydrodynamic flow phenomena for the system $(R, Q) = (64.0, 6.4)$. Due to the nature of the electric stresses, the initial spherical drops deform into a prolate shape. Here $R > Q$ and the bulk hydrodynamic flow is from the equator to the poles. The value of ζ for this system is around 12.95, implying a weaker hydrodynamic force than the electrostatic force. Responding to the strong dipole interaction, the drop comes close and finally coalesces. Just after coalescence, the charges redistribute along the interface. The high charges at the interface create significant electric stresses, and the drop gets stretched. The new flow field makes the drops move apart, as shown in Figure 5.8(f), and the system eventually disintegrates into smaller drops.

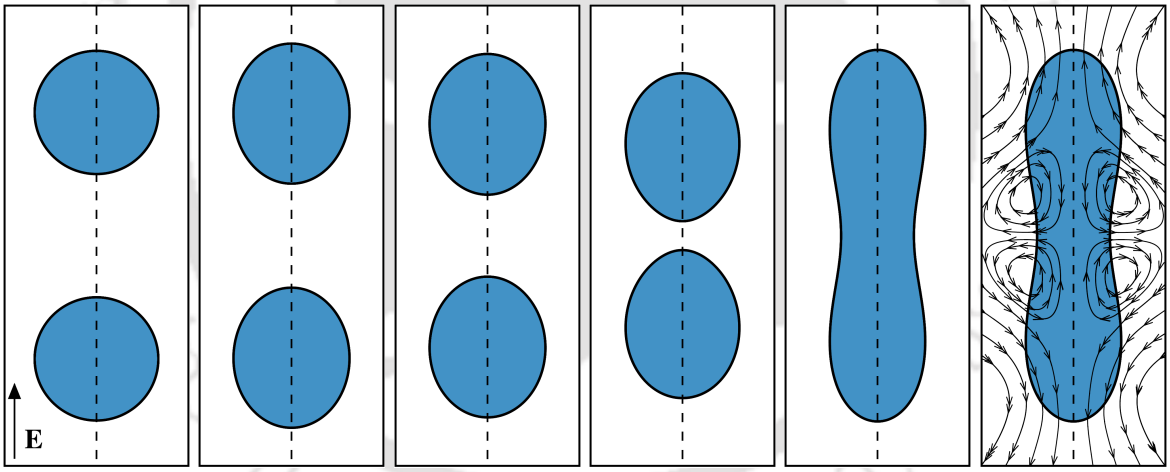

(a) $t = 0$ (b) $t = 2$ (c) $t = 10$ (d) $t = 18$ (e) $t = 21$ (f) $t = 21$

Fig. 5.8 Drop deformation and translation at different time instances for $R = 64$ and $Q = 6.4$ using the flow parameters $Ca_E = 0.12$ and $Re = 1$. We also plot the flow patterns at $t = 21$.

Figure 5.9 shows the drop translation and the associated hydrodynamic flow phenomena for the system $(R, Q) = (0.1, 1.0)$. The initial spherical drops deform into an oblate shape. The bulk hydrodynamic flow is from the poles to the equator as $R < Q$. The flow circulations around the drops make them translate towards each other. The value of ζ for this system is around 0.17, which says that the hydrodynamic forces aid

the drops in coming closer. Here also, two asymmetric vortex pairs are formed inside the drops and there is a net force inside the drops that make them move towards each other. As time progresses, the drops come closer, and the interfaces touch each other, as observed in Figure 5.9(f). Immediately after they touch, the flow scenario inside the drop changes. The net hydrodynamic force inside the drop tries to separate them, while the outer hydrodynamic forces push the drops together. This balance between the forces makes the drops stay together without coalescing, and the drops reach a steady state.

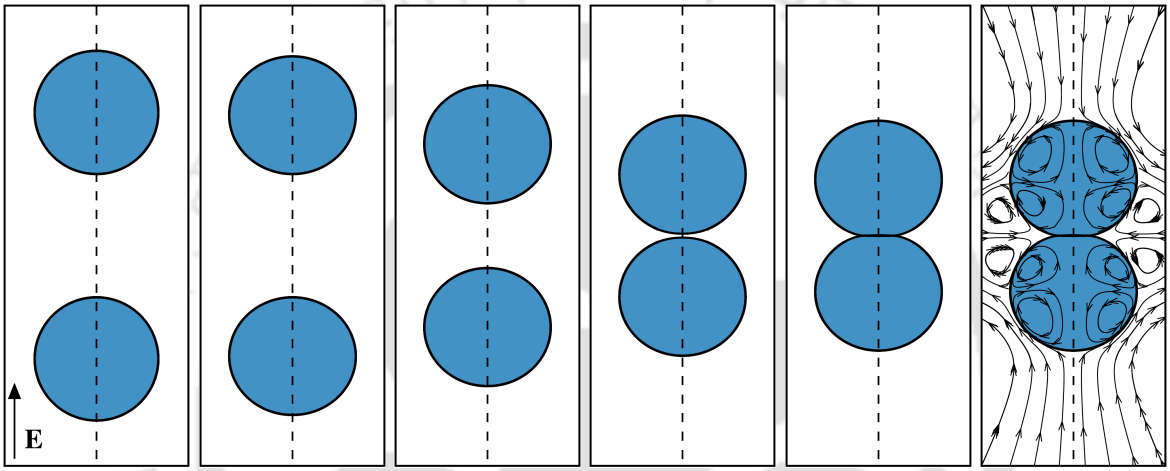

(a) $t = 0$ (b) $t = 5$ (c) $t = 35$ (d) $t = 53$ (e) $t = 70$ (f) $t = 70$

Fig. 5.9 Drop deformation and translation at different time instances for $R = 0.1$ and $Q = 1$ using the flow parameters $Ca_E = 0.12$ and $Re = 1$. We also plot the flow patterns at $t = 70$.

Figure 5.10 shows the drop translation and the associated hydrodynamic flow phenomena for the system $(R, Q) = (0.025, 0.16)$. Due to the nature of the electric stresses, the initial spherical drops deform into a prolate shape. Here $R < Q$ and the bulk hydrodynamic flow is from the poles to the equator. The value of ζ for this system is around 1.32, implying that the hydrodynamic and electrostatic forces are almost equivalent. They both bring the drops closer. Inside the drop, the relative strengths of the hydrodynamic forces by the vortex pairs make the drops come closer. As time progresses, the drops come closer, and the interfaces touch each other, as observed in Figure 5.10(f). Here again, the flow scenario inside the drop changes. The net hydrodynamic force inside the drop tries to separate them, while the outer hydrodynamic forces push the drops together. This balance between the forces makes the drops stay together without coalescing.

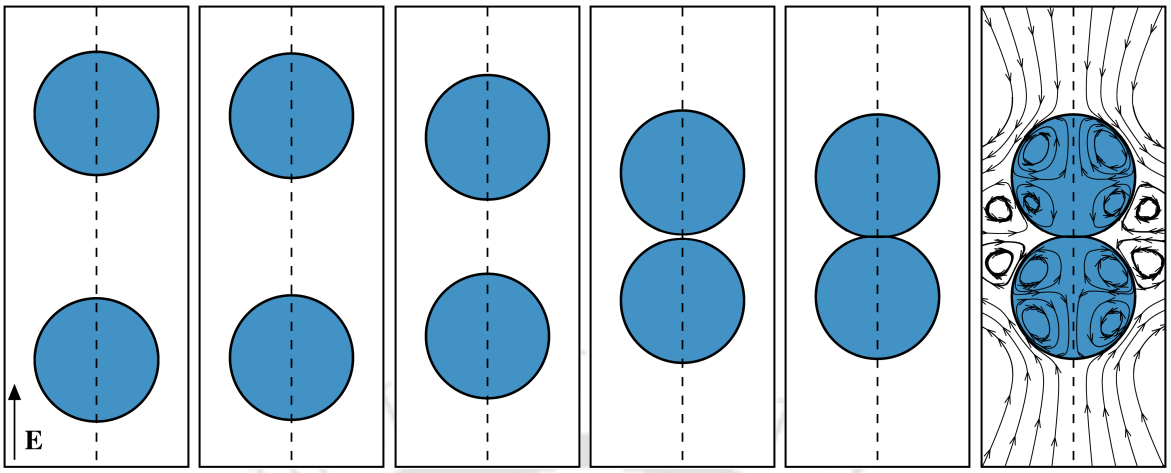

(a) $t = 0$ (b) $t = 10$ (c) $t = 70$ (d) $t = 120$ (e) $t = 140$ (f) $t = 140$

Fig. 5.10 Drop deformation and translation at different time instances for $R = 0.025$ and $Q = 0.16$ using the flow parameters $Ca_E = 0.12$ and $Re = 1$. We also plot the flow patterns at $t = 140$.

Figure 5.11 shows the drop translation and the associated hydrodynamic flow phenomena for the system $(R, Q) = (1.5, 10.0)$. Due to the nature of the electric stresses, the initial spherical drops deform into an oblate shape. Here $R < Q$ and the bulk hydrodynamic flow is from the poles to the equator. The electrostatic forces always tend to bring the drops closer. Consequently, the flow patterns also make the drops come closer to each other. The value of ζ for this system is around 0.0055, which implies that the hydrodynamic forces are very strong and assist the drops in coming together. The flow dynamics for both inner and outer regions around the drop can be seen clearly in Figure 5.11(f). Inside the drop, two asymmetric vortex pairs are formed. Considering the relative strengths of the hydrodynamic forces by these vortex pairs, it is clear that there is a net force that makes the drops come closer, and eventually, the drops coalesce.

Figure 5.12 shows the drop translation and the associated hydrodynamic flow phenomena for the system $(R, Q) = (25, 40)$. Due to the nature of the electric stresses, the initial spherical drops deform into a prolate shape. Here $R < Q$ and the bulk hydrodynamic flow is from the poles to the equator. The flow dynamics for both inner and outer regions around the drop can be seen clearly in Figure 5.12(f). Both inside and outside the drop, the flow pattern is such that it brings the drops closer. The value of ζ for this system is around 7.22, implying a weaker hydrodynamic force than the electrostatic force. Nevertheless, both forces tend to bring the drops closer. Due to the

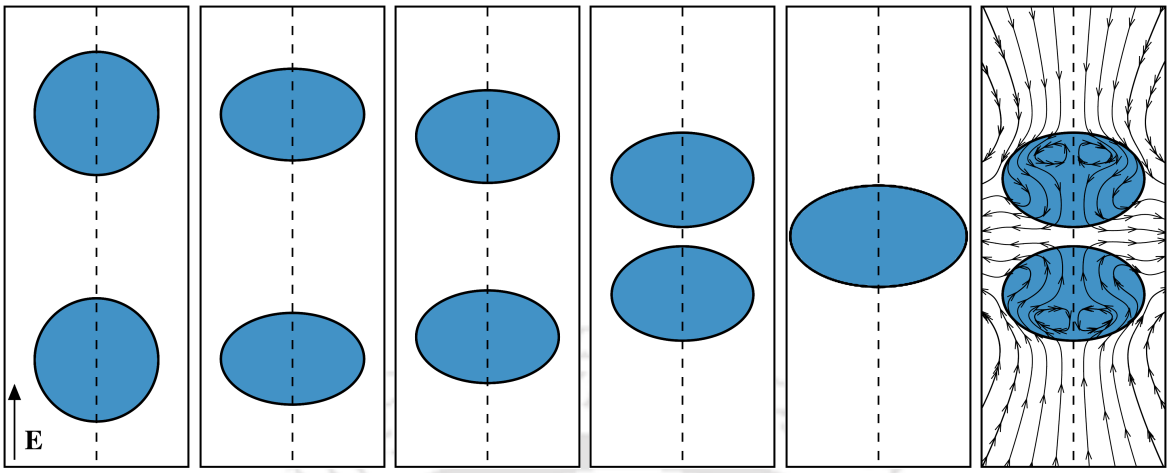

(a) $t = 0$ (b) $t = 1$ (c) $t = 10$ (d) $t = 19$ (e) $t = 35$ (f) $t = 19$

Fig. 5.11 Drop deformation and translation at different time instances for $R = 1.5$ and $Q = 10$ using the flow parameters $Ca_E = 0.12$ and $Re = 1$. We also plot the flow patterns at $t = 19$.

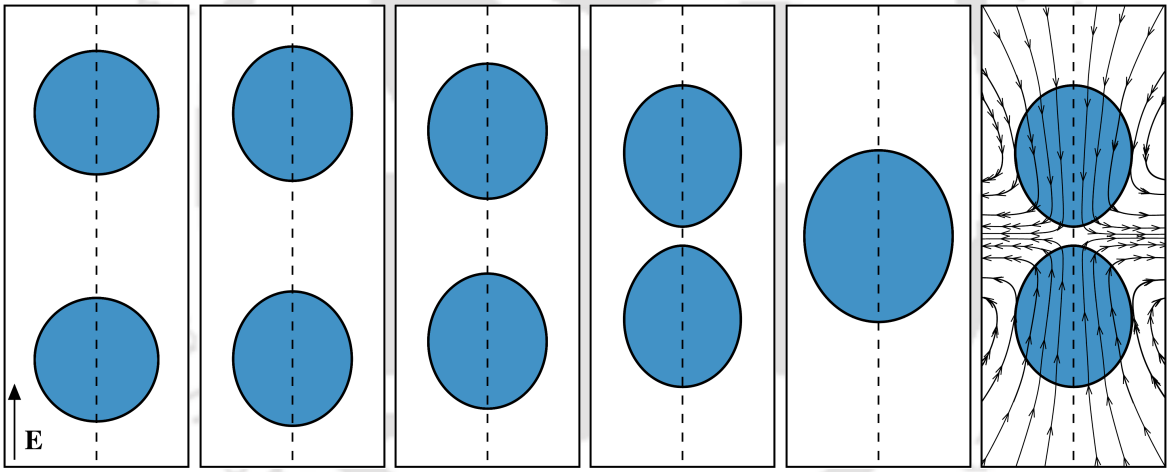

(a) $t = 0$ (b) $t = 2$ (c) $t = 16$ (d) $t = 24$ (e) $t = 32$ (f) $t = 24$

Fig. 5.12 Drop deformation and translation at different time instances for $R = 25$ and $Q = 40$ using the flow parameters $Ca_E = 0.12$ and $Re = 1$. We also plot the flow patterns at $t = 24$.

high value of the permittivity ratio for this system, enormous charges are developed at the interface leading to a high value of electrostatic forces. This results in the drops coming closer and finally coalescing into a single drop.

5.4.2 Regime map for interacting drop pair

Unlike the previous work, including inertial effects (in contrast to Stokes regime) reveal interesting regimes for the drop interaction under an electric field. We still observe the expected shape response for a pair of drops and the circulation patterns Baygents et al. (1998). In addition, we find that the drops can also come close and not coalesce but instead form a stable thin film between them. For $R = 16$ and $Q = 1$, Figure 5.7 shows the formation of a thin film between a drop pair. As the two drops approach each other, asymmetry in the shape starts to appear. The electric field magnitude is higher in the region between the drops, which also induces higher charge density

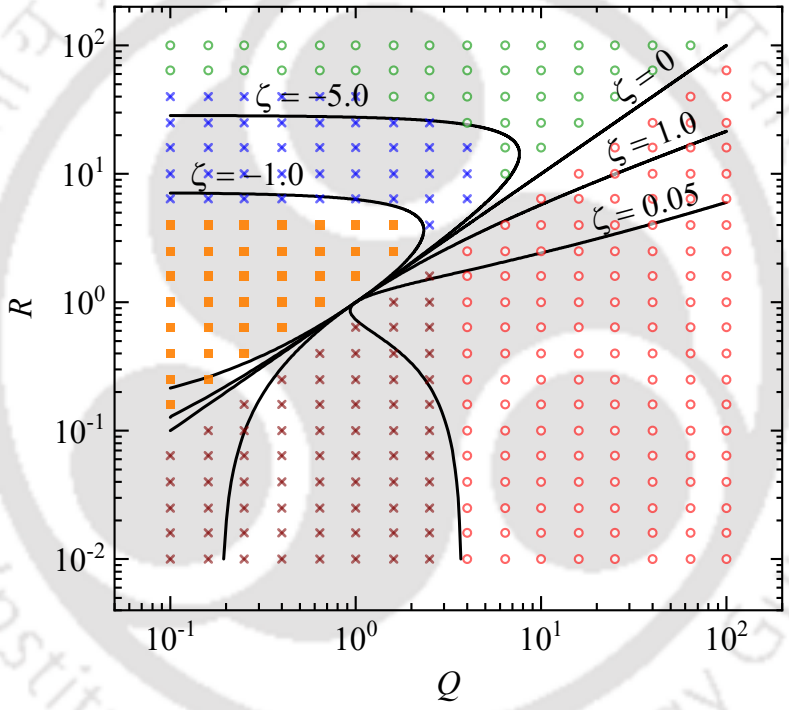

Fig. 5.13 A regime plot showing the various interaction dynamics between a pair of drops when subjected to an uniform electric field. The properties considered in the numerical study are $Ca_E = 0.12$, $Re = 1$, $\mu_r = 1$, and $\rho_r = 1$. An open circle (○) denotes drop coalescence, a cross mark (×) denotes thin film formation, and a square (■) denotes drop separation.

at the interfaces. This leads to a high magnitude of the electrostatic stresses on the leading poles, which are balanced by the capillary force by adjusting the curvature. We also observe a high pressure between the drops, which retards the motion of the approaching surfaces. The pressure reaches its maximum at the center and minimum at the periphery of the thin film; thus, a dimple shape of the thin film is observed.

At such small separations, the Maxwell stresses overcome the lubrication resistance. However, the drainage of the film is prevented by the converging flow in bulk, resulting in a stable thin film. Similar thin film formation phenomena for other combinations of electrical properties for a given Ca_E.

Figure 5.13 shows the different conductivity and permittivity ratios regimes for which the above stable thin film phenomenon is observed. We introduce several regimes on the phase plot to characterize the interaction dynamics of the drop pairs. The points denoted by an open circle (○) represent the coalescence of drops, the points denoted by a cross mark (×) represent a thin film formation, while the points denoted by a square (■) represent the drops moving apart. Electrostatic forces are always attractive, but the hydrodynamic forces due to the circulation flow generated by the electrical stresses at the drop interfaces can determine the nature of the interaction. An estimate of the ratio of hydrodynamic forces (F_h) and electrostatic forces (F_e) has been obtained to determine the nature of the interaction dynamics of a pair of drops. As shown in Figure 5.13, for $\zeta > -5$, the electrostatic forces overcome the weak hydrodynamic repelling forces and make the drops coalesce. Furthermore, for $\zeta < -1.0$, the hydrodynamic repelling forces make the drops move apart. Interestingly, the drops form a thin film without coalescing for $-1.0 < \zeta < -5$. Additionally, for $\zeta > 0.05$, the strong hydrodynamic attractive forces aid the electrostatic forces in the coalescence of the drops. While for $\zeta < 0.05$, the drops again form a thin film without coalescence. The curves shown in Figure 5.13 help in demarcating the behavior of the drop. We note that the theoretically obtained limiting lines match well with the computational results. We would also like to note here that the given phase boundaries such as $\zeta = -5$ and $\zeta = 0.05$, are functions of Ca_E. The several new regimes for leaky-dielectric drops representing the thin film formation obtained here have been observed in experiments (Mhatre et al., 2015a) but have not been observed in earlier numerical studies since they were performed in the Stokes limit.

5.5 Summary

In the present study, we have investigated the interaction dynamics of a pair of leaky-dielectric drops under the influence of an external electric field. This numerical study utilized an axisymmetric domain to understand drop dynamics. We also validated our computational model with previous experimental work. The previous investigation by Baygents et al. (1998) studied the drop pair dynamics using creeping flow approxima-

tions. Their study defined a map that showed drops could either move apart or come close based on the electrical conductivity and permittivity ratios. This work showed that we could obtain different drop interaction dynamics for a small finite Reynolds number. While we obtained the previous results of drops translating together and drops moving apart, we also found that drops can come closer and form a thin film without coalescing. Based on this observation, we defined a phase map representing regions for various drop interaction dynamics. It is to be noted that this map is valid only for the electrical capillary number of $Ca_E = 0.12$. Nevertheless, this phase map gives a general idea about the interaction dynamics for a pair of leaky-dielectric drops under the influence of an external electric field. This work can assist in performing experimental investigations in these regimes to understand the mechanism behind the thin film formation.

Chapter 6

Viscoelastic effects on drop deformation

The effect of viscoelasticity on drop deformation is studied using a finite volume based solver. We consider a system with a leaky-dielectric drop suspended in a leaky-dielectric medium. To investigate the effect of viscoelasticity, we consider either the drop or the medium as viscoelastic. Accordingly, we get two configurations. We use the Oldroyd-B constitutive model to study the drop dynamics. The applied electric field deforms the drop with some deviations from its Newtonian counterpart. The chapter starts by outlining the previous investigations on viscoelastic drop deformations (§ 6.1). Then, the computational model used to study electrohydrodynamic flows is described (§ 6.2). Next, the model is validated with earlier studies (§ 6.3). The effects of viscoelasticity on drop deformation are subsequently explored (§ 6.4). The chapter then concludes with a summary of the outcomes (§ 6.5).

6.1 Introduction

Understanding polymer blends is essential in foods, paints, cosmetics, and processing industries. The properties of these emulsions are directly related to the microstructure of the polymers resulting from drop deformation, coalescence, and breakup. For dilute emulsions, the dynamics of a single drop provide complete information about its behavior. Consequently, extensive studies have been conducted to investigate drop deformation and breakup in simple linear flows (Taylor, 1932). Most of these emulsion studies were restricted to both phases being Newtonian (Stone, 1994). However, non-

Newtonian fluids can significantly affect the dynamics of drop deformation and breakup (Tucker and Moldenaers, 2002; Yue et al., 2005).

Most investigations for non-Newtonian emulsions study the effect of shear and extensional flows. The viscosity ratio and the capillary number govern the drop dynamics of Newtonian systems. The capillary number is the ratio of the viscous stretching force to the interfacial resistive force. A critical capillary number exists, below which the drops retain their elongated shapes and above which the drops break. Introducing viscoelasticity changes the extent of drop deformation and the critical capillary number for the breakup. The effect of viscoelasticity has been attributed to the combined effect of non-zero normal stresses, changes in viscous and viscoelastic stresses, and flow modification (Ramaswamy and Leal, 1999a,b; Yue et al., 2005). The deformation of a viscoelastic drop decreases compared to a Newtonian drop due to the presence of normal stresses in the drop phase. Gauthier et al. (1971) and Varanasi et al. (1994) found a higher critical capillary number for viscoelastic drops in a Newtonian matrix. Flumerfelt (1972) performed experiments for a Newtonian drop sheared in a viscoelastic matrix and found the critical shear rate to increase with increasing matrix elasticity. Elmendorp (1986) considered both systems where either the drop or the matrix phase was viscoelastic. They concluded that drop elasticity inhibited deformation, whereas matrix elasticity enhanced it in a simple shear flow. Mighri et al. (1997, 1998) experimented with Boger fluids and came to the same conclusion regarding the effect of viscoelasticity on drop deformation. However, Guido et al. (2003) and Sibillo et al. (2004) found that matrix viscoelasticity impedes drop breakup in simple shear flows.

Greco (2002) computed a perturbative solution for a second-order drop and matrix model. He found a deviation from the Newtonian model only in the drop orientation angle and not in deformation at small capillary numbers. Maffettone and Greco (2004) performed calculations with an ellipsoidal drop shape assumption and predicted a less deformed Newtonian drop suspended in a viscoelastic matrix. Toose et al. (1995) simulated a viscoelastic drop deformation using a boundary integral method and concluded that for small deformations, drop viscoelasticity affects only the transient behavior. Ramaswamy and Leal (1999a,b) and Hooper et al. (2001) used a finite element method to investigate the axisymmetric deformation of viscoelastic drops in a uniaxial extensional flow. They used FENE-CR and Oldroyd-B constitutive equations for their studies and reported reduced deformation for viscoelastic drop and enhanced deformation in the opposite case. Using finite element simulations, Pillapakkam et al.

(2007) observed a non-monotonic change in the deformation of Newtonian drops in a viscoelastic matrix. Yue et al. (2005) explained this non-monotonic behavior using the variation in stresses. Their study was conducted using a diffuse interface method. Unlike shear and extensional flow studies, investigations for electrohydrodynamic flows for viscoelastic phases are limited. Ha and Yang (2000a) experimentally observed the effects of viscoelasticity on the deformation and breakup of a drop in a uniform electric field. They concluded that the critical electric field strength of viscoelastic drops was increased. Lima and D'Ávila (2014) performed numerical simulations using a finite volume method and found that the drop deformation decreased with increased relaxation time. They performed their simulations using a Giesekus constitutive model.

In this chapter, we present a two-dimensional axisymmetric study of drop deformation using the Oldroyd-B model at a finite Reynolds number. Either the drop or matrix has been considered to be viscoelastic. Oldroyd-B has been considered in this study as it has a shear-independent viscosity and sustains a positive first normal stress and a zero second normal stress. It is a quasi-linear constitutive model with a single relaxation time. We consider both phases to be leaky-dielectric in nature.

6.2 Formulation

6.2.1 Computational domain

We study the effect of an electric field on the deformation of a drop suspended in a medium. The drop/medium is considered to be viscoelastic. Accordingly, we have two configurations: a viscoelastic drop suspended in a Newtonian fluid (VN), and a Newtonian fluid suspended in a viscoelastic medium (NV). We study the dynamics for a leaky-dielectric drop in a leaky-dielectric medium using an axisymmetric cylindrical coordinate system (r, z).The initial undeformed spherical drop is kept at the center of the domain, as shown in Figure 6.1. The extent of the domain in both the radial and axial directions is $16a$, where a is the radius of the drop. The properties of the drop are denoted by subscript 1, whereas the ambient fluid is denoted using the subscript 2. Electric permittivities and conductivities are ε_1 and σ_1, respectively, for the drop, and ε_2 and σ_2 for the medium. The drops are neutrally buoyant with densities $\rho_1 = \rho_2$. Viscosity of the fluids 1 and 2 are given by μ_1 and μ_2, respectively. The viscoelastic phase has both solvent (μ_s) and polymer (μ_p) viscosity. The fluids involved are assumed to be incompressible, and the surface tension coefficient of the interface between the

two fluids is given as $\gamma_{12} = \gamma$. The chosen computational domain is large enough to neglect the effect of boundaries on the dynamics of the drop at the time scales considered in this study.

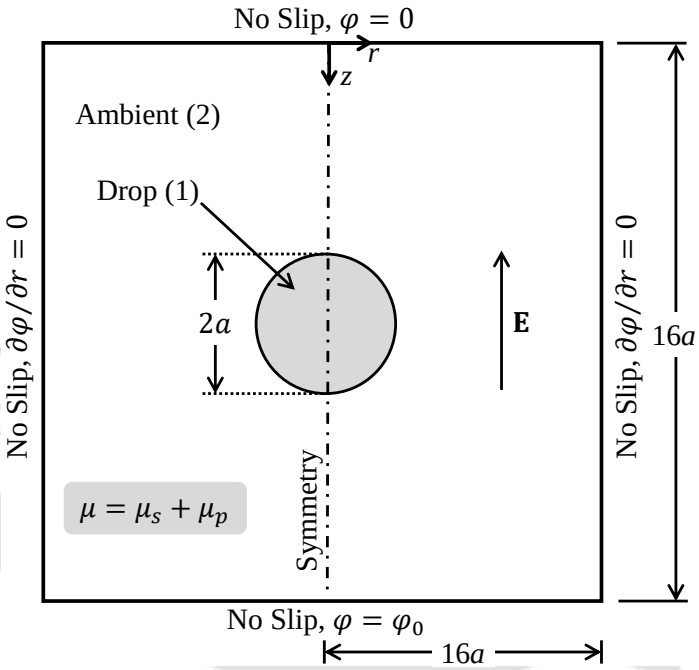

Fig. 6.1 Schematic diagram (not to scale) showing the initial configuration and boundary conditions in an axisymmetric cylindrical coordinate system (r, z). The radius of the drop is a. Electric field ($\mathbf{E}$) is applied along negative z axis. The size of the domain is $16a \times 16a$. Viscoelasticity of a phase will have both solvent (μ_s) and polymer (μ_p) viscosity.

6.2.2 Solution methodology

Using the one-fluid formulation, we solve the tho-phase system governed by the modified incompressible Navier-Stokes equations. The modified momentum equation incorporates the surface tension force, polymeric stresses, and the electric force for the volume.

$$\boldsymbol{\nabla} \cdot \mathbf{u} = 0 \ ,$$

$$\rho\left[\frac{\partial \mathbf{u}}{\partial t} + \mathbf{u} \cdot \boldsymbol{\nabla}\mathbf{u}\right] = -\boldsymbol{\nabla}p + \boldsymbol{\nabla}\cdot\left[\mu_s\left(\boldsymbol{\nabla}\mathbf{u} + \boldsymbol{\nabla}\mathbf{u}^T\right)\right] + \boldsymbol{\nabla}\cdot\mathbb{T}_p + \gamma\kappa\delta_s\hat{\mathbf{n}} + \boldsymbol{\nabla}\cdot\left[\varepsilon\left(\mathbf{EE} - \frac{E^2}{2}\mathbf{I}\right)\right]$$

We perform the viscoelastic studies for an Oldroyd-B model whose constitutive relation is given as

$$\lambda\left[\frac{\partial \mathbb{T}_p}{\partial t}+\mathbf{u}\cdot\boldsymbol{\nabla}\mathbb{T}_p-(\boldsymbol{\nabla}\mathbf{u})\cdot\mathbb{T}_p-\mathbb{T}_p\cdot(\boldsymbol{\nabla}\mathbf{u})^T\right]+\mathbb{T}_p=\mu_p\left(\boldsymbol{\nabla}\mathbf{u}+\boldsymbol{\nabla}\mathbf{u}^T\right)$$

An external electric field ($\mathbf{E}$) is applied along the axial direction. It is imposed by applying electric potential φ using the boundary condition on the bottom boundary $(r, z = 16a)$

$$\varphi=\varphi_0\ , \qquad u=v=0\ . \tag{6.1}$$

The top boundary is electrically grounded using the boundary condition $(r, z = 0)$

$$\varphi=0\ , \qquad u=v=0\ . \tag{6.2}$$

Neumann boundary condition for the electric potential is imposed on the right boundary $(r = 16a, z)$

$$\frac{\partial\varphi}{\partial r}=0\ , \qquad u=v=0\ . \tag{6.3}$$

Symmetry boundary conditions are imposed on the axis of symmetry for the velocity field and the electric potential $(r = 0, z)$

$$\frac{\partial\varphi}{\partial r}=0\ , \qquad u=0\ , \qquad \frac{\partial v}{\partial r}=0\ . \tag{6.4}$$

No-slip and impervious velocity conditions are imposed on the other boundaries. The details of the governing equations are defined in Section 2.2.1. The numerical simulations are carried out using the Basilisk solver described extensively in Section 2.2.2.

6.2.3 Dimensionless parameters

The governing equations, along with the boundary conditions, are made dimensionless using the following scaling parameters: undeformed spherical drop radius a is taken as the characteristic length scale, $U_e \sim a\varepsilon_2 E_\infty^2/\mu_2$ is taken as the characteristic velocity scale based on the flow generated by the electric forces, and E_∞ is chosen as the characteristic scale for the electric field. The pressure and the polymeric stress terms are scaled using $\rho_2 U_e^2$. All the fluid properties are scaled using the respective properties of the ambient phase. We obtain the following dimensionless parameters using the

above scaling:

$$Re = \frac{\rho_m \varepsilon_m a^2 E_\infty^2}{\mu_m^2}\,, \qquad Ca_E = \frac{\varepsilon_m a E_\infty^2}{\gamma}\,, \qquad Re_E = \frac{\varepsilon_m^2 E_\infty^2}{\mu_m \sigma_m}\,, \qquad De = \frac{\lambda}{a/U_e}\,. \tag{6.5}$$

Reynolds number Re represents the ratio of the inertia forces to the viscous forces, and the electric capillary number Ca_E represents the ratio of the electrostatic forces to the surface tension forces. The term Re_E is the electric Reynolds number which denotes the ratio of the charging time scale to the flow time scale. Furthermore, two additional dimensionless parameters are involved in studying viscoelastic fluids. $\beta = \mu_s/(\mu_s + \mu_p)$ gives the ratio of the solvent viscosity to the total viscosity of that phase. Deborah number De represents the ratio of the relaxation time scale to the flow time scale. The Deborah number indicates how a particular material will behave over a given time frame. If the observation time is long or the relaxation time of the material is short, then a fluid-like behavior is expected. In contrast, if the relaxation time of the material is large or the observation time is short, then the Deborah number is high, and the material exhibits a solid-like behavior. The dimensionless parameters for other properties are the electrical conductivity ratio $R = \sigma_1/\sigma_2$, the electric permittivity ratio $Q = \varepsilon_1/\varepsilon_2$, the viscosity ratio $\mu_r = \mu_1/\mu_2$, and the density ratio $\rho_r = \rho_1/\rho_2$. We have considered $\mu_r = 1$ and $\rho_r = 1$ in the present study. A detailed derivation of the dimensionless equations is described in Appendix B.

6.3 Validation

6.3.1 Comparison with literature

We validate the numerical model used in this study with previous investigations. To the best of our knowledge, very few studies exist on the electrohydrodynamics of viscoelastic fluids. Hence, we validate the two physics separately. The electrohydrodynamics part of the solver has been validated well in the previous chapters. Here, we compare the viscoelastic two-phase flow results of the present solver with the work of Figueiredo et al. (2016). Figueiredo et al. (2016) studied the dynamics of a deformable drop under a pure Couette shear flow, in which either or both the drop and ambient fluid has been considered viscoelastic fluid. A drop of radius a is positioned at the center of a rectangular domain and is subjected to a shear flow, with the top and bottom walls moving in opposite directions. The viscoelastic fluid considered was an Oldroyd-B

fluid, with $\beta = 0.5$. The other parameters used in the study are capillary number $Ca = 0.6$, Reynolds number $Re = 0.3$, and Deborah number $De = 0.4$. They defined the deformation parameter as the ratio between the smaller and the larger distances of the drop interface up to the drop center, as $D = (a_{max} - a_{min})/(a_{max} + a_{min})$. Figure 6.2 compares this deformation obtained by the present solver with the work of Figueiredo et al. (2016), which is in good agreement. In the case of viscoelastic drop and Newtonian ambient fluid (VN), the drop deforms continuously with time. In comparison, the drop settles to a stationary state for a Newtonian drop in a viscoelastic ambient (NV).

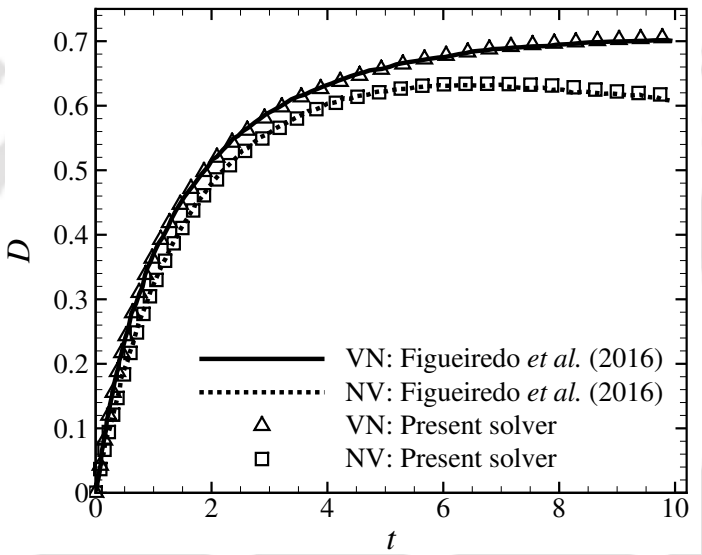

Fig. 6.2 Temporal evolution of the deformation parameter (D) for two different configurations. Other dimensionless parameters for the computations are $Ca = 0.6$, $Re = 0.3$, $De = 0.4$, and $\beta = 0.5$.

6.3.2 Grid independence studies

A grid convergence study is performed to ensure the results are independent of the grid resolution. The adaptive meshing capability of the solver allows us to use very fine mesh near the interface and a relatively coarser mesh away from the drop. This results in less computational time than studies using a uniform grid. The entire interface is resolved using Δx_{min}, and the grid is progressively coarsened ($l = 6$) away from the drop. We consider the deformation of a viscoelastic drop suspended in a Newtonian fluid. The parameters used for the test are $R = 0.5$, $Q = 2$, $Re = 1$, $Ca_E = 0.2$, $De = 1$, $Re_E = 0.01$, $\beta = 0.1$, $\mu_r = 1$ and $\rho_r = 1$. The temporal evolution of the drop

deformation (D) is plotted in Figure 6.3. It can be observed from the inset that the curves corresponding to $a/\Delta x_{min} = 256$ ($l = 12$) and 512 ($l = 13$) almost overlaps, and hence a further grid refinement would have a negligible effect. The maximum difference was 0.09%. Hence, a grid refinement level of 12 has been used for the rest of the study to minimize the computational cost.

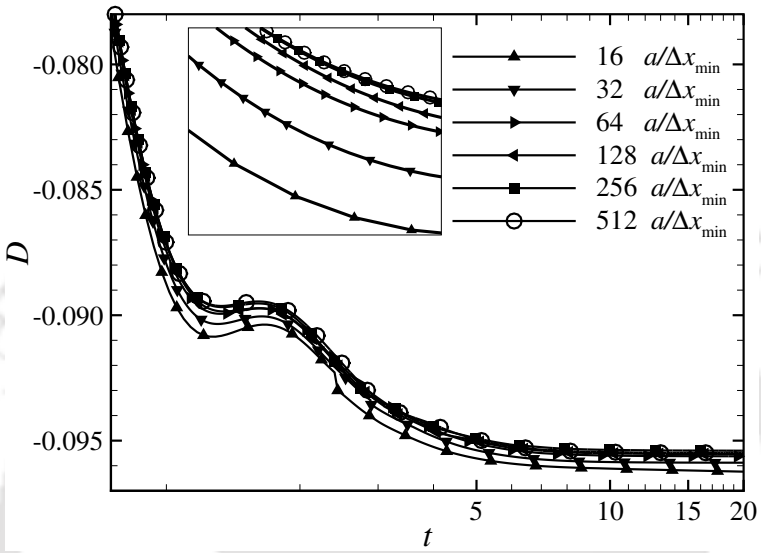

Fig. 6.3 Temporal evolution of drop deformation (D) for different levels of grid refinement. The inset shows the zoomed view for better convergence analysis. The dimensionless parameters for the computations are $R = 0.5$, $Q = 2$, $Re = 1$, $Ca_E = 0.2$, $De = 1$, $Re_E = 0.01$, $\beta = 0.1$, $\mu_r = 1$ and $\rho_r = 1$.

6.4 Results and discussion

In this section, we study the deformation and stability of two configurations: a viscoelastic drop suspended in a Newtonian fluid (VN), and a Newtonian fluid suspended in a viscoelastic medium (NV). The application of a uniform electric field leads to a deformation of the drop. Due to the presence of viscoelastic fluid in a medium, we observe different dynamics compared to Newtonian fluids. For all the studies, we fix $Re = 1$, $Re_E = 0.01$, $\beta = 0.1$, $\rho_r = 1$ and $\mu_r = 1$. The governing dimensionless parameters for the studies are R, Q, Ca_E, and De. First, we present the transient drop deformation dynamics followed by the steady state dynamics.

6.4.1 Transient drop deformation

Figure 6.4 shows the drop deformation as a function of time for $R = 10$, $Q = 0.1$, $Ca_E = 0.2$ and varying De. We also plot the deformation history for a Newtonian drop represented by $De = 0$. The steady-state value of deformation D for VN configuration decreases with an increase in De owing to increased viscoelastic stresses inhibiting the drop deformation. In contrast, for NV configuration, the viscoelastic stresses aid in deforming the drop, and consequently, D increases with an increase in De. We observe overshoots and oscillations in the transient deformation for both configurations. This is attributed to the relaxation time associated with the Oldroyd-B model, which leads to a finite time interval for the development of the viscoelastic stresses. These variations in temporal deformations have also been reported in previous studies (Aggarwal and Sarkar, 2007; Yue et al., 2005). The deformation is significant for the VN configuration, while we find the deformation to change by a very small amount for the NV configuration. The deviation in steady-state deformation with De observed here is due to the nonlinear nature of the Oldroyd-B constitutive equation, which gives rise to a finite first normal stress difference.

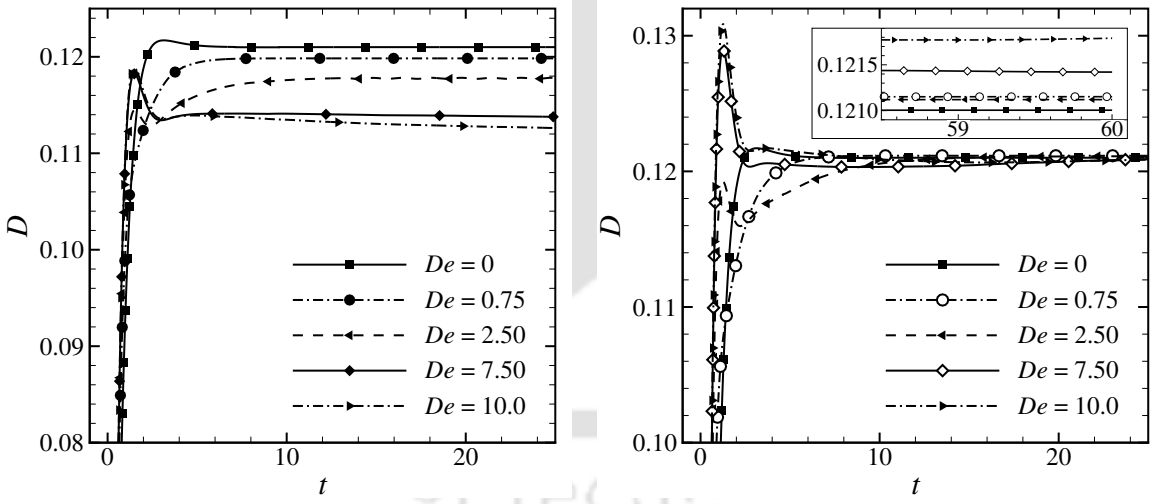

(a) VN (b) NV

Fig. 6.4 Effect of De on deformation of drop for $Ca_E = 0.2$, $R = 10$ and $Q = 0.1$. The inset for NV configuration shows that at steady-state the deformation increases with an increase in De.

6.4.2 Steady state drop deformation

The steady-state drop deformation is calculated for the two configurations, VN and NV. The drop deformation is represented as $D = (L - B)/(L + B)$. The deformation values are normalized by the Newtonian drop deformation D_N (at $De = 0$). Figure 6.5 shows the plot of D/D_N as a function of De for two values of Ca_E. In the case of VN, D/D_N decreases monotonically with increasing De. On the other hand, for NV, the curve has a non-monotonic nature. The deformation reaches a minimum and then increases, although the overall effect is still an increase in deformation. Thus, viscoelasticity in the drop decreases deformation. While the viscoelasticity in the ambient phase suppresses drop deformation for small De, but enhances drop deformation for large De. This trend of viscoelasticity is also observed for drop deformation in steady shear (Aggarwal and Sarkar, 2007, 2008). The stress fields around the drop are examined to understand such behavior.

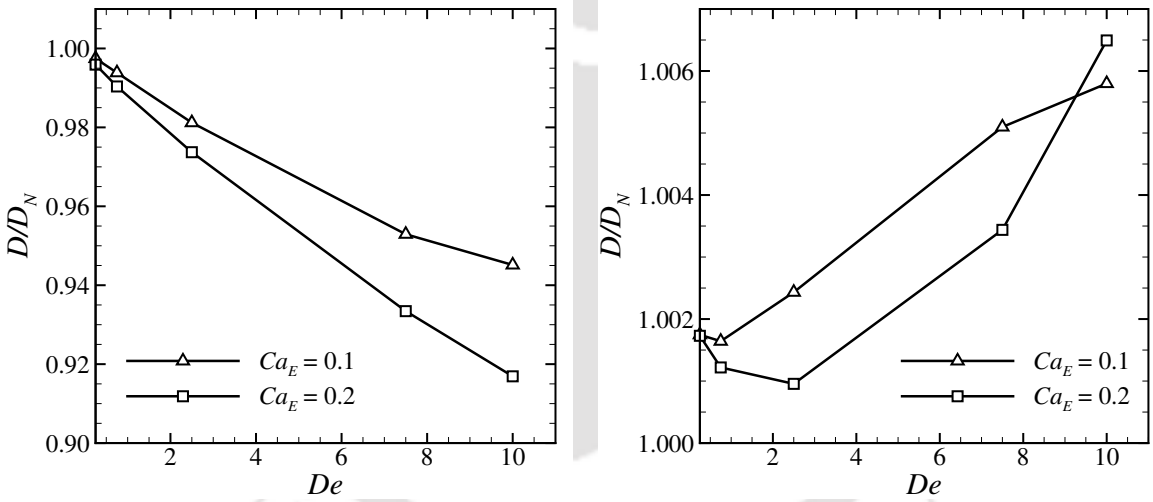

(a) VN (b) NV

Fig. 6.5 Steady-state deformation variation D/D_N (normalized with D at $De = 0$) with De for two different $Ca_E = 0.1, 0.2$. The electrical parameters are $R = 10$ and $Q = 0.1$. The effect of viscoelasticity is more prominent in the study of VN system.

We evaluate the stresses on the inside edge of the drop interface as a function of angular position θ from the electric field direction. Figure 6.6 shows the variation of normal electric stress (τ_{en}) and tangential electrical stress (τ_{et}). The normal electric stresses at the poles cause the drop to increase L in the direction of the electric field, while at the equator, the normal electric stress reduces B. This results in an overall prolate deformation of the drop. Since the electric stresses are not affected by the flow

field, they remain constant for all the De considered for the study. Hence, we do not show their variation and consider the variation of viscous and viscoelastic stresses. For an Oldroyd-B drop deforming in a Newtonian matrix outside the drop, the normal force on the interface is identical to a Newtonian drop. However, inside the drop, the viscoelastic stresses cause a reduction in drop deformation.

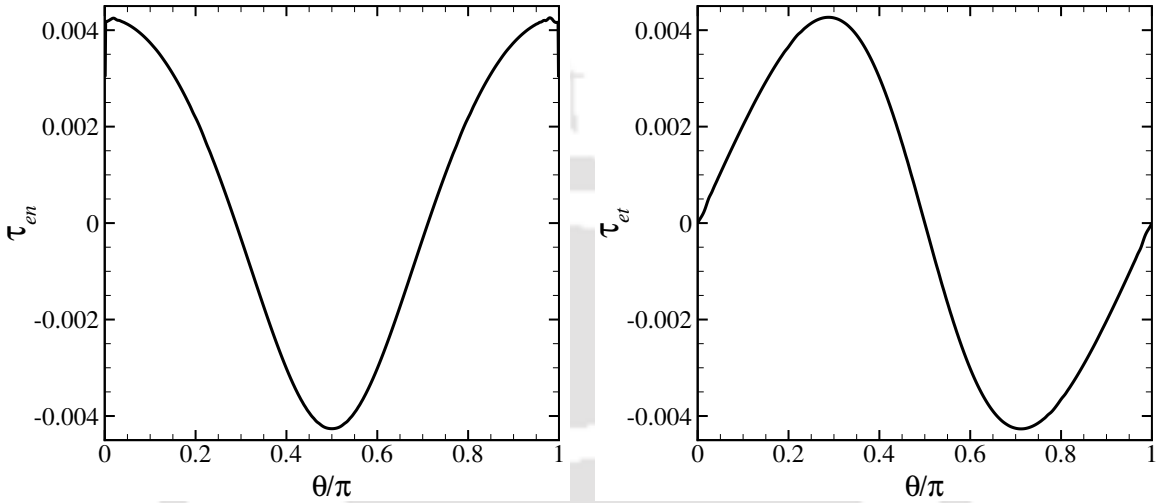

Fig. 6.6 Plot of electric stresses (a) normal τ_{en} and (b) tangential τ_{et} along the inside edge of the interface at $Ca_E = 0.2$, $R = 10$ and $Q = 0.1$. These stresses do not change with the flow field and only depend on the electric field strength.

In Figures 6.7(a) and 6.7(c), we plot the normal component of the viscous (τ_{sn}) and viscoelastic (τ_{pn}) stresses along the circumference of the drop. The viscous normal stress reduces with an increase in De at the poles but does not change much at the equator. The viscoelastic normal stress shows an increase in its peak value with increasing De. These viscoelastic normal stresses are maximum around the drop poles, exerting an inward pull at the poles, reducing L. We observe a minute increase in viscoelastic normal stress at the equator with De. This stress exerts an outward push which increases B. The magnitude of viscous normal stress is significantly less than that of viscoelastic normal stress. The stresses tangential to the drop interface are shown in Figures 6.7(b) and 6.7(d). The viscous tangential stresses (τ_{st}) decrease at the poles with an increase in De. The viscoelastic tangential stress (τ_{pt}) increases at the poles with an increase in De. Here again, we observe that the magnitude of the viscous tangential stresses is small compared to the viscoelastic stresses. Hence, the overall effect of viscoelasticity dominates. The drop interface has a net inward pull

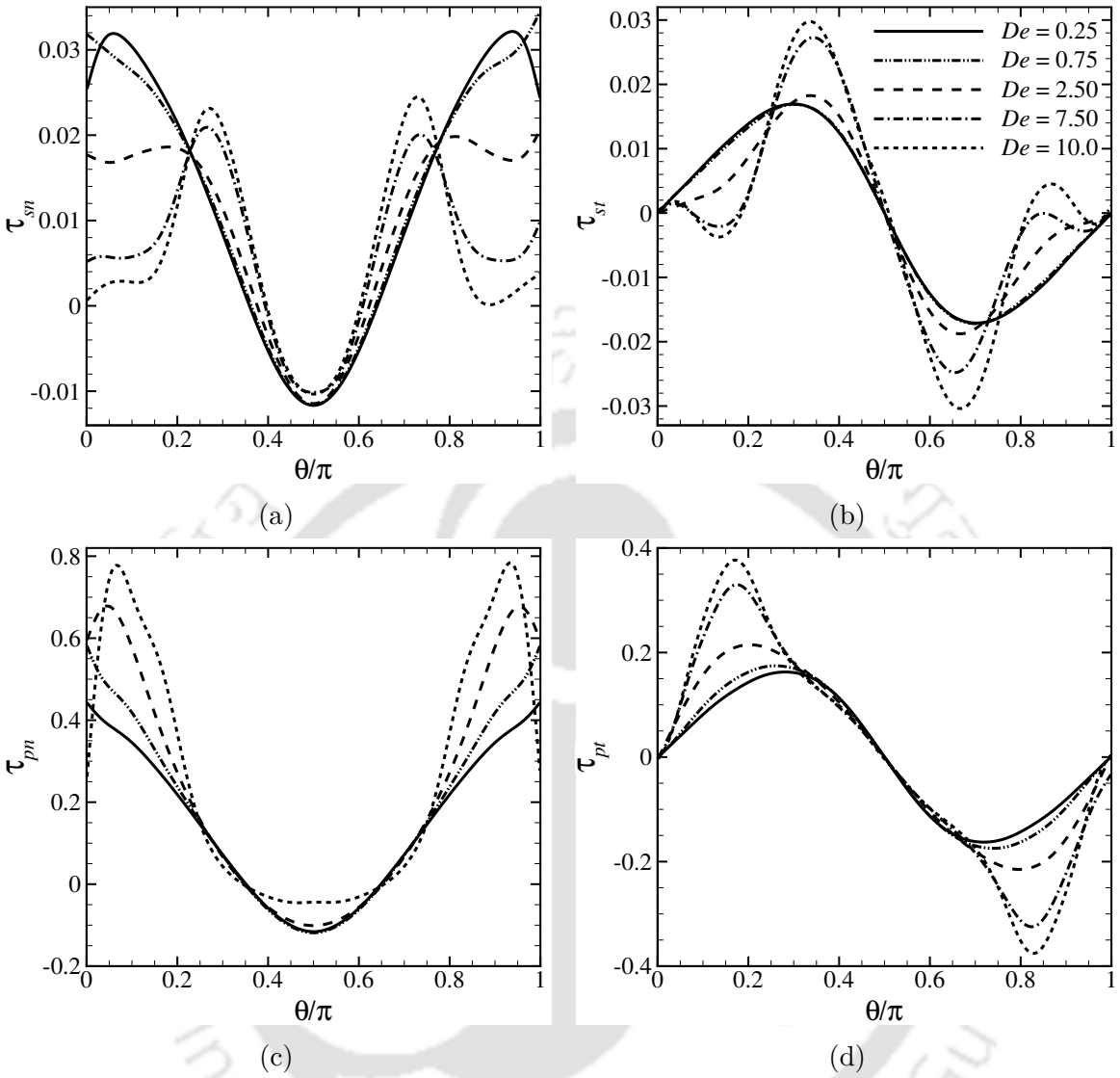

Fig. 6.7 Stresses along the inner edge of the interface for VN configuration at $Ca_E = 0.2$. (a) The viscous normal stress τ_{sn} and (b) the viscous tangential stress τ_{st}, due to the solvent in the Oldroyd-B fluid. (c) The polymer normal stress τ_{pn} and (b) the polymer tangential stress τ_{pt}, being the inward normal to the interface. The electrical parameters are $R = 10$ and $Q = 0.1$.

due to the hoop stress effect caused by the tangential stress at the poles. This induces a high pressure at the drop equator and thus pushes the drop outwards, increasing B. Near the equator of the drop, the viscous and viscoelastic tangential stresses do not show much variation and hence do not contribute much to the deformation of the drop. We observe that the viscoelastic normal stress at the poles decreases L, and

the viscoelastic tangential stress at the equator increases B, which causes an overall reduction in drop deformation with increasing De.

Now, we switch the phases and consider the NV configuration. For this study, we observed a non-monotonic deformation curve. The variation of normal electric stress (τ_{en}) and tangential electrical stress (τ_{et}) are still the same (not shown here). In Figures 6.8(a) and 6.8(c), we plot the normal component of the viscous (τ_{sn}) and viscoelastic (τ_{pn}) stresses along the outer edge of the drop interface for different De at $Ca_E = 0.20$. The viscous normal stress decreases at the poles with an increase in De. At the equator of the drop, there is not much change in these stresses. With increasing elasticity, the magnitude of the viscoelastic normal stress at the poles increases significantly. The magnitude of viscous normal stress is significantly less than that of viscoelastic normal stress. This results in an overall increase in L. The tangential component of the viscous (τ_{st}) and viscoelastic (τ_{pt}) stresses show peculiar behavior as shown in Figures 6.8(b) and 6.8(d). At the equator, both stresses do not change much with De. The viscous tangential stress decreases with an increase in De at poles. In comparison, the viscoelastic tangential stress first decreases and then increases with De. Here, the magnitude of viscous normal stress is comparable with that of viscoelastic normal stress. This again results in the interface having a net pull due to the hoop stress effect, and high pressure is induced at the equator of the drop. We observe an overall monotonic increase in L due to the viscoelastic normal stresses, and B changes non-monotonically (decreasing viscous stress but increasing viscoelastic stress). This results in a non-monotonic behavior of drop deformation with De.

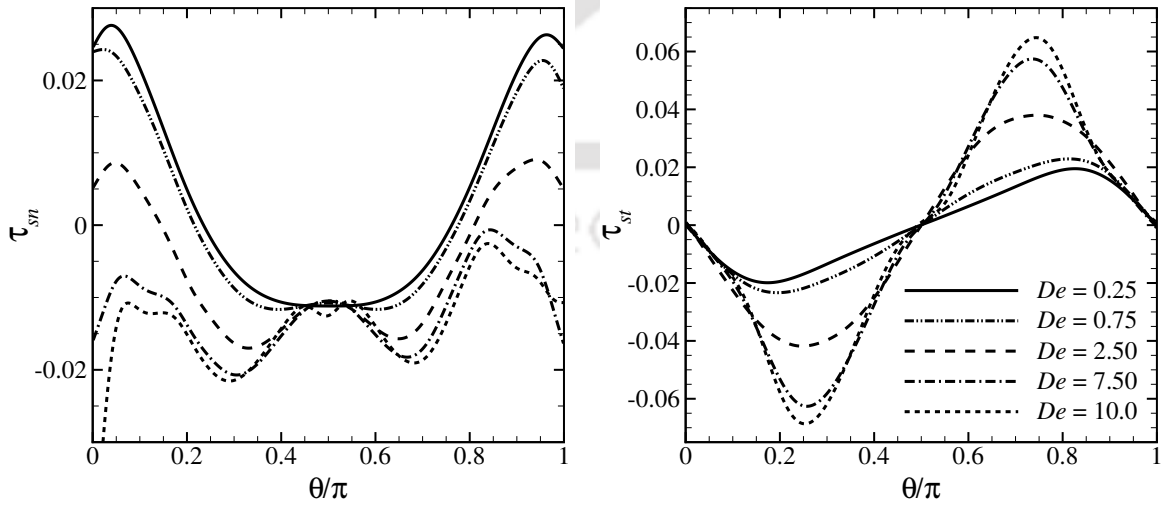

(a) (b)

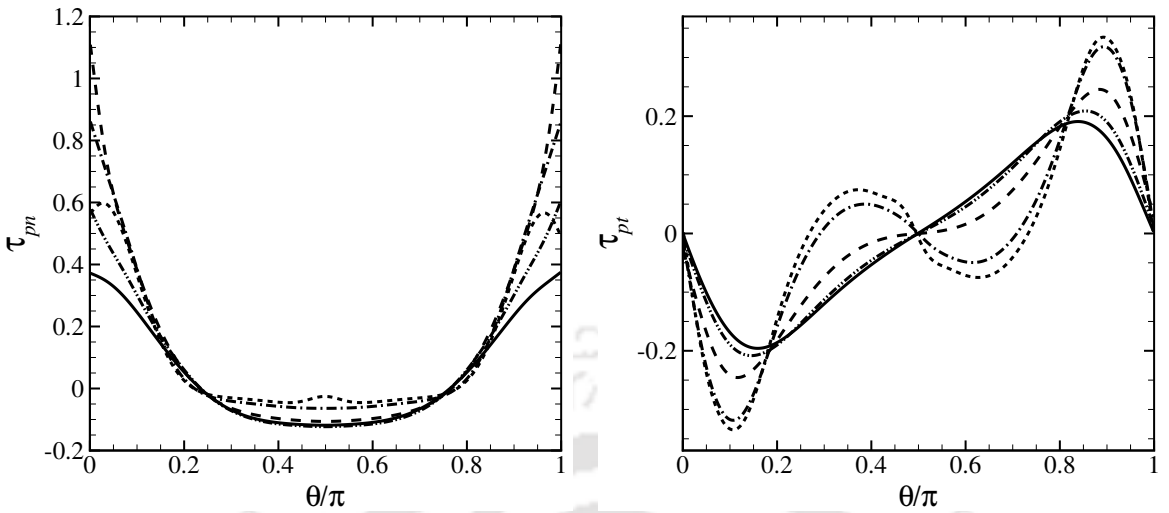

Fig. 6.8 Stresses along the outer egde of the interface for NV configuration at $Ca_E = 0.2$. (a) The viscous normal stress τ_{sn} and (b) the viscous tangential stress τ_{st}, due to the solvent in the Oldroyd-B fluid. (c) The polymer normal stress τ_{pn} and (d) the polymer tangential stress τ_{pt}, being the outward normal to the interface. The electrical parameters are $R = 10$ and $Q = 0.1$.

6.5 Summary

This chapter presented the dynamics of drop deformation in the presence of viscoelastic fluids. We studied the dynamics using an open-source finite volume based solver in a two-dimensional axisymmetric configuration. The two phases were considered to be leaky-dielectric in nature. Drop dynamics of a viscoelastic drop suspended in a Newtonian matrix (VN) and a Newtonian drop suspended in a viscoelastic medium (NV) are investigated. The viscoelasticity was parameterized using the Deborah number (De). The transient drop deformation for both configurations showed overshoots and oscillations. This was due to the non-linear nature of the Oldroyd-B constitutive model. For the VN configuration, drop deformation decreased with an increase in De. The deformation dynamics showed a non-monotonic nature for the NV configuration. The electric stresses showed no change with De as the flow field did not affect it. The viscous and viscoelastic stresses for both configurations were calculated to understand the reduced and non-monotonic nature of the deformation.

Chapter 7

Conclusions and scope for future work

In this thesis, the drop-drop and drop-surface dynamics during impact and electrohydrodynamic interactions have been investigated. We utilized an in-house coupled level set and volume of fluid (CLSVOF) method based solver and an open-source solver Basilisk for the computational studies. This chapter summarizes the main results of the investigations and the conclusions drawn (§ 7.1). Furthermore, we identified some areas which require more investigation for a complete understanding of the interaction dynamics. Those have been listed at the end of this chapter (§ 7.2).

7.1 Conclusions

We provided a detailed literature review of the past work on drop impact dynamics and electrohydrodynamics. Based on the literature gap, we provided the objectives for the present thesis. The studies in this thesis are solely based on numerical simulations. We describe the two computational tools utilized for the studies. The details of an in-house solver based on the CLSVOF method and an open-source solver Basilisk are presented. The governing equations and their discretizations are shown. The numerical schemes used and the algorithm of the solver are described in detail. The spatial discretization and the grid used to discretize the domain are presented.

The culmination of a series of phenomena during the impact of a water drop on a deep pool of water. The evolution of the outward jets that form during the collapse of the crater can produce secondary drops. Stronger radial flow produces a more elongated jet. The jet emanates as a consequence of the flow rate imposed by the

radial velocity field induced by the crater walls. As the impact velocity increases, larger cavities result, followed by various jet dynamics and variations of drop sizes. When the crater reaches maximum depth, inertia becomes less significant, and surface tension governs the receding motion of the crater. Capillary effects are responsible for the formation of the wave swell at the crater mouth (Ray et al., 2015). During the collapse of the crater, the capillary waves from the top of the cavity propagate and focus at the bottom (Deike et al., 2018; Woodcock et al., 1953). As a part of capillary retraction dynamics, these waves also deform the bottom of the cavity from which the jet is issued. The liquid jet moves up vertically and grows due to a symmetric rush of radial velocity from liquid inventory. As the Weber number increases, the jet height increases (Ray et al., 2012). Having reached a critical height, the jet sheds drops to release high surface energy, and the remaining part of the ejected liquid recoils back into the reservoir. As mentioned, the evolution of the outward jets that form during collapse of the crater produces secondary drops. The dimensionless jet velocity can be expressed as a function of Froude number, Weber number, and the minimum radius of the cavity. Depending on Fr and We, three different scenarios emerge together with the formation of a central jet and the pinch-off of one or more secondary drops. At low impact velocities, a long thick central jet is formed, finally leading to the formation of a secondary drop which is always smaller than the initial drop. For moderate impact velocities still, a long jet emanates, which is, much thinner than in the previous case entailing the breakup of the jet into multiple secondary drops, which are all smaller than the initial drop. In the third paradigm of very high impact velocities, which was clearly identified here for the first time, the emanating jet is long and thick, leading to the pinch-off of a secondary drop, which has a larger diameter than the initial drop. Similar to the case with a long thick jet and a singular secondary drop smaller than the initial drop, in this new regime with an evolving larger drop than the original one, linear relations are observed for the pinch-off time and the maximum jet height as a function of the Froude number.

The interaction dynamics of a pair of drops in a uniform electric field is numerically investigated. A leaky dielectric model is utilized for this study, with the core and the ambient phase being the same and the shell of the compound drop being different. We note that the stability of a compound drop as well the relative motion between a pair of drops, depends essentially on the charge relaxation time constant ratio of the ambient and the outer shell of the compound drop (τ_e^1/τ_e^2) or equivalently the ratio of Q/R. This parameter describes the sign of the charge that develops at the drop interface and,

thus, the sense of the flow circulation generated due to the tangential electric stresses. If the flow is from the poles to the equator in the ambient fluid, it implies that the flow in the outer shell is from the center toward the pole. The flow generated in the ambient indicates a hydrodynamic drag on the neighboring drop, thus driving the two drops together and making the emulsion unstable. Also, due to the flow inside the outer shell of the compound drop being from the center towards the pole, any deviation of the inner drop from the center of the compound drop would result in a hydrodynamic drag that will drive the inner drop toward the ambient fluid. We show that this simple rule of thumb is not applicable when the inertial forces are accounted for. Despite the vital role played by the hydrodynamic forces governed by the strength of the electric field Ca_E and the ratio of charge relaxation time constants τ_e^1/τ_e^2, we observed that for lower values of Reynolds number, Re, electrostatic dipole-dipole forces can modify certain features of the interaction dynamics. The apriori expectation of the stability of an emulsion in an electric field would require consideration of the relative time scales of electrostatic attraction, charge relaxation, and flow time scale. Moreover, the relative strength of the electrostatic and hydrodynamic forces, given by the ratio F_e/F_h in Equation (4.9), also determines the interaction dynamics of the drops. For low F_e/F_h, hydrodynamic forces govern the motion of the drops, and the velocity of approach varies as $1/h^2$, whereas for higher F_e/F_h, electrostatic forces are dominant and the velocity of approach varies as $1/h^4$. We believe that this study would motivate some more experiments in regimes that show interesting dynamics of the drops, such as the formation of a drop-drop doublet.

In the earlier work, we saw a new phenomenon of non-coalescence in which the drops were attracted toward each other but did not coalesce. Instead, a stable thin film was formed between the drops. A pair of single emulsion leaky-dielectric drops suspended in a leaky-dielectric medium is considered for this study. Only the effect of conductivity and permittivity ratios are investigated for the interaction dynamics. All other properties and dimensionless parameters are kept constant. The previous investigation by Baygents et al. (1998) studied the drop pair dynamics using creeping flow approximations. Their study defined a map that showed drops could either move apart or come close. We revisited this same work, but instead, we solved the full Navier-Stokes equations using a finite Reynolds number. Based on the simulations, we identified a different regime for drop interaction dynamics. Electrostatic forces are always attractive, but the hydrodynamic forces due to the circulation flow generated by the electrical stresses at the drop interfaces can determine the nature of the interaction.

An estimate of the ratio of hydrodynamic forces and electrostatic forces is obtained to determine the nature of the interaction dynamics of a pair of drops. This ratio of forces enabled us to delineate the different regimes for interaction. Finally, we provide a phase map for the interaction dynamics based on the conductivity and permittivity ratios. The theoretically obtained limiting lines match well with the computational results. We found three regimes where the drops can come together and coalesce, the drops can move apart, and the drops come together and form a thin film without coalescing. The several new regimes for leaky-dielectric drops representing the thin film formation obtained here have been observed in experiments but have not been observed in earlier numerical studies since they were performed in the Stokes limit.

We study the effects of viscoelasticity in the presence of an electric field in a two-dimensional axisymmetric configuration. Viscoelastic studies for drop deformation were conducted only in the context of shear and extensional flows. The effect of the electric field on viscoelasticity is studied numerically using the open-source solver. Two configurations are selected for the study. A viscoelastic drop suspended in a Newtonian ambient (VN) and a Newtonian drop suspended in a viscoelastic matrix (NV). We only study the effect of Deborah number using the Oldroyd-B constitutive model. All other properties, including the electrical properties, are kept constant. The conductivity and permittivity ratios are taken such that the drop deforms prolately. The transient drop dynamics show oscillations for viscoelastic fluids. This is attributed to the nonlinear nature of the Oldroyd-B constitutive equation, which gives rise to a finite first normal stress difference. The steady-state deformation shows a significant effect of viscoelasticity. A normalized deformation is plotted against the De. The electric stresses only depend on the electrical properties and the electric field strength. Hence they do not change with the flow field and do not modify the drop deformation. For the VN configuration, drop deformation decreased with an increase in De. We observe that the viscoelastic normal stress at the poles decreases the axial length, and the viscoelastic tangential stress at the equator increases the length perpendicular to the axis. This interplay of viscoelastic stress causes an overall reduction in drop deformation with increasing De. The deformation dynamics showed a non-monotonic nature for the NV configuration. We observe an overall monotonic increase in axial length due to the viscoelastic normal stresses, and the length of the transverse axis changes non-monotonically. This is due to decreasing viscous stress but increasing viscoelastic stress at the poles of the drop, which results in a non-monotonic behavior

of drop deformation with De. Further investigations on drop breakup can be conducted to understand the stability of these systems.

7.2 Scope of future work

The present dissertation explored the drop dynamics in the purview of impact and coalescence. A significant portion of the physical dynamics still needs to be analyzed to understand the practical applications better. The possible extensions of the current work as future scope are mentioned below.

- Drop dynamics in electrohydrodynamic flows are affected by viscosity contrast between the phases. Investigations into this parameter will reveal important flow features.
- A non-uniform electric field (AC) leads to drop dynamics that depend on the frequency of the flow field. Studies can be conducted to understand the effect of oscillating flow fields.
- With the advent of digital microfluidics, the application of electromagnetic fields is gaining interest. The drop dynamics in such investigations may lose their symmetrical nature. Full three-dimensional studies should be conducted to analyze such systems.
- The drop deformation will depend on the solvent viscosity ratio and the viscoelasticity in both phases. The inclusion of such parameters will demonstrate the effect of polymeric fluids.

References

Abbasi, M. S., Ali, H., Kazim, A. H., Chaudhary, T. N., Usman, M., Afzaal, S., Usman, M., and Abalo, D. (2022). Emulsion Droplet Pair Coalescence under a Direct Current Electric Field. *Mathematical Problems in Engineering*, 2022:1–9.

Abbasi, M. S., Song, R., Kim, J., and Lee, J. (2017). Electro-hydrodynamic behavior and interface instability of double emulsion droplets under high electric field. *Journal of Electrostatics*, 85:11–22.

Abbasi, M. S., Song, R., Kim, S. M., Kim, H., and Lee, J. (2019a). Mono-emulsion droplet stretching under direct current electric field. *Soft Matter*, 15(11):2328–2335.

Abbasi, M. S., Song, R., and Lee, J. (2019b). Breakups of an encapsulated surfactant-laden aqueous droplet under a DC electric field. *Soft Matter*, 15(43):8905–8911.

Agbaglah, G., Thoraval, M.-J., Thoroddsen, S. T., Zhang, L. V., Fezzaa, K., and Deegan, R. D. (2015). Drop impact into a deep pool: vortex shedding and jet formation. *Journal of Fluid Mechanics*, 764:R1.

Aggarwal, N. and Sarkar, K. (2007). Deformation and breakup of a viscoelastic drop in a Newtonian matrix under steady shear. *Journal of Fluid Mechanics*, 584:1–21.

Aggarwal, N. and Sarkar, K. (2008). Effects of matrix viscoelasticity on viscous and viscoelastic drop deformation in a shear flow. *Journal of Fluid Mechanics*, 601:63–84.

Ajayi, O. O. (1978). A note on Taylor's electrohydrodynamic theory. *Proceedings of the Royal Society of London. A. Mathematical and Physical Sciences*, 364(1719):499–507.

Allan, R. S. and Mason, S. G. (1962). Particle behaviour in shear and electric fields I. Deformation and burst of fluid drops. *Proceedings of the Royal Society of London. Series A. Mathematical and Physical Sciences*, 267(1328):45–61.

Anand, V., Juvekar, V. A., and Thaokar, R. M. (2019). Modes of coalescence of aqueous anchored drops in insulating oils under an electric field. *Colloids and Surfaces A: Physicochemical and Engineering Aspects*, 568:294–300.

Anand, V., Juvekar, V. A., and Thaokar, R. M. (2020). Coalescence, Partial Coalescence, and Noncoalescence of an Aqueous Drop at an Oil-Water Interface under an Electric Field. *Langmuir*, 36(21):6051–6060.

Arp, P. A., Foister, R. T., and Mason, S. G. (1980). Some electrohydrodynamic effects in fluid dispersions. *Advances in Colloid and Interface Science*, 12(4):295–356.

Arp, P. A. and Mason, S. G. (1977). Particle behaviour in shear and electric fields. *Colloid and Polymer Science*, 255(10):980–993.

Aryafar, H. and Kavehpour, P. (2006). Drop coalescence through planar surfaces. *Physics of Fluids*, 18(7):72105.

Aryafar, H. and Kavehpour, P. (2007). Electrocoalescence. *Physics of Fluids*, 19(9).

Atten, P. (1993). Electrocoalescence of water droplets in an insulating liquid. *Journal of Electrostatics*, 30(C):259–269.

Azarmanesh, M., Farhadi, M., and Azizian, P. (2015). Simulation of the double emulsion formation through a hierarchical T-junction microchannel. *International Journal of Numerical Methods for Heat and Fluid Flow*, 25(7):1705–1717.

Bailes, P., Lee, J., and Parsons, A. (2000). An Experimental Investigation into the Motion of a Single Drop in a Pulsed DC Electric Field. *Chemical Engineering Research and Design*, 78(3):499–505.

Barnes, H. A. (1994). Rheology of emulsions — a review. *Colloids and Surfaces A: Physicochemical and Engineering Aspects*, 91(C):89–95.

Batchelor, G. K. (2000). *An Introduction to Fluid Dynamics*. Cambridge University Press.

Baygents, J. C., Rivette, N. J., and Stone, H. A. (1998). Electrohydrodynamic deformation and interaction of drop pairs. *Journal of Fluid Mechanics*, 368:359–375.

Behera, N., Mandal, S., and Chakraborty, S. (2019). Electrohydrodynamic settling of drop in uniform electric field: beyond Stokes flow regime. *Journal of Fluid Mechanics*, 881:498–523.

Behjatian, A. and Esmaeeli, A. (2013). Electrohydrodynamics of a compound drop. *Physical Review E - Statistical, Nonlinear, and Soft Matter Physics*, 88(3):033012.

Behjatian, A. and Esmaeeli, A. (2015). Transient electrohydrodynamics of compound drops. *Acta Mechanica*, 226(8):2581–2606.

Bell, J. B., Colella, P., and Glaz, H. M. (1989). A second-order projection method for the incompressible navier-stokes equations. *Journal of Computational Physics*, 85(2):257–283.

Bentenitis, N. and Krause, S. (2005). Droplet deformation in DC electric fields: The extended leaky dielectric model. *Langmuir*, 21(14):6194–6209.

Berny, A., Deike, L., Séon, T., and Popinet, S. (2020). Role of all jet drops in mass transfer from bursting bubbles. *Physical Review Fluids*, 5(3):033605.

Bird, J. C., Ristenpart, W. D., Belmonte, A., and Stone, H. A. (2009). Critical angle for electrically driven coalescence of two conical droplets. *Physical Review Letters*, 103(16):164502.

Bird, R. B., Armstrong, R. C., and Hassager, O. (1987a). *Dynamics of polymeric liquids. Vol. 1: Fluid mechanics*. John Wiley and Sons Inc., New York, NY.

Bird, R. B., Armstrong, R. C., and Hassager, O. (1987b). *Dynamics of polymeric liquids. Vol. 2: Kinetic theory*. John Wiley and Sons Inc., New York, NY.

Blanchette, F. and Bigioni, T. P. (2006). Partial coalescence of drops at liquid interfaces. *Nature Physics*, 2(4):254–257.

Borthakur, M. P., Nath, B., and Biswas, G. (2021). Dynamics of a compound droplet under the combined influence of electric field and shear flow. *Physical Review Fluids*, 6(2):023603.

Boyko, E. and Stone, H. A. (2022). Pressure-driven flow of the viscoelastic Oldroyd-B fluid in narrow non-uniform geometries: analytical results and comparison with simulations. *Journal of Fluid Mechanics*, 936:A23.

Brackbill, J. U., Kothe, D. B., and Zemach, C. (1992). A continuum method for modeling surface tension. *Journal of Computational Physics*, 100(2):335–354.

Brazier-Smith, P. R. (1971). Stability and Shape of Isolated and Pairs of Water Drops in an Electric Field. *The Physics of Fluids*, 14(1):1–6.

Brosseau, Q. and Vlahovska, P. M. (2017). Streaming from the Equator of a Drop in an External Electric Field. *Physical Review Letters*, 119(3):034501.

Castillo-Orozco, E., Davanlou, A., Choudhury, P. K., and Kumar, R. (2015). Droplet impact on deep liquid pools: Rayleigh jet to formation of secondary droplets. *Physical Review E - Statistical, Nonlinear, and Soft Matter Physics*, 92(5):053022.

Chang, Y. C., Hou, T. Y., Merriman, B., and Osher, S. (1996). A Level Set Formulation of Eulerian Interface Capturing Methods for Incompressible Fluid Flows. *Journal of Computational Physics*, 124(2):449–464.

Charles, G. E. and Mason, S. G. (1960). The mechanism of partial coalescence of liquid drops at liquid/liquid interfaces. *Journal of Colloid Science*, 15(2):105–122.

Chen, T., Mohammed, R., Bailey, A., Luckham, P., and Taylor, S. (1994). Dewatering of crude oil emulsions 4. Emulsion resolution by the application of an electric field. *Colloids and Surfaces A: Physicochemical and Engineering Aspects*, 83(3):273–284.

Chen, X., Mandre, S., and Feng, J. J. (2006). Partial coalescence between a drop and a liquid-liquid interface. *Physics of Fluids*, 18(5):51705.

Chung, C., Kim, J. M., Hulsen, M. A., Ahn, K. H., and Lee, S. J. (2009). Effect of viscoelasticity on drop dynamics in 5:1:5 contraction/expansion microchannel flow. *Chemical Engineering Science*, 64(22):4515–4524.

Chung, J. N. and Oliver, D. L. (1990). Transient Heat Transfer in a Fluid Sphere Translating in an Electric Field. *Journal of Heat Transfer*, 112(1):84–91.

Collins, R. T., Sambath, K., Harris, M. T., and Basaran, O. A. (2013). Universal scaling laws for the disintegration of electrified drops. *Proceedings of the National Academy of Sciences*, 110(13):4905–4910.

Coppola, G., Rocco, G., and de Luca, L. (2011). Insights on the impact of a plane drop on a thin liquid film. *Physics of Fluids*, 23(2):22105.

Das, D. and Saintillan, D. (2017a). A nonlinear small-deformation theory for transient droplet electrohydrodynamics. *Journal of Fluid Mechanics*, 810:225–253.

Das, D. and Saintillan, D. (2017b). Electrohydrodynamics of viscous drops in strong electric fields: numerical simulations. *Journal of Fluid Mechanics*, 829:127–152.

Deike, L., Ghabache, E., Liger-Belair, G., Das, A. K., Zaleski, S., Popinet, S., and Séon, T. (2018). Dynamics of jets produced by bursting bubbles. *Physical Review Fluids*, 3(1):013603.

Deka, H., Ray, B., Biswas, G., Dalal, A., Tsai, P. H., and Wang, A. B. (2017). The regime of large bubble entrapment during a single drop impact on a liquid pool. *Physics of Fluids*, 29(9).

Dezhi, S., Shik Chung, J., Xiaodong, D., and Ding, Z. (1999). Demulsification of water-in-oil emulsion by wetting coalescence materials in stirred- and packed-columns. *Colloids and Surfaces A: Physicochemical and Engineering Aspects*, 150(1-3):69–75.

Dong, Q. and Sau, A. (2018). Electrohydrodynamic interaction, deformation, and coalescence of suspended drop pairs at varied angle of incidence. *Physical Review Fluids*, 7(3):073701.

Durst, F. (1996). Penetration length and diameter development of vortex rings generated by impacting water drops. *Experiments in Fluids*, 21(2):110–117.

Elmendorp, J. J. (1986). A study on polymer blending microrheology. *Polymer Engineering and Science*, 26(6):418–426.

Enayati, M., Ahmad, Z., Stride, E., and Edirisinghe, M. (2010). One-step electrohydrodynamic production of drug-loaded micro- and nanoparticles. *Journal of The Royal Society Interface*, 7(45):667–675.

Enayati, M., Chang, M.-W., Bragman, F., Edirisinghe, M., and Stride, E. (2011). Electrohydrodynamic preparation of particles, capsules and bubbles for biomedical engineering applications. *Colloids and Surfaces A: Physicochemical and Engineering Aspects*, 382(1-3):154–164.

Engel, O. G. (1967). Initial Pressure, Initial Flow Velocity, and the Time Dependence of Crater Depth in Fluid Impacts. *Journal of Applied Physics*, 38(10):3935–3940.

Eow, J. S. and Ghadiri, M. (2002). Electrostatic enhancement of coalescence of water droplets in oil: a review of the technology. *Chemical Engineering Journal*, 85(2-3):357–368.

Eow, J. S. and Ghadiri, M. (2003). The behaviour of a liquid–liquid interface and drop-interface coalescence under the influence of an electric field. *Colloids and Surfaces A: Physicochemical and Engineering Aspects*, 215(1-3):101–123.

Eow, J. S., Ghadiri, M., and Sharif, A. (2001). Deformation and break-up of aqueous drops in dielectric liquids in high electric fields. *Journal of Electrostatics*, 51-52(1-4):463–469.

Fattal, R. and Kupferman, R. (2004). Constitutive laws for the matrix-logarithm of the conformation tensor. *Journal of Non-Newtonian Fluid Mechanics*, 123(2-3):281–285.

Fedorchenko, A. I. and Wang, A. B. (2004). On some common features of drop impact on liquid surfaces. *Physics of Fluids*, 16(5):1349–1365.

Feng, J. Q. (1999). Electrohydrodynamic behaviour of a drop subjected to a steady uniform electric field at finite electric Reynolds number. *Proceedings of the Royal Society of London. Series A: Mathematical, Physical and Engineering Sciences*, 455(1986):2245–2269.

Feng, J. Q. and Scott, T. C. (1996). A computational analysis of electrohydrodynamics of a leaky dielectric drop in an electric field. *Journal of Fluid Mechanics*, 311:289–326.

Fernández, A. (2008a). Response of an emulsion of leaky dielectric drops immersed in a simple shear flow: Drops less conductive than the suspending fluid. *Physics of Fluids*, 20(4).

Fernández, A. (2008b). Response of an emulsion of leaky dielectric drops immersed in a simple shear flow: Drops more conductive than the suspending fluid. *Physics of Fluids*, 20(4).

Figueiredo, R., Oishi, C., Afonso, A., Tasso, I., and Cuminato, J. (2016). A two-phase solver for complex fluids: Studies of the Weissenberg effect. *International Journal of Multiphase Flow*, 84:98–115.

Flumerfelt, R. W. (1972). Drop Breakup in Simple Shear Fields of Viscoelastic Fluids. *Industrial and Engineering Chemistry Fundamentals*, 11(3):312–318.

Francois, M. M., Cummins, S. J., Dendy, E. D., Kothe, D. B., Sicilian, J. M., and Williams, M. W. (2006). A balanced-force algorithm for continuous and sharp interfacial surface tension models within a volume tracking framework. *Journal of Computational Physics*, 213(1):141–173.

Funfschilling, D. and Li, H. Z. (2001). Flow of non-Newtonian fluids around bubbles: PIV measurements and birefringence visualisation. *Chemical Engineering Science*, 56(3):1137–1141.

Gañán-Calvo, A. M., López-Herrera, J. M., Herrada, M. A., Ramos, A., and Montanero, J. M. (2018). Review on the physics of electrospray: From electrokinetics to the operating conditions of single and coaxial Taylor cone-jets, and AC electrospray. *Journal of Aerosol Science*, 125:32–56.

Garton, C. G. and Krasucki, Z. (1964). Bubbles in insulating liquids: stability in an electric field. *Proceedings of the Royal Society of London. Series A. Mathematical and Physical Sciences*, 280(1381):211–226.

Gauthier, F., Goldsmith, H. L., and Mason, S. G. (1971). Particle Motions in Non-Newtonian Media. II. Poiseuille Flow. *Transactions of the Society of Rheology*, 15(2):297–330.

Gerlach, D., Tomar, G., Biswas, G., and Durst, F. (2006). Comparison of volume-of-fluid methods for surface tension-dominant two-phase flows. *International Journal of Heat and Mass Transfer*, 49(3-4):740–754.

Ghasemi, E., Bararnia, H., Soleimanikutanaei, S., and Lin, C. (2018). Simulation of deformation and fragmentation of a falling drop under electric field. *Powder Technology*, 325:301–308.

Gilet, T., Mulleners, K., Lecomte, J. P., Vandewalle, N., and Dorbolo, S. (2007). Critical parameters for the partial coalescence of a droplet. *Physical Review E - Statistical, Nonlinear, and Soft Matter Physics*, 75(3):036303.

Goodarzi, F. and Zendehboudi, S. (2019). A Comprehensive Review on Emulsions and Emulsion Stability in Chemical and Energy Industries. *The Canadian Journal of Chemical Engineering*, 97(1):281–309.

Gouz, H. N. and Sadhal, S. S. (1989). Fluid dynamics and stability analysis of a compound droplet in an electric field. *The Quarterly Journal of Mechanics and Applied Mathematics*, 42(1):65–83.

Greco, F. (2002). Drop deformation for non-Newtonian fluids in slow flows. *Journal of Non-Newtonian Fluid Mechanics*, 107(1-3):111–131.

Grmela, M. and Carreau, P. (1987). Conformation tensor rheological models. *Journal of Non-Newtonian Fluid Mechanics*, 23(C):271–294.

Guido, S., Simeone, M., and Greco, F. (2003). Deformation of a Newtonian drop in a viscoelastic matrix under steady shear flow Experimental validation of slow flow theory. *Journal of Non-Newtonian Fluid Mechanics*, 114(1):65–82.

Ha, J. W. and Yang, S. M. (1999a). Breakup of a Multiple Emulsion Drop in a Uniform Electric Field. *Journal of Colloid and Interface Science*, 213(1):92–100.

Ha, J. W. and Yang, S. M. (1999b). Fluid dynamics of a double emulsion droplet in an electric field. *Physics of Fluids*, 11(5):1029–1041.

Ha, J. W. and Yang, S. M. (2000a). Deformation and breakup of Newtonian and non-Newtonian conducting drops in an electric field. *Journal of Fluid Mechanics*, 405:131–156.

Ha, J. W. and Yang, S. M. (2000b). Electrohydrodynamics and electrorotation of a drop with fluid less conductive than that of the ambient fluid. *Physics of Fluids*, 12(4):764–772.

Hao, J. and Pan, T.-W. (2007). Simulation for high Weissenberg number. *Applied Mathematics Letters*, 20(9):988–993.

Harlow, F. H. and Welch, J. E. (1965). Numerical Calculation of Time-Dependent Viscous Incompressible Flow of Fluid with Free Surface. *Physics of Fluids*, 8(12):2182.

Harvie, D. J., Cooper-White, J. J., and Davidson, M. R. (2008). Deformation of a viscoelastic droplet passing through a microfluidic contraction. *Journal of Non-Newtonian Fluid Mechanics*, 155(1-2):67–79.

Herrera-Velarde, J. R., Zenit, R., Chehata, D., and Mena, B. (2003). The flow of non-Newtonian fluids around bubbles and its connection to the jump discontinuity. *Journal of Non-Newtonian Fluid Mechanics*, 111(2-3):199–209.

Hirt, C. and Nichols, B. (1981). Volume of fluid (VOF) method for the dynamics of free boundaries. *Journal of Computational Physics*, 39(1):201–225.

Holto, J., Berg, G., and Lundgaard, L. E. (2009). Electrocoalescence of drops in a water-in-oil emulsion. In *2009 IEEE Conference on Electrical Insulation and Dielectric Phenomena*, pages 196–199. IEEE.

Honey, E. M. and Kavehpour, H. P. (2006). Astonishing life of a coalescing drop on a free surface. *Physical Review E - Statistical, Nonlinear, and Soft Matter Physics*, 73(2):027301.

Hooper, R. W., De Almeida, V. F., Macosko, C. W., and Derby, J. J. (2001). Transient polymeric drop extension and retraction in uniaxial extensional flows. *Journal of Non-Newtonian Fluid Mechanics*, 98(2-3):141–168.

Huang, X., He, L., Luo, X., Xu, K., Lü, Y., and Yang, D. (2020). Coalescence, Partial Coalescence, and Noncoalescence of Two Free Droplets Suspended in Low-Viscosity Oil under a DC Electric Field. *Journal of Physical Chemistry B*, 124(34):7508–7517.

Hulsen, M. A., Fattal, R., and Kupferman, R. (2005). Flow of viscoelastic fluids past a cylinder at high Weissenberg number: Stabilized simulations using matrix logarithms. *Journal of Non-Newtonian Fluid Mechanics*, 127(1):27–39.

Jiang, Z., Gan, Y., and Luo, Y. (2020). Effect of viscosity ratio on the dynamic response of droplet deformation under a steady electric field. *Physics of Fluids*, 32(5).

Kane, A., Guénette, R., and Fortin, A. (2009). A comparison of four implementations of the log-conformation formulation for viscoelastic fluid flows. *Journal of Non-Newtonian Fluid Mechanics*, 164(1-3):45–50.

Kavehpour, H. P. (2015). Coalescence of Drops. *Annual Review of Fluid Mechanics*, 47(1):245–268.

Kilpatrick, P. K. (2012). Water-in-crude oil emulsion stabilization: Review and unanswered questions. *Energy and Fuels*, 26(7):4017–4026.

Kim, D., Lee, J., Bose, A., Kim, I., and Lee, J. (2021). The impact of an oil droplet on an oil layer on water. *Journal of Fluid Mechanics*, 906:A5.

Klasson, K. T., Taylor, P. A., Walker, J. F., Jones, S. A., Cummins, R. L., and Richardson, S. A. (2005). Modification of a Centrifugal Separator for In-Well Oil-Water Separation. *Separation Science and Technology*, 40(1-3):453–462.

Knechtges, P., Behr, M., and Elgeti, S. (2014). Fully-implicit log-conformation formulation of constitutive laws. *Journal of Non-Newtonian Fluid Mechanics*, 214:78–87.

Lac, E. and Homsy, G. M. (2007). Axisymmetric deformation and stability of a viscous drop in a steady electric field. *Journal of Fluid Mechanics*, 590:239–264.

Lanauze, J. A., Walker, L. M., and Khair, A. S. (2013). The influence of inertia and charge relaxation on electrohydrodynamic drop deformation. *Physics of Fluids*, 25(11):112101.

Lanauze, J. A., Walker, L. M., and Khair, A. S. (2015). Nonlinear electrohydrodynamics of slightly deformed oblate drops. *Journal of Fluid Mechanics*, 774:245–266.

Larson, R. G. (1988). *Constitutive equations for polymer melts and solutions*. Butterworths.

Latham, J. and Roxburgh, I. W. (1966). Disintegration of pairs of water drops in an electric field. *Proceedings of the Royal Society of London. Series A. Mathematical and Physical Sciences*, 295(1440):84–97.

Lee, J., Hwang, W. R., and Cho, K. S. (2021). Effect of stress diffusion on the Oldroyd-B fluid flow past a confined cylinder. *Journal of Non-Newtonian Fluid Mechanics*, 297:104650.

Leng, L. J. (2001). Splash formation by spherical drops. *Journal of Fluid Mechanics*, 427:73–105.

Li, Y. and Cheng, J. (2023). Modeling liquid droplet impact on a micropillar-arrayed viscoelastic surface via mechanically averaged responses. *Engineering Applications of Computational Fluid Mechanics*, 17(1):2194949.

Lima, N. C. and D'Ávila, M. A. (2014). Numerical simulation of electrohydrodynamic flows of Newtonian and viscoelastic droplets. *Journal of Non-Newtonian Fluid Mechanics*, 213:1–14.

Lin, Y., Skjetne, P., and Carlson, A. (2012). A phase field model for multiphase electro-hydrodynamic flow. *International Journal of Multiphase Flow*, 45:1–11.

Lind, S. J. and Phillips, T. N. (2010). The effect of viscoelasticity on a rising gas bubble. *Journal of Non-Newtonian Fluid Mechanics*, 165(15-16):852–865.

López-Herrera, J., Popinet, S., and Castrejón-Pita, A. (2019). An adaptive solver for viscoelastic incompressible two-phase problems applied to the study of the splashing of weakly viscoelastic droplets. *Journal of Non-Newtonian Fluid Mechanics*, 264:144–158.

López-Herrera, J. M., Popinet, S., and Herrada, M. A. (2011). A charge-conservative approach for simulating electrohydrodynamic two-phase flows using volume-of-fluid. *Journal of Computational Physics*, 230(5):1939–1955.

Ma, H., Liu, C., Li, X., Huang, H., and Dong, J. (2019). Deformation characteristics and energy conversion during droplet impact on a water surface. *Physics of Fluids*, 31(6).

Ma, J., Wang, Z., Young, J., Lai, J. C., Sui, Y., and Tian, F.-B. (2020). An immersed boundary-lattice Boltzmann method for fluid-structure interaction problems involving viscoelastic fluids and complex geometries. *Journal of Computational Physics*, 415:109487.

Maffettone, P. L. and Greco, F. (2004). Ellipsoidal drop model for single drop dynamics with non-Newtonian fluids. *Journal of Rheology*, 48(1):83–100.

Manzello, S. L. and Yang, J. C. (2002). An experimental study of a water droplet impinging on a liquid surface. *Experiments in Fluids*, 32(5):580–589.

Medwin, H., Kurgan, A., and Nystuen, J. A. (1990). Impact and bubble sound from raindrops at normal and oblique incidence. *The Journal of the Acoustical Society of America*, 88(1):413–418.

Melcher, J. R. and Taylor, G. I. (1969). Electrohydrodynamics: A Review of the Role of Interfacial Shear Stresses. *Annual Review of Fluid Mechanics*, 1(1):111–146.

Mhatre, S., Deshmukh, S., and Thaokar, R. M. (2015a). Electrocoalescence of a drop pair. *Physics of Fluids*, 27(9).

Mhatre, S., Vivacqua, V., Ghadiri, M., Abdullah, A., Al-Marri, M., Hassanpour, A., Hewakandamby, B., Azzopardi, B., and Kermani, B. (2015b). Electrostatic phase separation: A review. *Chemical Engineering Research and Design*, 96:177–195.

Michon, G. J., Josserand, C., and Séon, T. (2017). Jet dynamics post drop impact on a deep pool. *Physical Review Fluids*, 2(2):023601.

Midtgård, O.-M. (2012). Application of circuit theory for extraction of water from oil. *International Journal of Circuit Theory and Applications*, 40(9):927–942.

Mighri, F., Ajji, A., and Carreau, P. J. (1997). Influence of elastic properties on drop deformation in elongational flow. *Journal of Rheology*, 41(5):1183–1201.

Mighri, F., Carreau, P. J., and Ajji, A. (1998). Influence of elastic properties on drop deformation and breakup in shear flow. *Journal of Rheology*, 42(6):1477–1490.

Minale, M. (2004). Deformation of a non-Newtonian ellipsoidal drop in a non-Newtonian matrix: extension of Maffettone–Minale model. *Journal of Non-Newtonian Fluid Mechanics*, 123(2-3):151–160.

Mohammed, R., Bailey, A., Luckham, P., and Taylor, S. (1993). Dewatering of crude oil emulsions 2. Interfacial properties of the asphaltic constituents of crude oil. *Colloids and Surfaces A: Physicochemical and Engineering Aspects*, 80(2-3):237–242.

Morrison, F. A. (2001). *Understanding Rheology*. Oxford University Press.

Morton, D., Rudman, M., and Leng, L. J. (2000). An investigation of the flow regimes resulting from splashing drops. *Physics of Fluids*, 12(4):747–763.

Notz, P. K. and Basaran, O. A. (1999). Dynamics of Drop Formation in an Electric Field. *Journal of Colloid and Interface Science*, 213(1):218–237.

O'Konski, C. T. and Thacher, H. C. (1953). The distortion of aerosol droplets by an electric field. *Journal of Physical Chemistry*, 57(9):955–958.

Oldroyd, J. G. (1950). On the formulation of rheological equations of state. *Proceedings of the Royal Society of London. Series A. Mathematical and Physical Sciences*, 200(1063):523–541.

Osher, S. and Sethian, J. A. (1988). Fronts propagating with curvature-dependent speed: Algorithms based on Hamilton-Jacobi formulations. *Journal of Computational Physics*, 79(1):12–49.

Owens, R. G. and Phillips, T. N. (2002). *Computational Rheology*. World Scientific Publishing Company.

Pearce, C. A. R. (1954). The mechanism of the resolution of water-in-oil emulsions by electrical treatment. *British Journal of Applied Physics*, 5(4):136–143.

Penkova, A., Pan, W., Hodjaoglu, F., and Vekilov, P. G. (2006). Nucleation of Protein Crystals under the Influence of Solution Shear Flow. *Annals of the New York Academy of Sciences*, 1077(1):214–231.

Phillips, T. N. and Roberts, G. W. (2011). Lattice Boltzmann models for non-Newtonian flows. *IMA Journal of Applied Mathematics*, 76(5):790–816.

Pillapakkam, S. B., Singh, P., Blackmore, D., and Aubry, N. (2007). Transient and steady state of a rising bubble in a viscoelastic fluid. *Journal of Fluid Mechanics*, 589:215–252.

Pohl, H. A. and Crane, J. S. (1971). Dielectrophoresis of Cells. *Biophysical Journal*, 11(9):711–727.

Popinet, S. (2003). Gerris: a tree-based adaptive solver for the incompressible Euler equations in complex geometries. *Journal of Computational Physics*, 190(2):572–600.

Popinet, S. (2009). An accurate adaptive solver for surface-tension-driven interfacial flows. *Journal of Computational Physics*, 228(16):5838–5866.

Popinet, S. (2015). A quadtree-adaptive multigrid solver for the Serre–Green–Naghdi equations. *Journal of Computational Physics*, 302:336–358.

Popinet, S. (2018). Numerical Models of Surface Tension. *Annual Review of Fluid Mechanics*, 50(1):49–75.

Priti Sinha, K., Das, S., Karyappa, R. B., and Thaokar, R. M. (2020). Electrohydrodynamics of Vesicles and Capsules. *Langmuir*, 36(18):4863–4886.

Prosperetti, A. and Tryggvason, G. (2007). *Computational Methods for Multiphase Flow*, volume 9780521847. Cambridge University Press.

Puckett, E. G., Almgren, A. S., Bell, J. B., Marcus, D. L., and Rider, W. J. (1997). A High-Order Projection Method for Tracking Fluid Interfaces in Variable Density Incompressible Flows. *Journal of Computational Physics*, 130(2):269–282.

Pumphrey, H. C. and Elmore, P. A. (1990). The entrainment of bubbles by drop impacts. *Journal of Fluid Mechanics*, 220:539–567.

Ramaswamy, S. and Leal, L. G. (1999a). The deformation of a Newtonian drop in the uniaxial extensional flow of a viscoelastic liquid. *Journal of Non-Newtonian Fluid Mechanics*, 88(1-2):149–172.

Ramaswamy, S. and Leal, L. G. (1999b). The deformation of a viscoelastic drop subjected to steady uniaxial extensional flow of a Newtonian fluid. *Journal of Non-Newtonian Fluid Mechanics*, 85(2-3):127–163.

Ray, B., Biswas, G., and Sharma, A. (2010). Generation of secondary droplets in coalescence of a drop at a liquid–liquid interface. *Journal of Fluid Mechanics*, 655:72–104.

Ray, B., Biswas, G., and Sharma, A. (2012). Bubble pinch-off and scaling during liquid drop impact on liquid pool. *Physics of Fluids*, 24(8).

Ray, B., Biswas, G., and Sharma, A. (2015). Regimes during liquid drop impact on a liquid pool. *Journal of Fluid Mechanics*, 768:492–523.

Rayleigh, L. (1882). XX. On the equilibrium of liquid conducting masses charged with electricity. *The London, Edinburgh, and Dublin Philosophical Magazine and Journal of Science*, 14(87):184–186.

Rein, M. (1993). Phenomena of liquid drop impact on solid and liquid surfaces. *Fluid Dynamics Research*, 12(2):61–93.

Rein, M. (1996). The transitional regime between coalescing and splashing drops. *Journal of Fluid Mechanics*, 306:145–165.

Renardy, M. (1989). Mathematical Analysis of Viscoelastic Flows. *Annual Review of Fluid Mechanics*, 21(1):21–34.

Reznik, S. N., Yarin, A. L., Zussman, E., and Bercovici, L. (2006). Evolution of a compound droplet attached to a core-shell nozzle under the action of a strong electric field. *Physics of Fluids*, 18(6):62101.

Reznik, S. N. and Zussman, E. (2010). Capillary-dominated electrified jets of a viscous leaky dielectric liquid. *Physical Review E - Statistical, Nonlinear, and Soft Matter Physics*, 81(2):026313.

Ristenpart, W. D., Bird, J. C., Belmonte, A., Dollar, F., and Stone, H. A. (2009). Non-coalescence of oppositely charged drops. *Nature*, 461(7262):377–380.

Rocco, G., Coppola, G., and de Luca, L. (2010). Simulation of drop impact on a thin liquid film by means of the VOF method. *Aerotecnica Missili and Spazio*, 89(1).

Romanò, F., Muradoglu, M., Fujioka, H., and Grotberg, J. (2021). The effect of viscoelasticity in an airway closure model. *Journal of Fluid Mechanics*, 913:A31.

Romero Herreros, N. (2014). *Experimental study of the influence of an electric field on the shape of a droplet*. PhD thesis, Universitat Politècnica de Catalunya.

Salipante, P. F. and Vlahovska, P. M. (2010). Electrohydrodynamics of drops in strong uniform dc electric fields. *Physics of Fluids*, 22(11):112110.

Saville, D. A. (1997). Electrohydrodynamics: The Taylor-Melcher Leaky Dielectric Model. *Annual Review of Fluid Mechanics*, 29(1):27–64.

Sengupta, R., Walker, L. M., and Khair, A. S. (2017). The role of surface charge convection in the electrohydrodynamics and breakup of prolate drops. *Journal of Fluid Mechanics*, 833:29–53.

Sherwood, J. D. (1988). Breakup of fluid droplets in electric and magnetic fields. *Journal of Fluid Mechanics*, 188:133–146.

Sibillo, V., Simeone, M., and Guido, S. (2004). Break-up of a Newtonian drop in a viscoelastic matrix under simple shear flow. *Rheologica Acta*, 43(5):449–456.

Soni, P., Juvekar, V. A., and Naik, V. M. (2013). Investigation on dynamics of double emulsion droplet in a uniform electric field. *Journal of Electrostatics*, 71(3):471–477.

Sorgentone, C., Kach, J. I., Khair, A. S., Walker, L. M., and Vlahovska, P. M. (2021). Numerical and asymptotic analysis of the three-dimensional electrohydrodynamic interactions of drop pairs. *Journal of Fluid Mechanics*, 914:A24.

Sozou, C. (1975). Electrohydrodynamics of a pair of liquid drops. *Journal of Fluid Mechanics*, 67(2):339–348.

Stone, H. A. (1994). Dynamics of Drop Deformation and Breakup in Viscous Fluids. *Annual Review of Fluid Mechanics*, 26(1):65–102.

Strang, G. (1968). On the Construction and Comparison of Difference Schemes. *SIAM Journal on Numerical Analysis*, 5(3):506–517.

Sunder, S. and Tomar, G. (2013). Numerical simulations of bubble formation from submerged needles under non-uniform direct current electric field. *Physics of Fluids*, 25(10).

Sunder, S. and Tomar, G. (2020). Numerical investigation of a conducting drop's interaction with a conducting liquid pool under an external electric field. *European Journal of Mechanics - B/Fluids*, 81:114–123.

Sussman, M. and Puckett, E. G. (2000). A Coupled Level Set and Volume-of-Fluid Method for Computing 3D and Axisymmetric Incompressible Two-Phase Flows. *Journal of Computational Physics*, 162(2):301–337.

Sussman, M., Smereka, P., and Osher, S. (1994). A Level Set Approach for Computing Solutions to Incompressible Two-Phase Flow. *Journal of Computational Physics*, 114(1):146–159.

Taylor, G. (1964). Disintegration of water drops in an electric field. *Proceedings of the Royal Society of London. Series A. Mathematical and Physical Sciences*, 280(1382):383–397.

Taylor, G. (1966). Studies in electrohydrodynamics. I. The circulation produced in a drop by an electric field. *Proceedings of the Royal Society of London. Series A. Mathematical and Physical Sciences*, 291(1425):159–166.

Taylor, G. I. (1932). The viscosity of a fluid containing small drops of another fluid. *Proceedings of the Royal Society of London. Series A, Containing Papers of a Mathematical and Physical Character*, 138(834):41–48.

Thoraval, M. J., Li, Y., and Thoroddsen, S. T. (2016). Vortex-ring-induced large bubble entrainment during drop impact. *Physical Review E*, 93(3):033128.

Thoroddsen, S. T. and Takehara, K. (2000). The coalescence cascade of a drop. *Physics of Fluids*, 12(6):1265–1267.

Thoroddsen, S. T., Takehara, K., Nguyen, H. D., and Etoh, T. G. (2018). Singular jets during the collapse of drop-impact craters. *Journal of Fluid Mechanics*, 848:R3.

Tomar, G., Gerlach, D., Biswas, G., Alleborn, N., Sharma, A., Durst, F., Welch, S. W., and Delgado, A. (2007). Two-phase electrohydrodynamic simulations using a volume-of-fluid approach. *Journal of Computational Physics*, 227(2):1267–1285.

Toose, E., Geurts, B., and Kuerten, J. (1995). A boundary integral method for two-dimensional (non)-Newtonian drops in slow viscous flow. *Journal of Non-Newtonian Fluid Mechanics*, 60(2-3):129–154.

Torza, S., Cox, R. G., and Mason, S. G. (1971). Electrohydrodynamic deformation and bursts of liquid drops. *Philosophical Transactions of the Royal Society of London. Series A, Mathematical and Physical Sciences*, 269(1198):295–319.

Tretheway, D. C. and Leal, L. G. (2001). Deformation and relaxation of Newtonian drops in planar extensional flows of a Boger fluid. *Journal of Non-Newtonian Fluid Mechanics*, 99(2-3):81–108.

Tsukada, T., Katayama, T., Ito, Y., and Hozawa, M. (1993). Theoretical and Experimental Studies of Circulations Inside and Outside a Deformed Drop under a Uniform Electric Field. *Journal of Chemical Engineering of Japan*, 26(6):698–703.

Tucker, C. L. and Moldenaers, P. (2002). Microstructural Evolution in Polymer Blends. *Annual Review of Fluid Mechanics*, 34(1):177–210.

Varanasi, P. P., Ryan, M. E., and Stroeve, P. (1994). Experimental Study on the Breakup of Model Viscoelastic Drops in Uniform Shear Flow. *Industrial and Engineering Chemistry Research*, 33(7):1858–1866.

Vlahovska, P. M. (2019). Electrohydrodynamics of Drops and Vesicles. *Annual Review of Fluid Mechanics*, 51(1):305–330.

Wagoner, B. W., Vlahovska, P. M., Harris, M. T., and Basaran, O. A. (2020). Electric-field-induced transitions from spherical to discocyte and lens-shaped drops. *Journal of Fluid Mechanics*, 904:R4.

Wang, N., Li, S., Shi, L., Yuan, X., Liu, H., Wang, N., Li, S., Shi, L., Yuan, X., and Liu, H. (2023). Viscoelastic effects on the deformation and breakup of a droplet on a solid wall in Couette flow. *Journal of Fluid Mechanics*, 963:A18.

Wang, Q., Ma, M., and Siegel, M. (2019). Deformation and stability of a viscous electrolyte drop in a uniform electric field. *Physical Review Fluids*, 4(5):053702.

Woodcock, A. H., Kientzler, C. F., Arons, A. B., and Blanchard, D. C. (1953). Giant Condensation Nuclei from Bursting Bubbles. *Nature*, 172(4390):1144–1145.

Worthington, A. M. (1908). *A Study of Splashes*. Outlook Verlag.

Wu, J., Xu, Y., Dabros, T., and Hamza, H. (2003). Effect of Demulsifier Properties on Destabilization of Water-in-Oil Emulsion. *Energy and Fuels*, 17(6):1554–1559.

Xu, X. and Homsy, G. M. (2006). The settling velocity and shape distortion of drops in a uniform electric field. *Journal of Fluid Mechanics*, 564:395–414.

Xu, X., Ouyang, J., Jiang, T., and Li, Q. (2012). Numerical simulation of 3D-unsteady viscoelastic free surface flows by improved smoothed particle hydrodynamics method. *Journal of Non-Newtonian Fluid Mechanics*, 177-178:109–120.

Yarin, A. (2006). Drop impact dynamics: Splashing, Spreading, Receding, Bouncing.... *Annual Review of Fluid Mechanics*, 38(1):159–192.

Youngs, D. L. (1982). *Time-dependent multi-material flow with large fluid distortion*. Academic Press, New York.

Yue, P., Feng, J. J., Liu, C., and Shen, J. (2005). Viscoelastic effects on drop deformation in steady shear. *Journal of Fluid Mechanics*, 540:427–437.

Zabarankin, M. (2020). Small deformation theory for two leaky dielectric drops in a uniform electric field. *Proceedings of the Royal Society A: Mathematical, Physical and Engineering Sciences*, 476(2233):20190517.

Zainali, A., Tofighi, N., Shadloo, M., and Yildiz, M. (2013). Numerical investigation of Newtonian and non-Newtonian multiphase flows using ISPH method. *Computer Methods in Applied Mechanics and Engineering*, 254:99–113.

Zhang, X., Basaran, O. A., and Wham, R. M. (1995). Theoretical prediction of electric field-enhanced coalescence of spherical drops. *AIChE Journal*, 41(7):1629–1639.

Zimmermann, U. and Vienken, J. (1982). Electric field-induced cell-to-cell fusion. *The Journal of Membrane Biology*, 67(1):165–182.

Appendix A

Log conformation representation

The numerical solution of viscoelastic problems fails when the value of the relaxation parameter is large. This is known as the High Wissenberg number problem. Fattal and Kupferman (2004) identified that the numerical instability was caused due to the exponential growth of the stresses. The remedy suggested by them was to use a kernel transformation. In this method, instead of advancing the conformation tensor, they proposed to advance its logarithm in time.

$$\boldsymbol{\Psi} = \log \mathbf{A} \tag{A.1}$$

Since $\mathbf{A}$ is symmetric and positive-definite, it is always diagonalizable as

$$\mathbf{A} = \mathbf{R}\ \Lambda\ \mathbf{R}^T \quad \text{and} \quad \boldsymbol{\Psi} = \log \mathbf{A} = \mathbf{R}\ \log \Lambda\ \mathbf{R}^T\ , \tag{A.2}$$

where Λ is the diagonal matrix formed with the eigenvalues and $\mathbf{R}$ is the tensor formed by arranging the eigenvectors. The diagonalization is also used to decompose the velocity gradient as

$$\boldsymbol{\nabla u} = \boldsymbol{\Omega} + \mathbf{B} + \mathbf{N}\mathbf{A}^{-1}\ , \tag{A.3}$$

where $\boldsymbol{\Omega}$ and $\mathbf{N}$ are antisymmetric and $\mathbf{B}$ is symmetric, traceless and commutes with $\mathbf{A}$. The equation for $\boldsymbol{\Psi}$ becomes

$$\frac{\partial \boldsymbol{\Psi}}{\partial t} + \boldsymbol{u} \cdot \boldsymbol{\nabla \Psi} - 2\mathbf{B} - (\boldsymbol{\Omega\Psi} - \boldsymbol{\Psi\Omega}) = -\frac{e^{-\boldsymbol{\Psi}}}{\lambda}\mathbf{f_R}(e^{\boldsymbol{\Psi}}) \tag{A.4}$$

For a 2D study, the velocity gradient can be written as

$$\begin{pmatrix} m_{11} & m_{12} \\ m_{21} & m_{22} \end{pmatrix} = \mathbf{R}^T(\boldsymbol{\nabla u})\mathbf{R} \tag{A.5}$$

and the elements of the decomposition are

$$\mathbf{B} = \mathbf{R}\begin{pmatrix} m_{11} & 0 \\ 0 & m_{22} \end{pmatrix}\mathbf{R}^T\,, \quad \boldsymbol{\Omega} = \mathbf{R}\begin{pmatrix} 0 & \omega \\ -\omega & 0 \end{pmatrix}\mathbf{R}^T\,, \quad \mathbf{N} = \mathbf{R}\begin{pmatrix} 0 & n \\ -n & 0 \end{pmatrix}\mathbf{R}^T \tag{A.6}$$

with $\omega = \frac{\Lambda_2 m_{12} + \Lambda_1 m_{21}}{\Lambda_2 - \Lambda_1}$ and $n = \frac{m_{12}+m_{21}}{\Lambda_2^{-1} - \Lambda_1^{-1}}$.

Appendix B

Dimensionless equations

The Navier–Stokes equations for the incompressible fluid motion are

$$\boldsymbol{\nabla} \cdot \mathbf{u} = 0 \,, \tag{B.1}$$

$$\rho \left[\frac{\partial \mathbf{u}}{\partial t} + \mathbf{u} \cdot \boldsymbol{\nabla} \mathbf{u} \right] = -\boldsymbol{\nabla} p + \boldsymbol{\nabla} \cdot \mathbb{T} + \mathbf{F}_s + \mathbf{F}_e \,, \tag{B.2}$$

The surface tension force is given as

$$\mathbf{F}_s = \gamma \kappa \delta_s \hat{\mathbf{n}} \,, \tag{B.3}$$

The stress tensor ($\mathbb{T}$) in the momentum equation is given as

$$\boldsymbol{\nabla} \cdot \mathbb{T} = \boldsymbol{\nabla} \cdot \mathbb{T}_s + \boldsymbol{\nabla} \cdot \mathbb{T}_p \tag{B.4}$$

The viscous stress tensor is expressed as

$$\mathbb{T}_s = 2\mu_s \mathbb{D} = \mu_s \left(\boldsymbol{\nabla} \mathbf{u} + \boldsymbol{\nabla} \mathbf{u}^T \right) \tag{B.5}$$

The polymeric stress tensor is expressed using the constitutive equation of Oldroyd-B model as

$$\lambda \left[\frac{\partial \mathbb{T}_p}{\partial t} + \mathbf{u} \cdot \boldsymbol{\nabla} \mathbb{T}_p - (\boldsymbol{\nabla} \mathbf{u}) \cdot \mathbb{T}_p - \mathbb{T}_p \cdot (\boldsymbol{\nabla} \mathbf{u})^T \right] + \mathbb{T}_p = \mu_p \left(\boldsymbol{\nabla} \mathbf{u} + \boldsymbol{\nabla} \mathbf{u}^T \right) \tag{B.6}$$

The electric force is written as the divergence of the Maxwell stress tensor ($\mathbb{T}_e$) as

$$\mathbf{F}_e = \boldsymbol{\nabla} \cdot \mathbb{T}_e = \varepsilon \left(\mathbf{E}\mathbf{E} - \frac{E^2}{2}\mathbf{I} \right) \tag{B.7}$$

The Poisson equation is given as

$$\boldsymbol{\nabla} \cdot (\varepsilon \mathbf{E}) = \boldsymbol{\nabla} \cdot (\varepsilon \boldsymbol{\nabla} \varphi) = -q_v \tag{B.8}$$

The charge conservation equation is given as

$$\frac{\partial q_v}{\partial t} + \boldsymbol{\nabla} \cdot (q_v \mathbf{u}) = \boldsymbol{\nabla} \cdot (\sigma \boldsymbol{\nabla} \varphi) \tag{B.9}$$

The fluid and electrical properties in the one fluid formulation are interpolated as

$$\begin{aligned} \rho &= C\rho_1 + (1-C)\rho_2 \,, \qquad \mu = C\mu_1 + (1-C)\mu_2 \,, \\ \varepsilon &= C\varepsilon_1 + (1-C)\varepsilon_2 \,, \qquad \sigma = C\sigma_1 + (1-C)\sigma_2 \,. \end{aligned} \tag{B.10}$$

These properties are made dimensionless using the properties of the ambient fluid (2) as

$$\begin{aligned} \frac{\rho}{\rho_2} &= C\frac{\rho_1}{\rho_2} + (1-C) \,, \qquad \frac{\mu}{\mu_2} = C\frac{\mu_1}{\mu_2} + (1-C) \,, \\ \frac{\varepsilon}{\varepsilon_2} &= C\frac{\varepsilon_1}{\varepsilon_2} + (1-C) \,, \qquad \frac{\sigma}{\sigma_2} = C\frac{\sigma_1}{\sigma_2} + (1-C) \,. \end{aligned}$$

which reduces to

$$\begin{aligned} \rho^* &= C\rho_r + (1-C) \,, \qquad \mu^* = C\mu_r + (1-C) \,, \\ \varepsilon^* &= CQ + (1-C) \,, \qquad \sigma^* = CR + (1-C) \,. \end{aligned} \tag{B.11}$$

Here, the * quantities are the dimensionless terms. The governing equations are made dimensionless, we use the following scales

$$\text{length scale} \sim a \,, \qquad \text{velocity scale} \sim U_e$$

$$\text{pressure scale} \sim \rho_2 U_e^2 \,, \qquad \text{polymeric stress scale} \sim \rho_2 U_e^2$$

$$\text{electric field scale} \sim E_\infty \,, \qquad \text{volumetric charge scale} \sim \frac{\varepsilon_2 E_\infty}{a}$$

The electrohydrodynamic velocity scale (U_e) is derived by balancing the viscous and electric forces as

$$\text{viscous force} \sim \text{electric force}$$
$$\Rightarrow \frac{\mu_2 u}{a^2} \sim \frac{E_\infty^2 \varepsilon_2}{a}$$
$$\Rightarrow u \sim \frac{\varepsilon_2 E_\infty^2 a}{\mu_2}$$

Next we describe the dimensionless governing equations.

$$\boldsymbol{\nabla}^* \cdot \mathbf{u}^* = 0 \tag{B.12}$$

$$\rho\left[\frac{\partial \mathbf{u}}{\partial t} + \mathbf{u}\cdot\boldsymbol{\nabla}\mathbf{u}\right] = -\boldsymbol{\nabla}p + \boldsymbol{\nabla}\cdot\mathbb{T}_p + \boldsymbol{\nabla}\cdot\left[\mu_s\left(\boldsymbol{\nabla}\mathbf{u} + \boldsymbol{\nabla}\mathbf{u}^T\right)\right] + \gamma\kappa\delta_s\hat{\mathbf{n}} + \boldsymbol{\nabla}\cdot\left[\varepsilon\left(\mathbf{E}\mathbf{E} - \frac{E^2}{2}\mathbf{I}\right)\right]$$

$$\Rightarrow \rho\left[\frac{\partial \mathbf{u}}{\partial t} + \mathbf{u}\cdot\boldsymbol{\nabla}\mathbf{u}\right] = -\boldsymbol{\nabla}p + \boldsymbol{\nabla}\cdot\mathbb{T}_p + \left(\frac{\mu_s}{\mu}\right)\boldsymbol{\nabla}\cdot\left[\mu\left(\boldsymbol{\nabla}\mathbf{u} + \boldsymbol{\nabla}\mathbf{u}^T\right)\right] + \gamma\kappa\delta_s\hat{\mathbf{n}} + \boldsymbol{\nabla}\cdot\left[\varepsilon\left(\mathbf{E}\mathbf{E} - \frac{E^2}{2}\mathbf{I}\right)\right]$$

$$\Rightarrow \rho\left[\frac{\partial \mathbf{u}}{\partial t} + \mathbf{u}\cdot\boldsymbol{\nabla}\mathbf{u}\right] = -\boldsymbol{\nabla}p + \boldsymbol{\nabla}\cdot\mathbb{T}_p + \beta\boldsymbol{\nabla}\cdot\left[\mu\left(\boldsymbol{\nabla}\mathbf{u} + \boldsymbol{\nabla}\mathbf{u}^T\right)\right] + \gamma\kappa\delta_s\hat{\mathbf{n}} + \boldsymbol{\nabla}\cdot\left[\varepsilon\left(\mathbf{E}\mathbf{E} - \frac{E^2}{2}\mathbf{I}\right)\right]$$

$$\begin{aligned}\Rightarrow \left(\frac{\rho_2 U_e^2}{a}\right)\rho^*\left[\frac{\partial \mathbf{u}^*}{\partial t^*} + \mathbf{u}^*\cdot\boldsymbol{\nabla}^*\mathbf{u}^*\right] = &-\left(\frac{\rho_2 U_e^2}{a}\right)\boldsymbol{\nabla}^* p^* + \left(\frac{\rho_2 U_e^2}{a}\right)\boldsymbol{\nabla}^*\cdot\mathbb{T}_p^* \\ &+ \left(\frac{\gamma}{a^2}\right)\kappa^*\delta_s^*\hat{\mathbf{n}} \\ &+ \beta\left(\frac{\mu_2 U_e}{a^2}\right)\boldsymbol{\nabla}^*\cdot\left[\mu^*\left(\boldsymbol{\nabla}^*\mathbf{u}^* + \boldsymbol{\nabla}^*\mathbf{u}^{*T}\right)\right] \\ &+ \left(\frac{\varepsilon_2 E_\infty^2}{a}\right)\boldsymbol{\nabla}^*\cdot\left[\varepsilon^*\left(\mathbf{E}^*\mathbf{E}^* - \frac{E^{*2}}{2}\mathbf{I}\right)\right]\end{aligned}$$

$$\Rightarrow \rho^* \left[\frac{\partial \mathbf{u}^*}{\partial t^*} + \mathbf{u}^* \cdot \boldsymbol{\nabla}^* \mathbf{u}^*\right] = -\boldsymbol{\nabla}^* p^* + \boldsymbol{\nabla}^* \cdot \mathbb{T}_p^* + \left(\frac{\gamma}{a\rho_2 U_e^2}\right) \kappa^* \delta_s^* \hat{\mathbf{n}} + \beta \left(\frac{\mu_2}{\rho_2 U_e a}\right) \boldsymbol{\nabla}^* \cdot \left[\mu^* \left(\boldsymbol{\nabla}^* \mathbf{u}^* + \boldsymbol{\nabla}^* \mathbf{u}^{*T}\right)\right] + \left(\frac{\varepsilon_2 E_\infty^2}{\rho_2 U_e^2}\right) \boldsymbol{\nabla}^* \cdot \left[\varepsilon^* \left(\mathbf{E}^* \mathbf{E}^* - \frac{E^{*2}}{2} \mathbf{I}\right)\right]$$

$$\Rightarrow \rho^* \left[\frac{\partial \mathbf{u}^*}{\partial t^*} + \mathbf{u}^* \cdot \boldsymbol{\nabla}^* \mathbf{u}^*\right] = -\boldsymbol{\nabla}^* p^* + \boldsymbol{\nabla}^* \cdot \mathbb{T}_p^* + \left(\frac{1}{Re} \; \frac{1}{Ca_E}\right) \kappa^* \delta_s^* \hat{\mathbf{n}} + \left(\frac{\beta}{Re}\right) \boldsymbol{\nabla}^* \cdot \left[\mu^* \left(\boldsymbol{\nabla}^* \mathbf{u}^* + \boldsymbol{\nabla}^* \mathbf{u}^{*T}\right)\right] + \left(\frac{1}{Re}\right) \boldsymbol{\nabla}^* \cdot \left[\varepsilon^* \left(\mathbf{E}^* \mathbf{E}^* - \frac{E^{*2}}{2} \mathbf{I}\right)\right] \tag{B.13}$$

For Newtonian studies, polymer stress tensor is absent. For viscoelastic studies we consider the Oldroyd-B model.

$$\lambda \left[\frac{\partial \mathbb{T}_p}{\partial t} + \mathbf{u} \cdot \boldsymbol{\nabla} \mathbb{T}_p - (\boldsymbol{\nabla} \mathbf{u}) \cdot \mathbb{T}_p - \mathbb{T}_p \cdot (\boldsymbol{\nabla} \mathbf{u})^T\right] + \mathbb{T}_p = \mu_p \left(\boldsymbol{\nabla} \mathbf{u} + \boldsymbol{\nabla} \mathbf{u}^T\right)$$

$$\Rightarrow \lambda \left[\frac{\partial \mathbb{T}_p}{\partial t} + \mathbf{u} \cdot \boldsymbol{\nabla} \mathbb{T}_p - (\boldsymbol{\nabla} \mathbf{u}) \cdot \mathbb{T}_p - \mathbb{T}_p \cdot (\boldsymbol{\nabla} \mathbf{u})^T\right] + \mathbb{T}_p = \left(\frac{\mu_p}{\mu}\right) \mu \left(\boldsymbol{\nabla} \mathbf{u} + \boldsymbol{\nabla} \mathbf{u}^T\right)$$

$$\Rightarrow \lambda \left(\frac{\rho_2 U_e^3}{a}\right) \left[\frac{\partial \mathbb{T}_p^*}{\partial t^*} + \mathbf{u}^* \cdot \boldsymbol{\nabla}^* \mathbb{T}_p^* - (\boldsymbol{\nabla}^* \mathbf{u}^*) \cdot \mathbb{T}_p^* - \mathbb{T}_p^* \cdot (\boldsymbol{\nabla}^* \mathbf{u}^*)^T\right] + \left(\rho_2 U_e^2\right) \mathbb{T}_p^* = (1-\beta) \left(\frac{\mu_2 U_e}{a}\right) \mu^* \left(\boldsymbol{\nabla}^* \mathbf{u}^* + \boldsymbol{\nabla}^* \mathbf{u}^{*T}\right)$$

$$\Rightarrow \lambda \left(\frac{U_e}{a}\right) \left[\frac{\partial \mathbb{T}_p^*}{\partial t^*} + \mathbf{u}^* \cdot \boldsymbol{\nabla}^* \mathbb{T}_p^* - (\boldsymbol{\nabla}^* \mathbf{u}^*) \cdot \mathbb{T}_p^* - \mathbb{T}_p^* \cdot (\boldsymbol{\nabla}^* \mathbf{u}^*)^T\right] + \mathbb{T}_p^* = (1-\beta) \left(\frac{\mu_2}{\rho_2 U_e a}\right) \left(\boldsymbol{\nabla}^* \mathbf{u}^* + \boldsymbol{\nabla}^* \mathbf{u}^{*T}\right)$$

$$\Rightarrow (De)\left[\frac{\partial \mathbb{T}_p^*}{\partial t^*} + \mathbf{u}^* \cdot \boldsymbol{\nabla}^* \mathbb{T}_p^* \quad -(\boldsymbol{\nabla}^* \mathbf{u}^*) \cdot \mathbb{T}_p^* - \mathbb{T}_p^* \cdot (\boldsymbol{\nabla}^* \mathbf{u}^*)^T\right] + \mathbb{T}_p^*$$
$$= \left(\frac{1-\beta}{Re}\right)\left(\boldsymbol{\nabla}^* \mathbf{u}^* + \boldsymbol{\nabla}^* \mathbf{u}^{*T}\right) \tag{B.14}$$

Now, the electrostatic equations are made dimensionless.

$$\begin{aligned}
\boldsymbol{\nabla} \cdot (\varepsilon \mathbf{E}) &= -q_v \\
\Rightarrow \left(\frac{\varepsilon_2 E_\infty}{a}\right) \boldsymbol{\nabla}^* \cdot (\varepsilon^* \mathbf{E}^*) &= -\left(\frac{\varepsilon_2 E_\infty}{a}\right) q_v^* \\
\Rightarrow \boldsymbol{\nabla}^* \cdot (\varepsilon^* \mathbf{E}^*) &= -q_v^* \qquad \text{(B.15)} \\
\frac{\partial q_v}{\partial t} + \boldsymbol{\nabla} \cdot (q_v \mathbf{u}) &= -\boldsymbol{\nabla} \cdot (\sigma \mathbf{E}) \\
\Rightarrow \left(\frac{\varepsilon_2 E_\infty U_e}{a^2}\right)\left[\frac{\partial q_v^*}{\partial t^*} + \boldsymbol{\nabla}^* \cdot (q_v^* \mathbf{u}^*)\right] &= -\left(\frac{\sigma_2 E_\infty}{a}\right) \boldsymbol{\nabla}^* \cdot (\sigma^* \mathbf{E}^*) \\
\Rightarrow \frac{\partial q_v^*}{\partial t^*} + \boldsymbol{\nabla}^* \cdot (q_v^* \mathbf{u}^*) &= -\left(\frac{a/U_e}{\varepsilon_2/\sigma_2}\right) \boldsymbol{\nabla}^* \cdot (\sigma^* \mathbf{E}^*) \\
\Rightarrow \frac{\partial q_v^*}{\partial t^*} + \boldsymbol{\nabla}^* \cdot (q_v^* \mathbf{u}^*) &= -\left(\frac{1}{Re_E}\right) \boldsymbol{\nabla}^* \cdot (\sigma^* \mathbf{E}^*) \qquad \text{(B.16)}
\end{aligned}$$

Finally, we have the following dimensionless parameters

$$\begin{aligned}
&\text{Reynolds number } Re = \frac{\rho_2 U_e a}{\mu_2} = \frac{\rho_2 \varepsilon_2 E_\infty^2 a^2}{\mu_2^2}, \\
&\text{Electric Capillary number } Ca_E = \frac{\mu_2 U_e}{\gamma} = \frac{\varepsilon_2 E_\infty^2 a}{\gamma}, \\
&\text{Electric Reynolds number } Re_E = \frac{\varepsilon_2/\sigma_2}{a/U_e}, \\
&\text{Deborah number } De = \frac{\lambda U_e}{a} = \frac{\lambda}{a/U_e}.
\end{aligned} \tag{B.17}$$

Appendix C

Grid representation

The in-house solver based on the CLSVOF method is used to study the dynamics of a drop impacting a liquid pool. A uniform grid arrangement is used where the grid size in both directions is considered the same, i.e., $\Delta x = \Delta y$. A representation of the grid is shown below in Figure C.1.

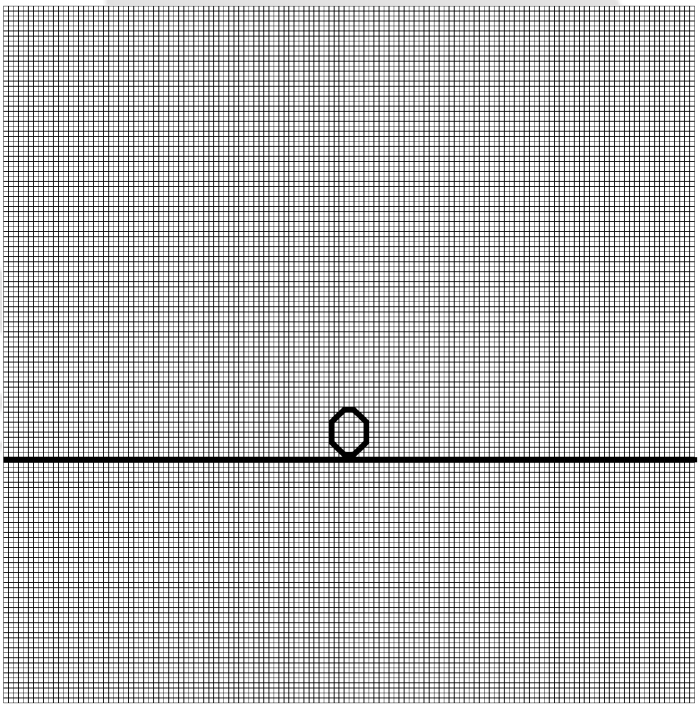

Fig. C.1 A representation of the grid used to study drop impact dynamics. An axisymmetric system is used for the study. The grid has been mirrored for better visualization. We also show the initial configuration of the system.

The open-source solver Basilisk uses a quadtree grid structure. The Adaptive Mesh Refinement (AMR) capability of the solver allows it to refine and coarsen the mesh dynamically. We show the adaptive grid arrangement for single drop (Figure C.2) and compound drop (Figure C.3). The mesh is refined based on the volume fraction gradient. Accordingly, we find a very fine mesh near the interface while a relatively coarser mesh elsewhere.

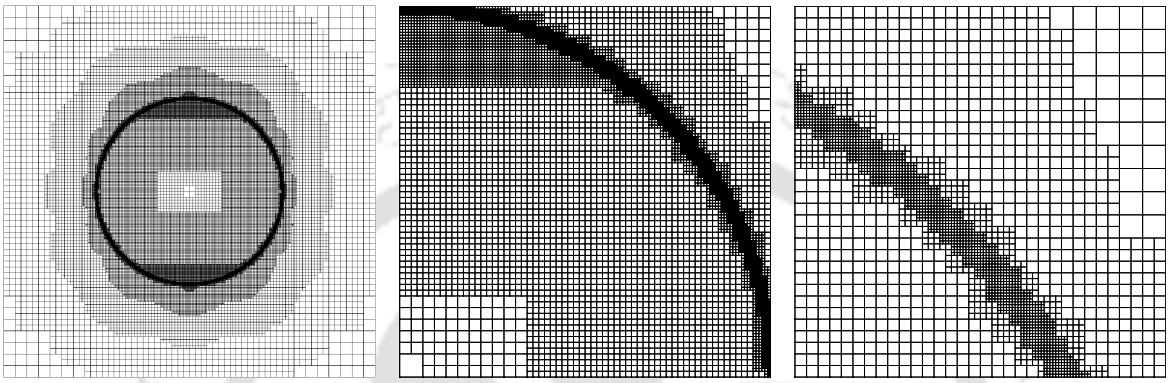

(a) (b) (c)

Fig. C.2 Different zoom levels showing grid refinement for a single emulsion drop. The minimum grid level is $l = 6$ while the maximum grid level is $l = 12$.

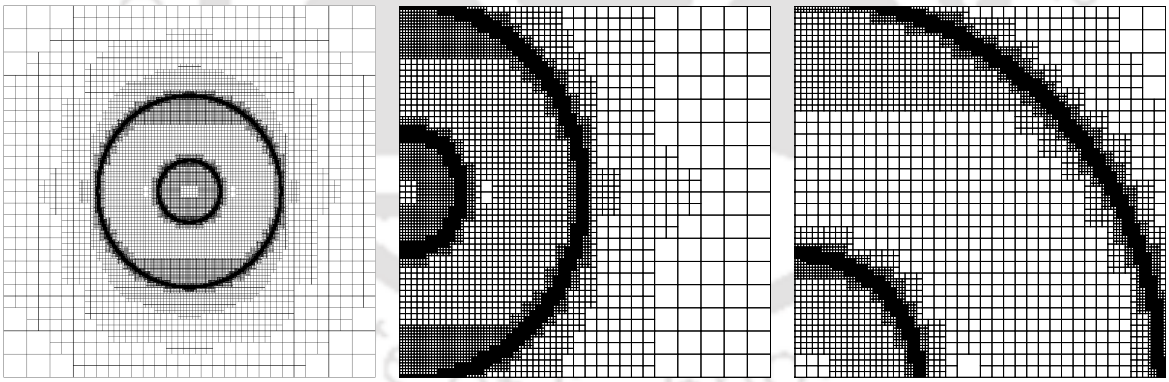

(a) (b) (c)

Fig. C.3 Different zoom levels showing grid refinement for a double emulsion drop. The minimum grid level is $l = 6$ while the maximum grid level is $l = 12$.

List of publications

Journals

1. **Santanu Kumar Das**, Amaresh Dalal, Gaurav Tomar, Electrohydrodynamic Induced Interactions between Droplets, *Journal of Fluid Mechanics*, vol. 915, A88, 2021.

2. **Santanu Kumar Das**, Amaresh Dalal, Michael Breuer and Gautam Biswas, Evolution of Jets During Drop Impact on a Deep Liquid Pool, *Physics of Fluids*, vol. 34, no. 2, p. 022110, 2022.

3. **Santanu Kumar Das**, Amaresh Dalal, Gaurav Tomar, Numerical Study on Electrocoalescence Criterion for Leaky-dielectric Drops, *Submitted*.

4. **Santanu Kumar Das**, Amaresh Dalal, Gaurav Tomar, Deformation and stability of viscoelastic drops in a steady electric field, *Under preparation*.

Conferences

1. **Santanu Kumar Das**, Amaresh Dalal, Three Dimensional Simulation of Droplet Impact on Liquid Pool, *International Heat and Mass Transfer Conference* (IHMTC), IIT Madras, 17th - 20th December, 2021.

2. **Santanu Kumar Das**, Sarika S. Bangar, Amaresh Dalal, Gaurav Tomar, Effect of viscoelasticity on drop deformation in a uniform electric field, *Annual Meeting of the Division of Fluid Dynamics* (APS-DFD), Indianapolis, Indiana, 20th - 22nd November, 2022.